

Hazy
a brief introduction to CLOUDY C17
3. Physics

Cloudy & Associates

www.nublado.org

April 17, 2019

Software: Copyright © 1978-2019 Gary J. Ferland and others. All rights reserved.

The software described in this documentation (CLOUDY) is subject to a FreeBSD-style software license contained in the file `license.txt` in the root directory of the distributed files. The list of co-authors is given in the file `others.txt` in the same directory. Use of this program is not restricted provided each use is acknowledged upon publication. The bibliographic reference to this version of CLOUDY is “version xx.xx of the code last described [Ferland et al. \(2017\)](#).” The version number, shown here as “xx.xx”, should be given. This version number, along with a complete citation, can be found by executing the code with the **print citation** command included in the input script.

CLOUDY is an evolving code. You should confirm that you have the most recent version of the code by checking the web site www.nublado.org. The code has a [discussion board](#) with emailing list. This will have announcements of any updates to the code.

Portions of the documentation have been published, and are copyrighted by, the American Astronomical Society, the Astronomical Society of the Pacific, and the Royal Astronomical Society. The remainder of the documentation is subject to the following FreeBSD format documentation license:

Documentation: Copyright © 1978–2019 Gary J. Ferland and others. All rights reserved.

Redistribution and use of the documentation (all parts of HAZY and the Quick Start Guide) in source (L^AT_EX) and ‘compiled’ forms (PDF, PostScript, HTML and so forth) with or without modification, are permitted provided that the following conditions are met:

1. Redistributions of source code (L^AT_EX) must retain the above copyright notice, this list of conditions and the following disclaimer as the first lines of the file `license.doc.txt` in the root directory unmodified.
2. Redistributions in compiled form (converted to PDF, PostScript, XML, HTML and other formats) must reproduce the above copyright notice, this list of conditions and the following disclaimer in the documentation and/or other materials provided with the distribution.

This documentation is provided by the CLOUDY project “as is” and any express or implied warranties, including, but not limited to, the implied warranties of merchantability and fitness for a particular purpose are disclaimed. In no event shall the CLOUDY project be liable for any direct, indirect, incidental, special, exemplary, or consequential damages (including, but not limited to, procurement of substitute goods or services; loss of use, data, or profits; or business interruption) however caused and on any theory of liability, whether in contract, strict liability, or tort (including negligence or otherwise) arising in any way out of the use of this documentation, even if advised of the possibility of such damage.

Cover image: The predicted X-ray spectrum of a warm absorber in an Active Galactic Nucleus. Prominent emission and absorption lines are present along with broad UTA absorption features. The parameters are from [Reynolds and Fabian \(1995\)](#).

CONTENTS

LIST OF FIGURES	vii
LIST OF TABLES	ix
1 THE MODEL ATOM FOR ISO-SEQUENCES	1
1.1 Overview	1
1.2 Departure coefficients	1
1.3 Pressure lowering of the ionization potential	2
1.4 Recombination rates and cooling	2
1.4.1 Formalism	2
1.4.2 Results	3
1.5 The collisional rate equations	5
1.6 The radiative rate equations	7
1.6.1 Photoionization—recombination	7
1.6.2 Derivation of radiative balance equations	7
1.6.3 Final radiative equations	8
2 THE HYDROGENIC ISO-SEQUENCE	11
2.1 Recombination rates and cooling	11
2.1.1 Rational approximations	11
2.2 Effective transition probabilities	11
2.2.1 Einstein A_s	11
2.3 Collisional contributions to hydrogen lines	12
2.4 Continuous thermal emission	12
3 HELIUM ISO-SEQUENCE	17
3.1 Overview	17
3.2 Energy levels	17
3.3 The He I triplets	17
3.4 Collapsed versus resolved levels	20
3.5 Emission from a pure helium gas	20
4 H^- AND MOLECULES	23
4.1 Overview	23
4.2 The Saha equation for arbitrary systems	23

4.3	LTE Populations of hydrogen molecules	25
4.4	The H^- balance; radiative processes	25
4.4.1	Radiative attachment	26
4.4.2	Photodetachment	27
4.4.3	Photodetachment by hard photons	27
4.4.4	The approach to LTE; high radiation densities	27
4.5	The H^- balance; collisional processes	29
4.5.1	Associative detachment	29
4.5.2	Electron collisional detachment	29
4.5.3	Collisional ionization by suprathermal electrons	30
4.5.4	Mutual neutralization	30
4.5.5	Charge neutralization with heavy elements	30
4.5.6	Neglected processes	30
4.5.7	The approach to LTE; high hydrogen densities	31
4.6	The HeH^+ molecular ion	31
4.7	Linearization of the balance equations	32
4.8	The H_2 molecule	32
4.8.1	Stoichiometry	32
4.8.2	Associative detachment of H^-	32
4.8.3	Catalysis on grain surfaces	33
4.8.4	Excited atom radiative association	33
4.8.5	Excited molecular dissociation	33
4.8.6	Collisional dissociation by H^0 , He^0 , and e^-	34
4.9	Heavy element molecules	34
4.9.1	Cooling	34
5	THE HEAVY ELEMENTS	35
5.1	Overview	35
5.2	Solar system abundances	36
5.3	Periodic table	36
5.4	Ionization balance	37
5.4.1	Photoionization cross sections	37
5.4.2	Auger multi-electron ejection	37
5.4.3	Compton scattering ionization of bound electrons	37
5.4.4	Collisional ionization rate coefficients	38
5.4.5	Charge transfer	38
5.5	Ionization potentials	38
5.6	Isoelectronic sequences	38
5.7	Be-sequence	42
5.8	Carbon	42
5.9	Nitrogen	42
5.10	Oxygen	45
5.10.1	The O I model atom	45
5.11	Neon	46
5.12	Magnesium	46

5.13	Aluminum	46
5.14	Calcium	46
5.15	Iron	46
5.15.1	Fe $K\alpha$ emission	48
5.16	Heavy element opacities	48
5.17	Overall reliability	48
5.18	Solving the ionization ladder	53
5.19	Ionization potentials of subshells	56
6	THERMAL EQUILIBRIUM	67
6.1	Overview	67
6.2	Thermal stability	67
6.3	Compton energy exchange	68
6.4	Bound Compton ionization, heating	71
6.5	Expansion cooling	71
6.6	Free-free heating-cooling	71
6.7	Photoelectric heating, recombination cooling	72
6.8	Collisional ionization—three-body recombination	72
6.9	H ⁻ heating and cooling	73
	H ⁻ bound-free	73
6.9.1	H ⁻ free-free	73
6.10	Line heating and cooling	73
6.10.1	Overview	73
6.10.2	Two level atoms	74
6.10.3	Three level atoms	74
6.10.4	Li Sequence	75
6.10.5	Boron Sequence	75
6.10.6	Beryllium sequence atoms	77
6.11	Evaluation of the cooling function	78
6.11.1	Total cooling	78
6.11.2	The cooling derivative	78
6.12	Evaluation of the heating function	78
6.13	Equilibrium calculations	78
6.13.1	Hydrogen only	78
6.13.2	Helium-only gas	80
6.13.3	Metal rich gas	80
7	GRAIN PHYSICS	83
7.1	Overview	83
7.2	Grain opacity	83
7.2.1	ISM grains	83
7.2.2	Orion grains	84
7.2.3	PN grains	84
7.2.4	Extinction	84
7.3	Photoelectric emission	84

7.4	Collisional charging of a grain	86
7.5	Grain potential	87
7.6	Grain drift velocity	87
7.7	Radiative heating and cooling of a grain	87
7.8	Collisional heating of a grain	88
7.9	Grain temperature	88
7.10	Photoelectric heating of the gas	89
7.11	Collisional cooling of the gas	89
7.12	Grain sublimation	89
7.13	Ionic recombination on grain surfaces	89
8	OTHER PHYSICAL PROCESSES	91
8.1	Overview	91
8.2	Magnetic fields	91
8.3	Cosmic ray interactions	92
8.4	Secondary ionization	94
8.4.1	Ionization, heating, and cooling	94
8.4.2	Secondary rates per atom	94
8.4.3	Total interaction rates	95
8.4.4	Rates during the hydrogen balance solution	95
8.4.5	Molecules and Suprathermal Electrons	95
8.5	Pressure laws	96
8.5.1	Units	96
8.5.2	Ideal gas laws	96
8.5.3	Equation of state	96
8.5.4	Turbulent pressure	97
8.5.5	Ram or dynamic pressure	97
8.6	Line radiation pressure	97
8.6.1	Formalism	97
8.6.2	Line width	99
8.6.3	Background opacity and thermalization	99
8.7	Radiative acceleration	100
8.8	Wind geometry	100
8.9	Eddington limit	101
8.10	Jeans length and mass	101
8.11	Luminosity Distance	103
	REFERENCES	105

LIST OF FIGURES

1.1	H recombination cooling	5
1.2	H populations vs density	6
1.3	H populations vs radiation field	8
2.1	Hydrogen line ratios	12
2.2	H emission comparision	14
2.3	H emission in black body limit	15
3.1	He iso sequence energy levels	18
3.2	Energies within high-n levels of He	20
3.3	l-mixed principle quantum number vs density	21
3.4	He I emission	22
4.1	H ⁻ departure coefficients vs radiation energy density	28
4.2	Rate coefficient for H ⁻ → H ₂ . The rates are taken from Launay et al. (1991)	29
4.3	H ⁻ departure coefficients vs density	31
5.1	Solar system abundances	36
5.2	Photoionization cross sections and yields for Fe ⁺	37
5.3	Ionization potentials of the elements	40
5.4	Energy level diagrams for second-row elements	41
5.5	Be-sequence model atom	42
5.6	O I energy levels	45
5.7	CaII model atom	47
5.8	Fe II model of low-lying levels	48
5.9	Fe IV model atom	49
5.10	Fe VII model atom	50
5.11	Fe Kα yield and energy	51
5.12	Atomic gas opacity	52
6.1	Compton Equilibrium Error	69
6.2	Compton equilibrium in the STE limit	70
6.3	Energy Level Diagram for Boron Sequence.	76
6.4	Energy Level Diagram for Beryllium Sequence.	77
6.5	Pure hydrogen approach to STE	79
6.6	High metallicity gas approach to LTE	81

7.1	Grain opacities	85
8.1	Wind velocity vs depth	102

LIST OF TABLES

1.1	State Specific and Case B Recombination Coefficients	3
1.2	State Specific and Case B Recombination Cooling Coefficients	4
3.1	Wavelengths of transitions of the He-like sequence	19
5.1	Ionization Potentials of the Elements (Rydbergs)	38
5.1	Ionization Potentials of the Elements (Rydbergs) – Continued	39
5.1	Ionization Potentials of the Elements (Rydbergs) – Continued	39
5.2	Isoelectronic Sequences	43
5.2	Isoelectronic Sequences – Continued	44
5.2	Isoelectronic Sequences – Continued	44
5.3	Ionization Balance Reliability	53
5.3	Ionization Balance Reliability – Continued	54
5.3	Ionization Balance Reliability – Continued	55
5.4	Ionization Potentials of Subshells (eV)	57
5.4	Ionization Potentials of Subshells (eV) – Continued	58
5.4	Ionization Potentials of Subshells (eV) – Continued	59
5.4	Ionization Potentials of Subshells (eV) – Continued	60
5.4	Ionization Potentials of Subshells (eV) – Continued	61
5.4	Ionization Potentials of Subshells (eV) – Continued	62
5.4	Ionization Potentials of Subshells (eV) – Continued	63
5.4	Ionization Potentials of Subshells (eV) – Continued	64
5.4	Ionization Potentials of Subshells (eV) – Continued	65
6.1	Lithium Sequence Lines	76
8.1	Secondary Ionization Efficiencies	95

Chapter 1

THE MODEL ATOM FOR ISO-SEQUENCES

1.1 Overview

CLOUDY is designed to model environments that range from the low-density limit to strict thermodynamic equilibrium. Eventually all isoelectronic series will be treated as a multi-level atom plus continuum. The following chapters go over the H-like and He-like sequences. This chapter provides an overview.

Following sections are adapted from [Ferland and Rees \(1988\)](#), [Ferland and Persson \(1989\)](#), and [Ferland et al. \(1992\)](#).

1.2 Departure coefficients

Departure coefficient is the ratio of the actual population of a state to its population in thermodynamic equilibrium. They are useful since they allow direct comparison of a population to its asymptotic equilibrium limit.

The LTE relative population density for level n is given by

$$\begin{aligned} P_n^* &= \frac{n_n^*}{n_e n_{ion}} = \frac{g_n}{g_e g_{ion}} \left(\frac{m_n^*}{m_e m_{ion}} \frac{h^2}{2\pi kT} \right)^{3/2} \exp(+\chi_n) \\ &\approx \frac{g_n}{g_e g_{ion}} \left(\frac{h^2}{2\pi m_e kT} \right)^{3/2} \exp(+\chi_n) \quad [\text{cm}^3] \\ &= \frac{g_n}{g_e g_{ion}} 4.1412957 \times 10^{-16} T^{-3/2} \exp(+\chi_n) \end{aligned} \quad (1.1)$$

where the electron statistical weight is $g_e = 2$, the ion statistical weights are 1 and 2 for H-like and He-like species, all nuclear statistical weights are ignored, and $g_n = 2n^2$ is the statistical weight of hydrogenic level n . n_n^* is the LTE population of level n [cm^{-3}], and the other symbols have their usual meaning. Here

$$\chi_n = \frac{I_n}{kT} = \frac{15.7807 \times 10^4 Z^2}{n^2 T} \quad (1.2)$$

where I_n is the ionization threshold for level n and Z is the nuclear charge, the exponent in equation 1 is positive, and the last term holds for hydrogenic systems. The dimensionless

departure coefficients are related to the LTE relative population density by

$$b_n = \frac{n_n}{P_n^* n_e n_{ion}} \quad (1.3)$$

where n_n is the actual population of the level.

1.3 Pressure lowering of the ionization potential

Not yet

1.4 Recombination rates and cooling

This section is taken from [Ferland and Persson \(1989\)](#).

State-specific rates for radiative recombination and radiative recombination cooling are needed for the temperature range $2.8 \text{ K} \leq T \leq 1.001 \times 10^{10} \text{ K}$. The methods and assumptions used to derive these for hydrogenic ions are described here.

1.4.1 Formalism

The Milne relation for the state-specific radiative recombination rate coefficient ($\text{cm}^3 \text{ s}^{-1}$) to a level n can be expressed as ([Brown and Mathews, 1970](#)); [Gould, 1978](#); [Mihalas, 1978](#));

$$\begin{aligned} \alpha_n(T) &= \left(\frac{2\pi m_e k}{h^2} \right)^{-3/2} \frac{8\pi}{c^2} \frac{g_n}{g_e g_{ion}} T^{-3/2} \int_{h\nu_o}^{\infty} \nu^2 \alpha_\nu(n) \exp(-h(\nu - \nu_o)/kT) d\nu \\ &= 4.12373 \times 10^{11} \frac{g_n}{g_e g_{ion}} T^{-3/2} \int_{h\nu_o}^{\infty} \nu_{Ryd}^2 \alpha_\nu(n) \exp(-h(\nu - \nu_o)/kT) d\nu_{Ryd} \end{aligned} \quad (1.4)$$

where the g 's are the statistical weights of the constituents, $h\nu_{Ryd}$ is the photon energy in Rydbergs, $h\nu_o \sim z^2/n^2$ is the ionization potential in Rydbergs, $\alpha_\nu(n)$ is the photoionization cross section, and the other symbols have their usual meanings.

In implementing this formalism the fact that, for hydrogen itself, the energy scale is shifted by the ratio of the reduced mass of the nucleus to an infinite mass was explicitly taken into account. If the energy of level n of hydrogen is $n^{-2}R_H$, then the temperature corresponding to 1 Rydberg, appearing in the exponential, is 157807 K, not the commonly quoted 157890 K. This does affect the results slightly since the energy scale enters as an exponential in equation 1.4.

Hydrogenic photoionization cross sections are required over a very wide range of energy since recombination coefficients over a wide range of temperature are needed. Cross sections $\alpha_\nu(n)$ were calculated using a program based on routines developed by [Hummer \(1988\)](#), [Storey and Hummer \(1991\)](#), and Hummer (private communication). The program generates the cross section values at arbitrary photon energies for all hydrogenic (n, l) states, as well as for the total n , employing analytic expressions and some very accurate expansions and numerical procedures. The calculations were carried out at a number of different mesh sizes to check for convergence. The results are typically accurate to better than 0.1 percent.

Table 1.1: State Specific and Case B Recombination Coefficients

$\log(T_e)$	1	2	3	4	5	6	Case B
0.5	9.258-12	5.087-12	3.512-12	2.684-12	2.172-12	1.825-12	5.758-11
1.0	5.206-12	2.860-12	1.974-12	1.508-12	1.220-12	1.025-12	2.909-11
1.5	2.927-12	1.608-12	1.109-12	8.465-13	6.842-13	5.737-13	1.440-11
2.0	1.646-12	9.028-13	6.216-13	4.732-13	3.811-13	3.183-13	6.971-12
2.5	9.246-13	5.055-13	3.460-13	2.613-13	2.084-13	1.720-13	3.282-12
3.0	5.184-13	2.805-13	1.888-13	1.395-13	1.085-13	8.717-14	1.489-12
3.5	2.890-13	1.517-13	9.779-14	6.884-14	5.099-14	3.912-14	6.430-13
4.0	1.582-13	7.699-14	4.555-14	2.965-14	2.053-14	1.487-14	2.588-13
4.5	8.255-14	3.461-14	1.812-14	1.076-14	6.953-15	4.775-15	9.456-14
5.0	3.882-14	1.316-14	6.059-15	3.314-15	2.022-15	1.331-15	3.069-14
5.5	1.545-14	4.196-15	1.736-15	8.918-16	5.219-16	3.335-16	8.793-15
6.0	5.058-15	1.146-15	4.392-16	2.160-16	1.229-16	7.694-17	2.245-15
6.5	1.383-15	2.760-16	1.005-16	4.807-17	2.685-17	1.660-17	5.190-16
7.0	3.276-16	6.031-17	2.129-17	1.000-17	5.523-18	3.385-18	1.107-16
7.5	7.006-17	1.227-17	4.251-18	1.976-18	1.083-18	6.606-19	2.221-17
8.0	1.398-17	2.377-18	8.139-19	3.759-19	2.052-19	1.248-19	4.267-18
8.5	2.665-18	4.455-19	1.515-19	6.970-20	3.796-20	2.303-20	7.960-19
9.0	4.940-19	8.175-20	2.769-20	1.271-20	6.913-21	4.190-21	1.457-19
9.5	9.001-20	1.481-20	5.005-21	2.294-21	1.247-21	7.552-22	2.636-20
10.0	1.623-20	2.662-21	8.985-22	4.116-22	2.235-22	1.354-22	4.737-21

The recombination cooling rate coefficient ($\text{erg cm}^3 \text{s}^{-3}$) is given by

$$kT\beta(t, n) = \left(\frac{2\pi m_e k}{h^2} \right)^{-3/2} \frac{8\pi}{c^2} \frac{g_n}{g_e g_{ion}} T^{-3/2} \int_{h\nu_o}^{\infty} \nu^2 \alpha_{\nu}(n) h(\nu - \nu_o) \exp(-h(\nu - \nu_o)/kT) d\nu \quad (1.5)$$

1.4.2 Results

The numerical results are presented in Tables 1.4.2 and 1.4.2. The first column of the table gives the log of the temperature. Columns 2 through 7 give the total recombination coefficient for $1 \leq n \leq 6$ summed over l states. The last column gives the case B sum, $2 \leq n \leq 1000$. A very large temperature range is considered for completeness; actually, at very low temperatures three-body recombination predominates for most densities (Bates et al., 1962), while at very high temperatures other processes (i.e., Compton scattering, collisions) dominate the balance and the neutral fraction is vanishingly small.

As tests, these predictions of the recombination rate coefficients are compared with those of (Seaton, 1959), (Ferland, 1980), (Hummer and Storey, 1987), and Martin (1988). Note that the total recombination rate given by Hummer and Storey is the sum of radiative and net three-body recombination. For this comparison their results for a density of 10^2 cm^{-3} were used to minimize the contribution of the second process. The agreement with all of these results is good, usually much better than 1 percent. (Seaton, 1959) calculates the recombination cooling coefficients. The

Table 1.2: State Specific and Case B Recombination Cooling Coefficients

$\log(T_e)$	1	2	3	4	5	6	case B
0.5	4.025-27	2.211-27	1.527-27	1.167-27	9.441-28	7.929-28	2.295-26
1.0	7.158-27	3.932-27	2.713-27	2.072-27	1.676-27	1.406-27	3.595-26
1.5	1.273-26	6.985-27	4.815-27	3.671-27	2.962-27	2.479-27	5.514-26
2.0	2.262-26	1.239-26	8.507-27	6.451-27	5.171-27	4.293-27	8.236-26
2.5	4.015-26	2.184-26	1.483-26	1.107-26	8.708-27	7.074-27	1.187-25
3.0	7.099-26	3.785-26	2.488-26	1.784-26	1.341-26	1.039-26	1.629-25
3.5	1.241-25	6.245-26	3.796-26	2.505-26	1.740-26	1.255-26	2.082-25
4.0	2.094-25	9.195-26	4.856-26	2.845-26	1.795-26	1.198-26	2.395-25
4.5	3.234-25	1.112-25	4.923-26	2.557-26	1.483-26	9.305-27	2.376-25
5.0	4.173-25	1.056-25	3.990-26	1.891-26	1.034-26	6.240-27	1.981-25
5.5	4.149-25	7.981-26	2.698-26	1.208-26	6.389-27	3.771-27	1.390-25
6.0	3.121-25	4.961-26	1.572-26	6.827-27	3.549-27	2.073-27	8.316-26
6.5	1.843-25	2.616-26	8.015-27	3.429-27	1.768-27	1.028-27	4.307-26
7.0	9.016-26	1.204-26	3.628-27	1.541-27	7.917-28	4.591-28	1.967-26
7.5	3.847-26	4.978-27	1.487-27	6.296-28	3.229-28	1.870-28	8.109-27
8.0	1.490-26	1.897-27	5.644-28	2.385-28	1.222-28	7.077-29	3.092-27
8.5	5.397-27	6.811-28	2.023-28	8.541-29	4.375-29	2.533-29	1.115-27
9.0	1.867-27	2.346-28	6.959-29	2.937-29	1.504-29	8.706-30	3.872-28
9.5	6.261-28	7.849-29	2.327-29	9.820-30	5.028-30	2.910-30	1.316-28
10.0	2.057-28	2.575-29	7.633-30	3.220-30	1.649-30	9.543-31	4.436-29

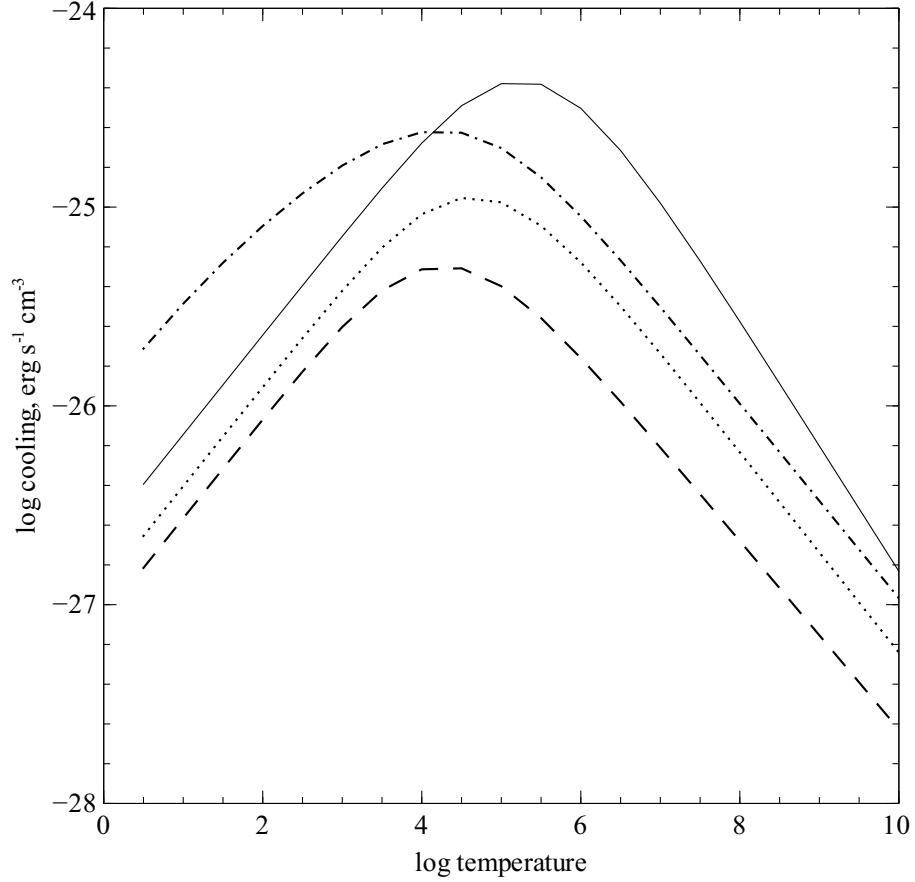


Figure 1.1: The recombination cooling for several states is shown as a function of temperature.

present results agree with his to better than 5 percent. Figure 1.4.2 shows the recombination-cooling coefficient for several states.

1.5 The collisional rate equations

The collision rates between two terms in strict thermodynamic equilibrium (STE) are related by detailed balance. Then

$$n_l^* C_{l,u} = n_u^* C_{u,l} \quad (1.6)$$

and we get the usual relation between collisional excitation and de-excitation rates,

$$C_{l,u} = (n_u^*/n_l^*) C_{u,l} = (g_u/g_l) \exp(-\chi/kT) C_{u,l}. \quad (1.7)$$

Considering only collisional terms, the departure coefficient for level n is given by

$$\frac{db_n}{dt} = \sum_l b_l C_{n,l} + \sum_u \frac{P_u^*}{P_n^*} b_u C_{u,n} - b_n \left\{ \sum_l C_{n,l} + \sum_u \frac{P_u^*}{P_n^*} C_{u,n} + C_{n,k} (1 - b_n^{-1}) \right\} \quad (1.8)$$

where the sums are over upper and lower levels. The collision rates (s^{-1}) from level i to level j are denoted by C_{ij} . The first term on the RHS represents collisional excitation to n from lower

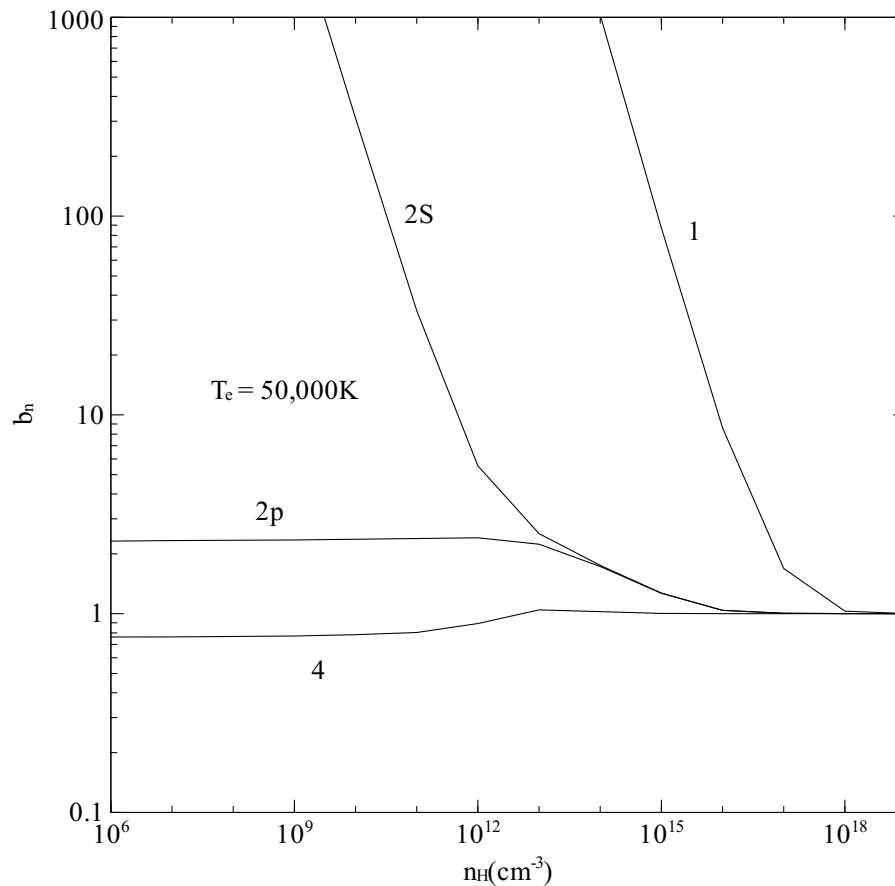


Figure 1.2: The equilibrium populations of the ground state and levels $2s$, $2p$, and 4 of the model hydrogen atom are shown as a function of the total hydrogen density n_H .

levels, the second is collisional deexcitation to n from higher levels, and the last term accounts for destruction processes. These include collisions to lower levels, upper levels, and the continuum. The factor multiplying the collisional ionization rate $C_{n\kappa}$ accounts for collisional ionization less three-body recombination. Note that this is often a net recombination process for the atom since, under many circumstances, $b_n < 1$.

Figure 1.5 shows a test case where collisional processes are dominant. All of the radiative processes discussed below are actually included, but the intensity of the external continuum is set to a very low (and hence negligible) value. As a result collisional and spontaneous radiative processes are dominant. The electrons are given a temperature of 50000 K, and the level populations and ionization of the gas are determined by solving the full set of equations of statistical equilibrium. The model is of a very thin cell of gas that is optically thin in the lines and continuum. Departure coefficients for the ground state, $2s$, $2p$, and 4 are shown.

The radiation field is set to a very low intensity, and the column density is kept small enough for optical depth effects to be negligible. A constant electron temperature of 5×10^4 K is assumed, so the gas is primarily collisionally ionized and excited. Levels $2s$ and $2p$ do not mix until a density of nearly 10^{14} cm^{-3} is reached, and do not come into LTE until the density is nearly 100 times higher. The entire atom is nearly in LTE at densities greater than 10^{18} cm^{-3} .

The ground state is overpopulated relative to its LTE value when upward collisional processes are much slower than downward radiative processes. It is only when the collisional rates approach the radiative rates that b_1 approaches unity. The $2s$ level also has a large overpopulation for much the same reason. It is highly metastable and accumulates a large overpopulation until $2s - 2p$ collisions become fast enough to mix the two l levels. The more highly excited levels ($n \geq 3$) have a behavior very similar to that of $n = 4$, which is shown in the figure. They are under populated relative to their LTE value when radiative decays to lower levels are competitive with collisional processes. It is only at a density of $n_H > 10^{18} \text{ cm}^{-3}$ that collisional processes completely dominate the rate equations and the atom reaches LTE. The mean departure coefficient at a density of 10^{19} cm^{-3} is $\bar{b}_i = 1.0007 \pm 0.0022$ for the entire atom, and the largest single deviation from unity is 0.7% (for the ground level).

1.6 The radiative rate equations

1.6.1 Photoionization—recombination

The photoionization rate (s^{-1}) is given by

$$\Gamma_n = 4\pi \int_{\nu_o}^{\infty} \frac{J_\nu}{h\nu} \alpha_\nu d\nu \quad [\text{s}^{-1}] \quad (1.9)$$

and the induced recombination rate coefficient by

$$\alpha(\text{ind}) = P_n^* 4\pi \int_{\nu_o}^{\infty} \frac{J_\nu}{h\nu} \alpha_\nu \exp(-h\nu/kT) d\nu \quad [\text{cm}^3 \text{s}^{-1}]. \quad (1.10)$$

This is evaluated at each zone by direct integration.

The ground level also includes destruction due to bound Compton scattering.

1.6.2 Derivation of radiative balance equations

Consider the balance for a level n of a three level system, with upper and lower levels u and l .

$$n_n (B_{n,u}\bar{J} + B_{n,l}\bar{J} + A_{n,l}) = n_u (B_{u,n}\bar{J} + A_{u,n}) + n_l B_{l,n}\bar{J}. \quad (1.11)$$

Converting densities n_i into departure coefficients, $n_i = b_i P_i^*$, we obtain

$$P_n^* b_n (B_{n,u}\bar{J} + B_{n,l}\bar{J} + A_{n,l}) = P_u^* b_u (B_{u,n}\bar{J} + A_{u,n}) + P_l^* b_l B_{l,n}\bar{J}. \quad (1.12)$$

Gathering LTE densities we find

$$b_n (B_{n,u}\bar{J} + B_{n,l}\bar{J} + A_{n,l}) = \frac{P_u^*}{P_n^*} b_u (B_{u,n}\bar{J} + A_{u,n}) + \frac{P_l^*}{P_n^*} b_l B_{l,n}\bar{J}. \quad (1.13)$$

Writing $B_{ln} = B_{nl}g_n/g_l$, we obtain the final form

$$b_n \left(\frac{g_u}{g_n} B_{u,n}\bar{J} + B_{n,l}\bar{J} + A_{n,l} \right) = \frac{P_u^*}{P_n^*} b_u (B_{u,n}\bar{J} + A_{u,n}) + \frac{P_l^*}{P_n^*} b_l \frac{g_n}{g_l} B_{n,l}\bar{J}. \quad (1.14)$$

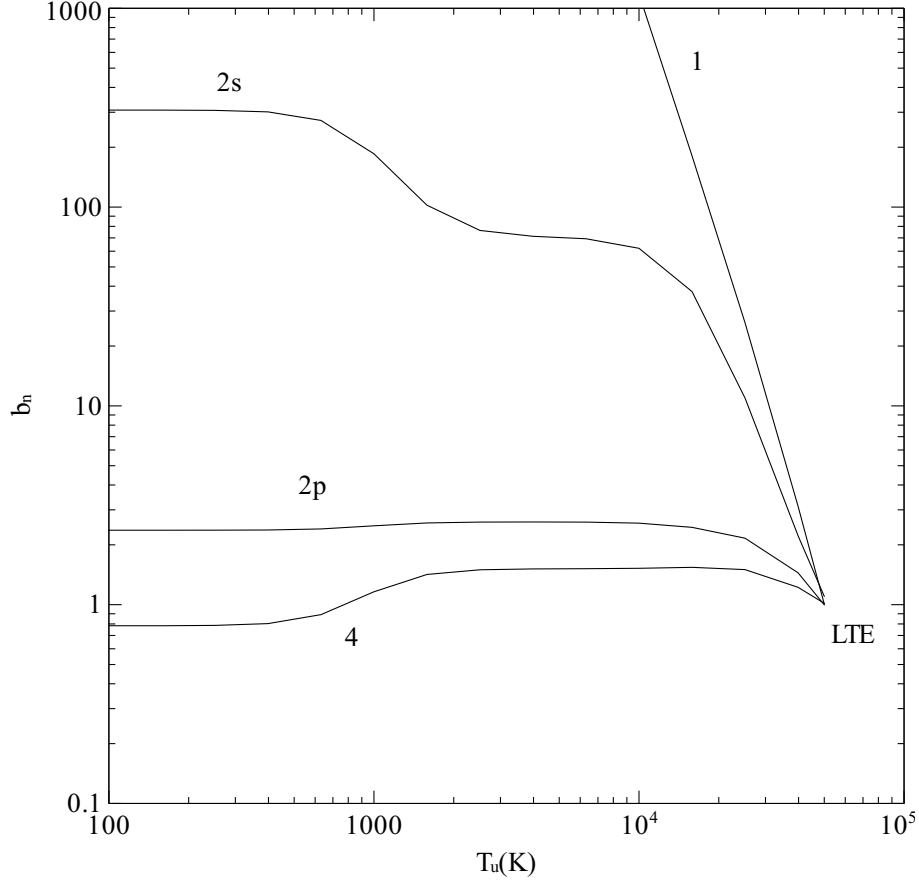


Figure 1.3: The calculations are for a constant temperature ($T = 5 \times 10^4 K$) optically thin gas exposed to black body radiation with a color temperature of $T_{color} = 5 \times 10^4 K$, but with various values of the energy density, parameterized as $T_u = (u/a)^{1/4}$, where u is the actual radiation density.

1.6.3 Final radiative equations

The full set of radiative balance equations can be written as

$$\begin{aligned} \frac{db_n}{dt} = & \sum_l \frac{P_l^*}{P_n^*} b_l A_{n,l} \frac{g_n}{g_l} \eta_{n,l} \gamma_{n,l} + \sum_u \frac{P_u^*}{P_n^*} b_u (A_{u,n} P_{u,n} + A_{u,n} \eta_{u,n} \gamma_{u,n}) + \\ & [\alpha(rad) + \alpha(ind)] / P_n^* - \\ & b_n \left(\sum_l (A_{n,l} P_{n,l} + A_{n,l} \eta_{n,l} \gamma_{n,l}) + \sum_u A_{u,n} \frac{g_u}{g_n} \eta_{u,n} \gamma_{u,n} + \Gamma_n \right) \end{aligned} \quad (1.15)$$

where the η is the continuum occupation number in the transition ij .

Figure 1.6.3 shows a test case that, in contrast to that shown in Figure 1.5, is dominated by radiative transitions.

Again, the full set of equations coupling the levels are solved, but spontaneous and induced processes are more important than collisions for many values of the radiation density. The model is of a very thin cell of gas, so that all lines and continua are optically thin, has a density of $n(H) = 10^{10} \text{ cm}^{-3}$, and an electron temperature of $5 \times 10^4 \text{ K}$. The gas is exposed to a black body continuum with a color temperature of $T_{color} = 5 \times 10^4 \text{ K}$, but the intensity of this continuum is

varied. This intensity is parameterized by an energy density temperature defined by $T_u \equiv (u/a)^{1/4}$ where u and a are, respectively, the actual radiation energy density and Stefan's radiation density constant.

A radiation field given by Planck's law (i.e., $T_u \equiv T_{color}$) forces the ionization and level population of an atom or ion to LTE in much the same way that high electron densities do. As Figure 1.6.3 shows, at very low values of T_u (low photon densities) the ground and $n = 2$ states are overpopulated for much the same reason that this occurs at low electron densities; the downward spontaneous radiative rates are fast relative to the induced (upward and downward) rates. At very low T_u (< 500 K), $n \geq 3$ levels are under populated since they decay at a rate much faster than the induced rates (for $T = 5 \times 10^4$ K these levels have $h\nu \gg kT$, so induced processes will be fast relative to spontaneous rates when $T_u = T_{color}$ and the atom is in LTE). As T_u increases, fluorescence from the ground state over-populates excited states (because the ground state is itself overpopulated) and b_4 exceeds unity. Finally, in the limit where $T_u = T_{color}$, the departure coefficients reach unity and the atom goes to LTE. (The actual mean departure coefficient for the entire atom is $\bar{b}_i = 1.013 \pm 0.029$). Note that the vast majority of the neutral hydrogen population is in excited states when the atom approaches LTE at these temperatures.

The hydrogen density ($n(H) = 10^{10} \text{ cm}^{-3}$) is low enough for radiation to be the main agent affecting level populations for most values of T_u . Fluorescence from the ground state drives the population of $n = 4$ above its LTE value for many radiation densities. Induced processes, mainly transitions between adjacent levels, drive the atom to LTE when T_u reaches 5×10^4 K.

Chapter 2

THE HYDROGENIC ISO-SEQUENCE

Tests in the low-density, or nebular, limit show that the model atom predicts level populations and emissivities that are in much better than 1% agreement with Seaton (1959), and with the Storey and Hummer (1995) results. The atom goes to LTE in the high radiation or matter density limits.

2.1 Recombination rates and cooling

2.1.1 Rational approximations

It is not numerically expedient to compute these rate coefficients on-the-fly in large scale ionization/thermal structure calculations. The rate coefficients were fitted with a high-order rational approximation. The recombination rate coefficient is expressed as

$$\alpha(n, T) = 10^{F(n, T)} T^{-1} \quad (2.1)$$

with

$$F(n, T) = \frac{a_n + c_n x + e_n x^2 + g_n x^3 + i_n x^4}{1 + b_n x + d_n x^2 + f_n x^3 + h_n x^4} \quad (2.2)$$

and $x \equiv \log(T)$. These approximations reproduce the numerical results with a mean error well below 0.1 percent. For levels below $n = 20$ the largest error is also under 0.1 percent, although errors as large as 1.4 percent occur for the highest sum at temperatures below 100 K.

Recombination cooling coefficients were fitted to equations of the form

$$kT\beta(n, T) = 10^{F(n, T)} \quad (2.3)$$

where $F(T, n)$ is given above, and the fitting coefficients are given in the code. The errors in fitting these coefficients are larger, typically 0.5 percent, but sometimes as large as several percent.

2.2 Effective transition probabilities

2.2.1 Einstein As

Two routines are used to compute hydrogenic transition probabilities, in the limit of a completely l -mixed atom. These routines were coded by Jason Ferguson, using algorithms given by [Johnson \(1972\)](#).

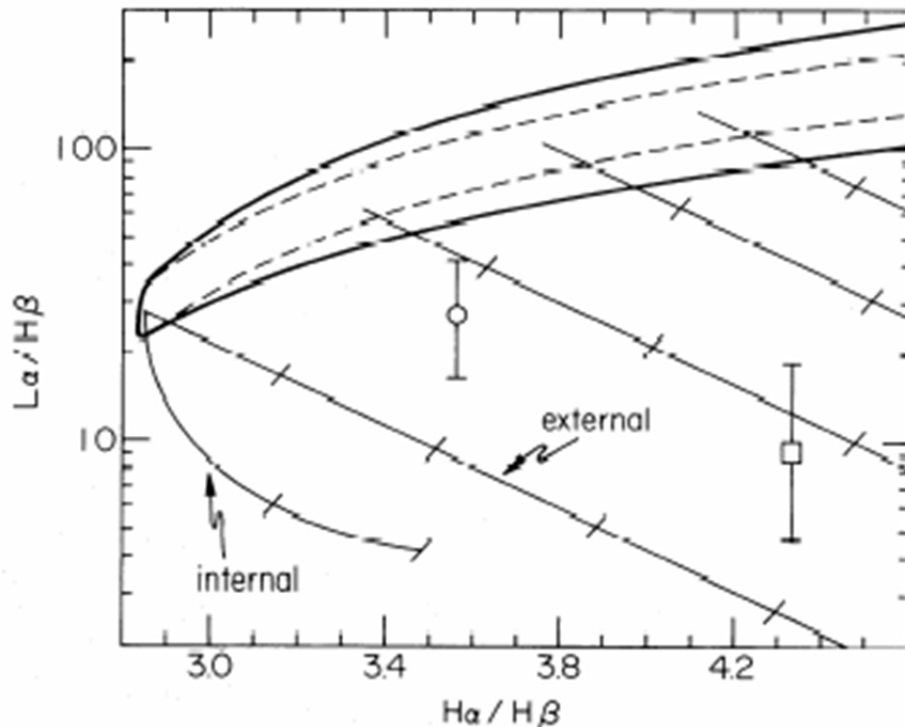


Figure 2.1: This figure, taken from Ferland & Osterbrock 1985, shows the effects of collisional excitation upon two ratios of hydrogen lines. The largest effects are to enhance $L\alpha$ and $H\alpha$ by large amounts.

Note that the code considers the $2s$ and $2p$ as two separate levels. These routines return transition probabilities for a well l -mixed atom, and cannot be applied directly to the separate $2s$ and $2p$ levels.

2.3 Collisional contributions to hydrogen lines

Figure 2.3, taken from Ferland & Osterbrock (1985), shows the effects of collisional excitation on hydrogen lines. This process can be significant relative to recombination when the gas temperature is high (perhaps due to low metallicity) or in partially neutral gas that is exposed to x-rays. The lines marked “external” are reddening curves due to external dust, and “internal” tracks the effects of internal dust. The band of solutions that go across the top of the figure shows the expected hydrogen line spectrum, as set by the collision strengths of the Lyman lines.

2.4 Continuous thermal emission

Diffuse emission (free-free and free-bound) by all atoms is computed using the stored photoabsorption cross sections and detailed balance (i.e., the Milne relation; see [Mihalas, 1978](#)).

Free-bound continua of all levels of hydrogen and helium are treated as follows. The Milne

relation for the emissivity $4\pi j$ ($\text{erg cm}^3 \text{ Hz}^{-1} \text{ s}^{-1}$) can be expressed as (Brown and Mathews, 1970)

$$r\pi j_\nu = h\nu \left(\frac{2\pi m_e k}{h^2} \right)^{3/2} \frac{8\pi}{c^2} \frac{g_n}{g_e g_{ion}} T^{-3/2} \nu^2 \alpha_\nu(n) \exp(-h(\nu - \nu_o)/kT) \quad (2.4)$$

where the statistical weight of level n is $g_n = 2n^2$ for H^0 and He^+ , and $g_n = n^2$ for helium singlets.

The code actually works with units similar to photons $\text{Ryd}^{-1} \text{ s}^{-1} \text{ cm}^{-2}$. The photon emissivity (photons $\text{cm}^3 \text{ s}^{-1} \text{ Ryd}^{-1}$) is then

$$\begin{aligned} \varphi_\nu(T, n) &= \left(\frac{2\pi m_e k}{h^2} \right)^{-3/2} \frac{8\pi}{c^2} \frac{g_n}{g_e g_{ion}} T^{-3/2} \nu^2 \alpha_\nu(n) \exp(-h(\nu - \nu_o)/kT) \\ &= 4.12373 \times 10^{11} \frac{g_n}{g_e g_{ion}} T^{-3/2} \nu_{\text{Ryd}}^2 \alpha_\nu(n) \exp(-h(\nu - \nu_o)/kT) \end{aligned} \quad (2.5)$$

where the g 's are the statistical weights of the constituents, ν_{Ryd} is the photon energy in Rydbergs, $h\nu_o \sim z^2/n^2$ is the ionization potential in Rydbergs, $\alpha_\nu(n)$ is the photoionization cross section, and the other symbols have their usual meanings. Equation 2.5 is evaluated directly using the stored photoionization cross sections. A similar approach is used for all absorption opacities. Detailed balancing between absorption and emission mechanisms is necessary if LTE is to be achieved.

A test case with an ionized hydrogen plasma at a temperature of 10^4 K and a density of 10^7 cm^{-3} (to suppress two photon emission) was computed, and is shown in Figure 2.2.

The input stream used to derive the figure is included in the test suite. As can be seen from this figure, the predicted diffuse continuum is generally within a percent of the exact value (given in Ferland 1980).

Figure 2.3 shows another series of test cases in which a very high density gas with cosmic abundances is irradiated with a $5 \times 10^4 \text{ K}$ blackbody radiation field in strict thermodynamic equilibrium. As can be seen from the figure, the predicted continuum goes to the blackbody limit.

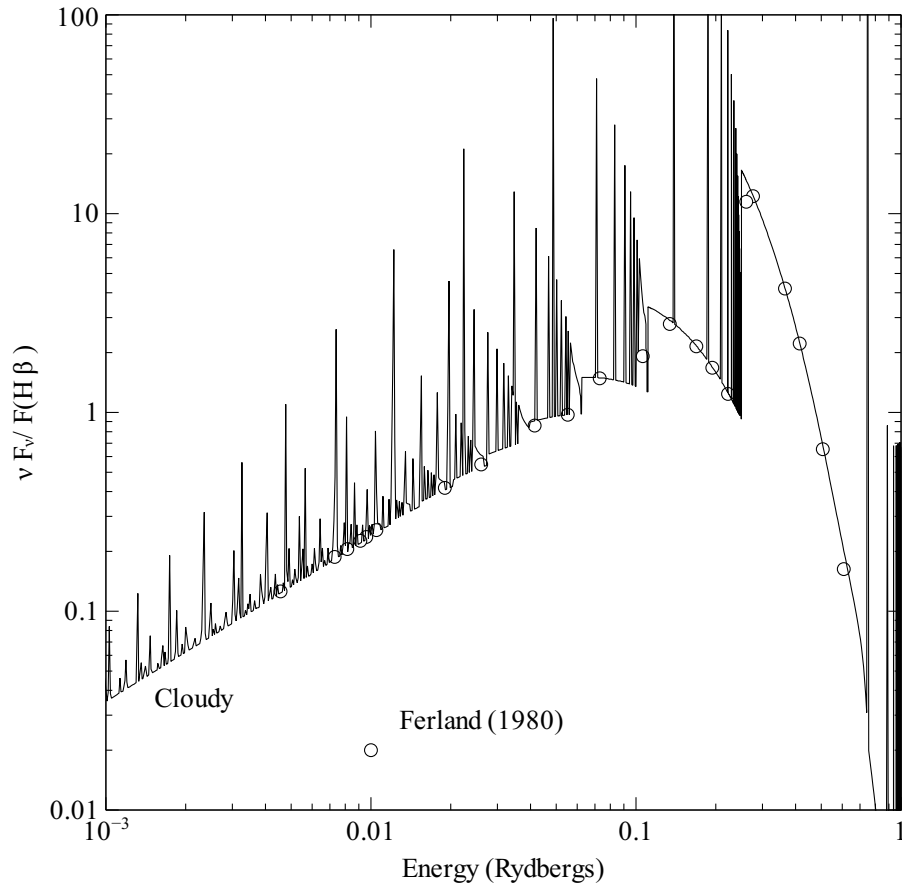


Figure 2.2: The emission from a slab of gas is compared with the predictions of [Ferland \(1980\)](#).

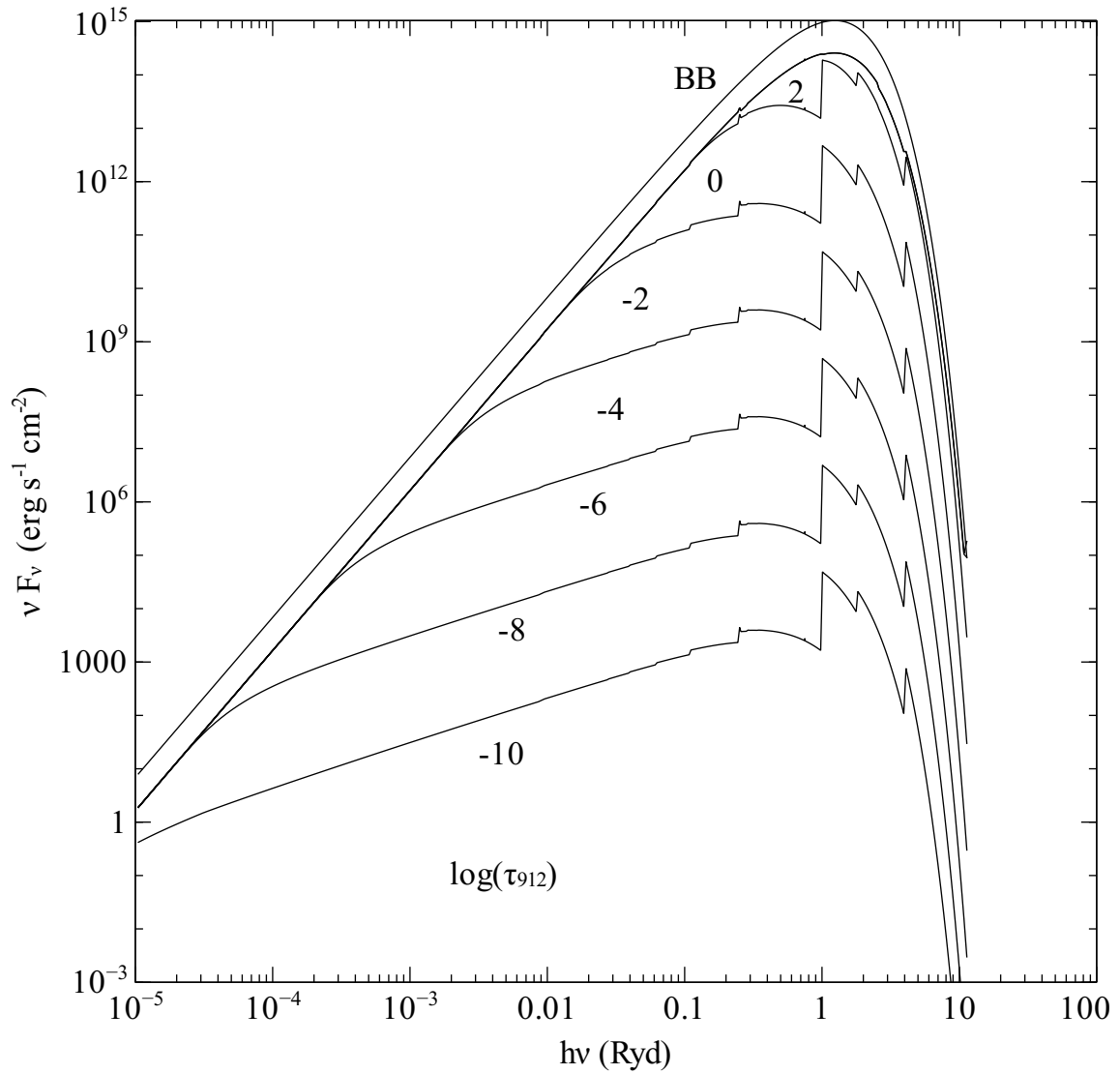


Figure 2.3: The emission from a dense slab of gas with cosmic abundances is shown as a function of the optical depth at the Lyman limit. The log of this optical depth is indicated on the figure. The top curve is for emission given by Planck's law. The continuous emission goes to the blackbody limit in the case of large continuum optical depths.

Chapter 3

HELIUM ISO-SEQUENCE

3.1 Overview

The helium-like isoelectronic sequence is treated with a single unified approach that was developed by Ryan Porter as his PhD thesis. These are published in [Bauman et al. \(2005\)](#), [Porter et al. \(2005\)](#), [Porter et al. \(2007\)](#), and [Porter and Ferland \(2007\)](#)

3.2 Energy levels

Figure 3.2 shows a partial Grotrian diagram for He-like ions. The order of the J levels within $2p\ P^o$ is reversed for the atom; the energy levels shown in Figure 3.2 are for astrophysically abundant ions. In the code the energies associated with a particular J level are always correct, but for He I these occur out of order in the vector of energy levels. This is ok since the levels are so close to having the same energy.

Figure 3.2 compares the energies of the levels within a high- n complex of He I. For comparison, the equivalent hydrogenic energies is drawn as a dotted line. The 1P level is actually above the hydrogenic level but all other He I levels are below, and their energies approach the hydrogen case as the angular momentum increases. Singlets always have higher energies than triplets.

Wavelengths for lines coming from the $n = 2$ complex are listed in Table 3.2

3.3 The He I triplets

The population of the metastable $2s\ ^3S$ level is determined including all processes that create and destroy the level. Processes that destroy $2s\ ^3S$ include photoionization and collisional ionization, radiative decays to ground, and collisional transitions to the singlets. Processes that create populations include three-body and radiative recombination and collisions to the triplets from the singlets. Including only radiative recombination, exchange collisions to the singlets, and radiative decays to ground, the relative population of the 2^3S level of He^0 can be written as

$$\frac{He(2^3S)}{He^+} = \frac{5.79 \times 10^{-6} t_4^{-1.18}}{1 + 3110 t_4^{-0.51} n_e^{-1}} \quad (3.1)$$

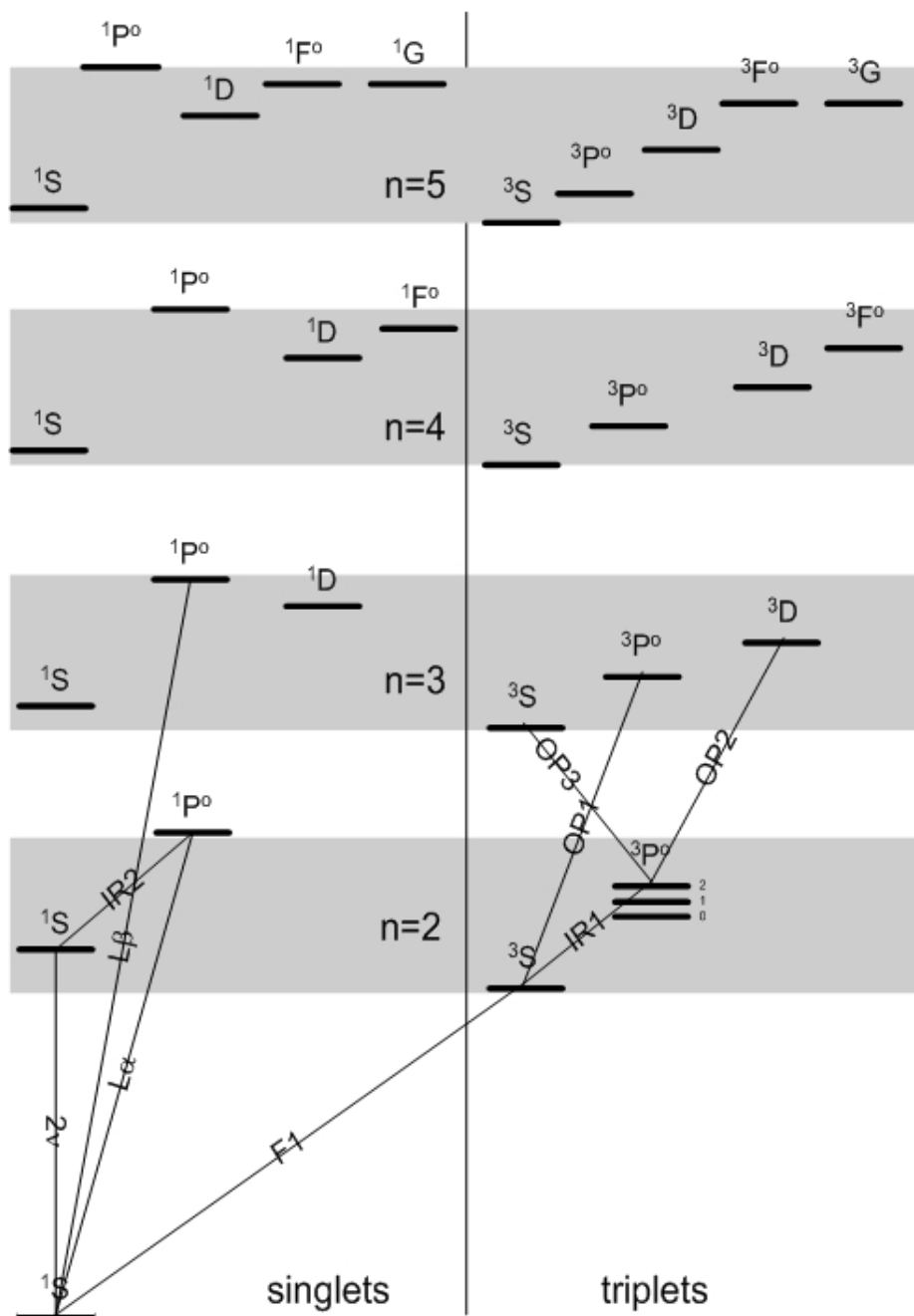


Figure 3.1: A partial Grotrian diagram for the helium iso-electronic sequence.

Table 3.1: Wavelengths of transitions of the He-like sequence

Z	Elem	2^1P-1^1S	$2^3P_1-1^1S$	$2^3P_2-1^1S$	2^3S-1^1S	$2^3P_2-2^3S$	$2^3P_1-2^3S$	$2^3P_0-2^3S$
2	He	584.3A	591.4A	591.4A	625.6A	1.083m	1.083m	1.083m
3	Li	199.3A	202.3A	202.3A	210.1A	5484A	5485A	5483A
4	Be	100.3A	101.7A	101.7A	104.5A	3721A	3723A	3721A
5	B	60.31A	61.09A	61.09A	62.44A	2822A	2826A	2825A
6	C	40.27A	40.73A	40.73A	41.47A	2271A	2278A	2277A
7	N	28.79A	29.08A	29.08A	29.53A	1897A	1907A	1908A
8	O	21.60A	21.81A	21.80A	22.10A	1624A	1638A	1640A
9	F	16.81A	16.95A	16.94A	17.15A	1395A	1414A	1417A
10	Ne	13.45A	13.55A	13.55A	13.70A	1248A	1273A	1278A
11	Na	11.00A	11.08A	11.08A	11.19A	1112A	1142A	1149A
12	Mg	9.169A	9.231A	9.228A	9.314A	997.5A	1034A	1043A
13	Al	7.757A	7.807A	7.804A	7.872A	899.7A	943.2A	954.3A
14	Si	6.648A	6.688A	6.685A	6.740A	814.7A	865.1A	878.6A
15	P	5.760A	5.793A	5.790A	5.836A	740.0A	797.5A	813.2A
16	S	5.039A	5.066A	5.063A	5.102A	673.4A	738.3A	756.3A
17	Cl	4.444A	4.468A	4.464A	4.497A	613.8A	686.1A	706.0A
18	Ar	3.949A	3.969A	3.966A	3.994A	560.0A	639.6A	661.6A
19	K	3.532A	3.550A	3.546A	3.571A	510.7A	596.3A	621.5A
20	Ca	3.177A	3.193A	3.189A	3.211A	466.9A	560.7A	585.9A
21	Sc	2.873A	2.887A	2.883A	2.903A	426.1A	525.1A	553.6A
22	Ti	2.610A	2.623A	2.619A	2.637A	389.5A	496.6A	523.9A
23	V	2.382A	2.393A	2.389A	2.406A	355.8A	469.0A	496.9A
24	Cr	2.182A	2.193A	2.189A	2.203A	325.0A	444.0A	472.1A
25	Mn	2.006A	2.016A	2.012A	2.026A	296.8A	421.1A	449.3A
26	Fe	1.850A	1.860A	1.855A	1.868A	271.2A	400.3A	428.2A
27	Co	1.712A	1.721A	1.716A	1.728A	247.6A	381.2A	408.6A
28	Ni	1.588A	1.597A	1.592A	1.604A	226.3A	363.9A	390.5A
29	Cu	1.478A	1.485A	1.481A	1.492A	206.7A	347.7A	373.5A
30	Zn	1.378A	1.385A	1.381A	1.391A	188.9A	333.0A	357.3A

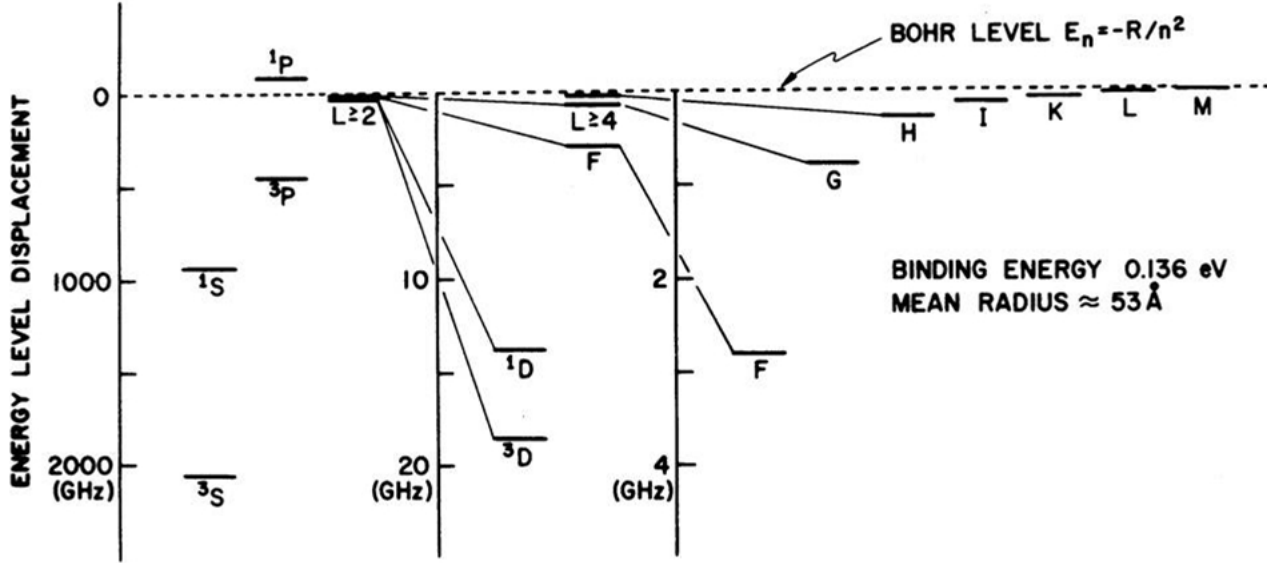


Figure 3.2: A comparison of energies of various states within a high- n state of He0. From Wing & McAdam (1978).

where t_4 is the electron temperature in units of 10^4 K.

3.4 Collapsed versus resolved levels

A level in which all of the spin and angular momentum states are explicitly determined individually is said to be resolved. One in which these are replaced by a single level, with the sublevels assumed to be populated according to their statistical weight, is said to be collapsed. Treating a level as a collapsed levels saves computer time and is appropriate if the density is high enough for collisions to make the state fully l-mixed.

Figure 3.4 shows a plot of the density needed to l-mix a level (the y-axis) vs the principle quantum number (the x-axis). The data are taken from Pengelly and Seaton (1964). This can be used as a guide for adjusting what levels can be treated as the collapsed case.

3.5 Emission from a pure helium gas

Figure 3.5 shows the predicted line and continuous emission for a pure helium gas.

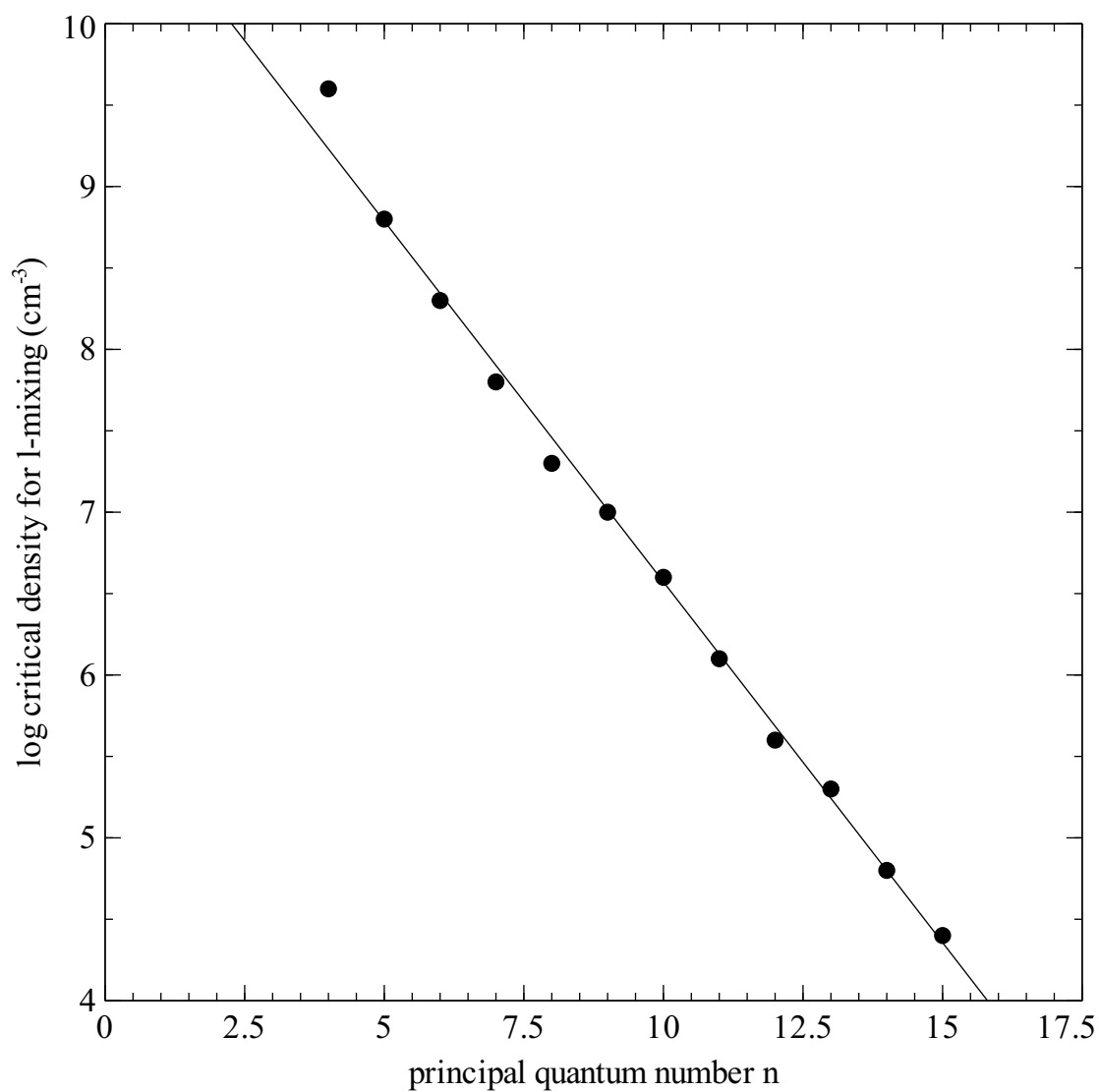


Figure 3.3: The lowest principle quantum number which can be treated as *l*-mixed (the x-axis) is shown versus the density for this to occur (the y-axis). Original data taken from [Pengelly and Seaton \(1964\)](#).

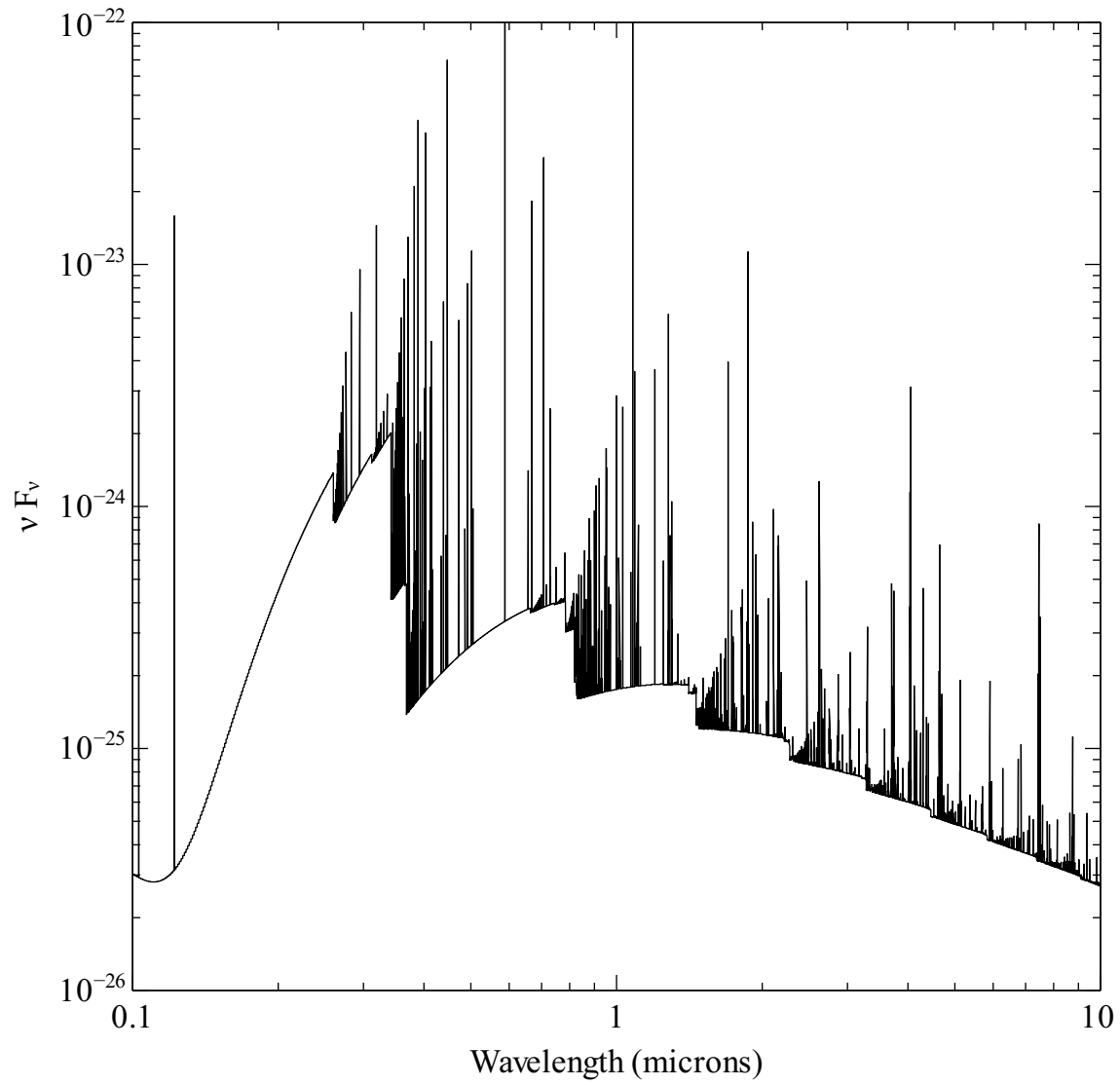


Figure 3.4: The net emission from a pure atomic helium gas at 10^4 K. This is from the calculation `heatomt10.in` in the test suite.

Chapter 4

H⁻ AND MOLECULES

4.1 Overview

An ion-molecule network, initially based on [Black \(1978\)](#) but heavily revised to include a large network, is included in CLOUDY. Aspects are discussed in [Ferland and Persson \(1989\)](#), [Ferland et al. \(1994\)](#), [Ferland et al. \(2002\)](#), [Henney et al. \(2005\)](#), and [Abel et al. \(2005\)](#). [Röllig et al. \(2007\)](#) present the results of a workshop that compared various codes' predictions of conditions in atomic and molecular clouds.

4.2 The Saha equation for arbitrary systems

The Boltzmann equation relates the densities of related species by the expression

$$\frac{n_{final}}{n_{initial}} = \frac{\rho_{final}}{\rho_{initial}} \exp(-\Delta E/kT) \quad (4.1)$$

where $n_{initial}$ and n_{final} indicate the densities of the initial and final states, and the ρ 's are the densities of available states at a given energy. Consider the process $i \Rightarrow j + k$. The energy change during this process is

$$\Delta E = \chi_I + \frac{1}{2}mv^2 \quad (4.2)$$

where the first term is the ionization or dissociation potential of the initial system, and the second term represents the kinetic energy of the system in the final state. The sign of ΔE is related to the energies of the initial and final systems by

$$E_{final} = E_{initial} + \Delta E. \quad (4.3)$$

The ρ 's entering equation 1 are the total densities of states accessible at an energy E . Since the initial state is a bound particle we can take it as at rest in the lab frame, and consider the final state consisting of two constituent particles moving with kinetic energy ΔE . The density of states of the final particles can be written as the product of densities of states due to electron spin and to motion of the particle. Nuclear spins are assumed to be uncorrelated, so nuclear statistical weights cancel out and are not carried through.

Considering only spin and motion (momentum) the total density of states is the spin statistical weight of the particle g_{spin} multiplied by the density of states due to momentum g_p (Mihalas, 1978, p 112; Elitzur, 1992, p 14):

$$\rho_{total} = g_{spin}g_p \quad (4.4)$$

where g_p is

$$g_p = \frac{dx dy dz dp_x dp_y dp_z}{h^3}. \quad (4.5)$$

The volume element can be removed from the problem by defining it as the volume containing one particle,

$$dx dy dz = (n_k/g_k)^{-1} \quad (4.6)$$

while the momentum volume element is given in terms of the particle's speed u by

$$dp_x dp_y dp_z = 4\pi p^2 dp = 4\pi m^3 u^2 du. \quad (4.7)$$

Combining these with equation 4.1 we find

$$\frac{n_{final}n_k}{n_{initial}} = \frac{n_j n_k}{n_i} = \left(\frac{g_{spin,j}g_{spin,k}}{g_{spin,i}} \right) \left(\frac{g_{p,j}g_{p,k}}{g_{p,i}} \right) \exp(-\Delta E/kT). \quad (4.8)$$

Shortening $g_{spin,x}$ to simply g_x , and using equation 4.7, we find

$$\frac{n_j n_k}{n_i} = \left(\frac{g_j g_k}{g_i} \right) \left(\frac{4\pi}{h^3} \frac{m_j^3 u_j^2 \exp\left(-\frac{1}{2}m_j u_j^2/kT\right) du_j m_k^3 u_k^2 \exp\left(-\frac{1}{2}m_k u_k^2/kT\right) du_k}{m_i^3 u_i^2 \exp\left(-\frac{1}{2}m_i u_i^2/kT\right) du_i} \right) \exp(-\Delta E/kT) \quad (4.9)$$

Integrating each energy term over velocity, making the substitution

$$x \equiv \left(\frac{m}{2kT} \right)^{1/2} u, \quad (4.10)$$

we find

$$\int_0^\infty u_j^2 \exp\left(-\frac{1}{2}m_j u_j^2/kT\right) du_j = \left(\frac{2kT}{m_j} \right)^{3/2} \int_0^\infty \exp(-x^2) x^2 dx = \left(\frac{2kT}{m_j} \right)^{3/2} \frac{\pi^{1/2}}{4} \quad (4.11)$$

where the root π over 4 is the value of the integral. The final form of the Saha equation, for an arbitrary system, is:

$$\begin{aligned} \frac{n_j n_k}{n_i} &= \left(\frac{g_j g_k}{g_i} \right) \left(\frac{2\pi kT}{h^2} \frac{m_j m_k}{m_i} \right)^{3/2} \exp(-\Delta E/kT) \\ &= 8.7819 \times 10^{55} \left(\frac{g_j g_k}{g_i} \right) \left(\frac{T m_j m_k}{m_i} \right)^{3/2} \exp(-\Delta E/kT) \end{aligned} \quad (4.12)$$

For the case of ionization producing an electron, the mass of the electron is neglected relative to the mass of the atom. If the atom and ion are i and j , then we have a mass ratio factor that is basically

$$\frac{m_j m_k}{m_i} = \frac{m_{ion} m_e}{m_{atom}} \approx m_e. \quad (4.13)$$

The most common final expression (Mihalas, 1978) includes the assumption that m_i and m_k are nearly identical, and cancel out. In this case we obtain the form of the Saha equation most often encountered for hot gas, with the 2 being the spin statistical weight of the electron:

$$\frac{n_{ion}n_e}{n_{atom}} = \left(\frac{g_{ion}2}{g_{atom}} \right) \left(\frac{2\pi m_e kT}{h^2} \right)^{3/2} \exp(-\Delta E/kT). \quad (4.14)$$

In the case of molecular hydrogen

$$\frac{n_H n_H}{n_{H_2}} = 4 \left(\frac{\pi kT m_p}{h^2} \right)^{3/2} \exp(-\Delta E/kT). \quad (4.15)$$

4.3 LTE Populations of hydrogen molecules

In much of the following discussion comparison and relationships will be made between the predicted hydrogen species populations and their LTE values.

The statistical weight of H_2^+ is 4 while that of H_2 is 1 and the dissociation energies are 2.647 eV and 4.477 eV respectively.

The LTE relative population density of H^- is

$$P^*(H^-) = \frac{n^*(H^-)}{n_e n(H^0)} = \frac{g_{H^-}}{g_{H^0} g_e} \left(\frac{h^2}{2\pi m_e kT} \right)^{3/2} \exp[I(H^-)/kT] \quad [cm^3] \quad (4.16)$$

where g_i is the statistical weight of the constituents, ($g_{H^-} = 1$; $g_{H^0} = 2$; and $g_e = 2$), the binding energy of the negative hydrogen ion is $I(H^-) = 0.055502$ Ryd, and other constants have their usual meaning.

The LTE relative population density of H_2 is

$$P^*(H_2) = \frac{n^*(H_2)}{n(H^0) n(H^0)} = \frac{g_{H_2}}{g_{H^0} g_{H^0}} \left(\frac{h^2}{\pi m_p kT} \right)^{3/2} \exp[I(H_2)/kT] [cm^3] \quad (4.17)$$

4.4 The H^- balance; radiative processes

Although only a trace amount of hydrogen is in the form of H^- , the opacity provided by this ion is often dominant in the optical and near infrared, and it couples energy in the near infrared continuum to moderately ionized gas. The methods and approximations employed to include heating and cooling by H^- are described here. Other discussions can be found in Lambert and Pagel (1968), Vernazza et al. (1981), and Lites and Mihalas (1984). This section is based on Ferland and Persson (1989).

The equilibrium density of H^- is determined by assuming statistical equilibrium, and balancing production and destruction mechanisms. Great care is taken in including both forward and back reactions, to ensure that the present treatment of H^- is capable of going to LTE in the limit of high radiation or particle densities.

4.4.1 Radiative attachment

This is the most important creation mechanism for H^- at low densities, when three-body processes are negligible;



For temperatures greater than 10^4 K the rate coefficient is evaluated by numerically integrating the photodetachment cross section over frequency;

$$\alpha_{rad}(T) = P^*(H^-) \int_{\nu_0}^{\infty} \alpha_{\nu} \frac{8\pi \nu^2}{c^2} \exp(-h\nu/kT) d\nu \quad [\text{cm}^3 \text{s}^{-1}] \quad (4.19)$$

where cross sections computed by [Wishart \(1979\)](#) and spline interpolation are used. These cross sections are in excellent agreement with the velocity operator bound-free cross sections tabulated by [Doughty et al. \(1966\)](#). The energy interval between the photodetachment threshold at 0.055502 Ryd and ~ 1.8 Ryd is divided into a large number of cells with logarithmically increasing width, and the integration is carried out as a straight forward sum.

This method is not numerically expedient for very low temperatures, where the energy bandwidth of the integral is small, and a much finer frequency grid would be required. Rather, the integration was carried out using spline interpolation and 32 point gaussian quadrature, integrating over factors of two in $h\nu/kT$. The results were then fitted with a set of power-laws. The rate coefficients can be approximated by:

$$\alpha(T)_e = \begin{cases} 8.934 \times 10^{18} T^{0.505} & 1K \leq T < 31.62K \\ 5.159 \times 10^{18} T^{0.664} & 31.62K \leq T < 90K \\ 2.042 \times 10^{18} T^{0.870} & 90K \leq T < 1200K \\ 8.861 \times 10^{18} T^{0.663} & 1200K \leq T < 3800K \\ 8.204 \times 10^{17} T^{0.303} & 3800K \leq T < 10^4 K \end{cases} \quad [\text{cm}^3 \text{s}^{-1}] \quad (4.20)$$

These approximations fit the exact numerical results with a mean deviation of 0.7 percent, and the largest error of 2.05 percent, over the indicated temperature range.

Tests show that the numerical radiative attachment rates computed here are in very good agreement with the approximation given by [Hutchins \(1976\)](#), who used the cross sections computed by [Doughty et al. \(1966\)](#), for temperatures $500 \text{ K} \leq T \leq 2500 \text{ K}$. (Notice that there is a typographical error in the approximation for the radiative attachment rate given by [Palla et al. \(1983\)](#).) It is also within 10% of the value given by [Dalgarno and Kingston \(1963\)](#), which was based on earlier calculations of the photodetachment cross section.

Continuum occupation numbers can be large in the infrared. The induced radiative attachment rate coefficient is

$$\alpha_{ind}(T) = P^*(H^-) \int_{\nu_0}^{\infty} \alpha_{\nu} \frac{4\pi J_{\nu}(\tau)}{h\nu} \exp(-h\nu/kT) d\nu \quad [\text{cm}^3 \text{s}^{-1}] \quad (4.21)$$

where the mean intensity of the depth-dependent continuum is $J_{\nu}(\tau)$. This expression is used for all temperatures.

4.4.2 Photodetachment

Photodetachment,



is the dominant H⁻ destruction mechanism for many conditions. The rate is evaluated in the standard manner;

$$\Gamma(\text{H}^-) = \int_{\nu_0}^{\infty} \alpha_{\nu}(bf) \frac{4\pi J_{\nu}(\tau)}{h\nu} d\nu \quad [\text{s}^{-1}] \quad (4.23)$$

The integral is evaluated as a sum over the numerically binned continuum. The incident continuum is then attenuated by optical depth increments

$$d\tau(\text{H}^-) = \alpha_{\nu}(bf) n(\text{H}^-) \{1 - \exp(-h\nu/kT)/b_{\text{H}^-}\} f(r) dr \quad (4.24)$$

where b_{H^-} is the departure coefficient for H⁻, $b_{\text{H}^-} \equiv n(\text{H}^-)/n^*(\text{H}^-)$, $f(r)$ is the filling factor, and $n^*(\text{H}^-)$ is the LTE H⁻ density.

4.4.3 Photodetachment by hard photons

The H⁻ photoabsorption cross section increases above $\sim 3/4$ Ryd, energies where excitation of $n \geq 2$ levels is possible. Cross sections that include this process are taken from [Broad and Reinhardt \(1976\)](#). These calculations do not extend to high energies, so I scaled high-energy hydrogen cross sections by the ratio of H⁻ to H⁰ cross sections at 18Å in order to take absorption of x- and γ- rays into account.

The cross section for $(\gamma, 2e^-)$ absorption is much smaller than (γ, e^-) ([Broad and Reinhardt, 1976](#)), and this latter process is neglected.

4.4.4 The approach to LTE; high radiation densities

As a test of the assumptions and methods, the approach to LTE under conditions determined by radiative attachment (spontaneous and induced) and photodetachment are first considered. Tests in which gas with temperature T is exposed to black body radiation fields with color temperature T_{color} are computed. The color and gas temperatures are set equal, $T = T_{\text{color}}$, and the intensity of the radiation field is varied up to the black body limit. The intensity of the radiation field is parameterized by the equivalent energy density temperature $T_u = (u/a)^{1/4}$, where u is the energy density (erg cm^{-3} ; see above) and a is the Stefan's radiation density constant. The equilibrium population of H⁻ was computed, including all process mentioned below, but with the hydrogen density small enough (typically 10^5 cm^{-3}) for radiative processes to be most important. The H⁻ population is expressed as a departure coefficient, and the results are shown in Figure 4.4.4, for tests in which $T_{\text{color}} = 0.5, 1$, and $2 \times 10^4 \text{ K}$.

When $T_u = T_{\text{color}}$, and the radiation field is in strict thermodynamic equilibrium, radiative processes must hold H⁻ in LTE and departure coefficients of unity are expected. The computed departure coefficients for the three temperatures are 0.9998, 0.9996, and 1.0030, respectively. As the Figure shows, when T_u is lowered below T_{color} , the intensity of the radiation field falls below its thermodynamic equilibrium value, and the population of H⁻ increases. This is because the photodetachment rate (which is proportional to the intensity of the radiation field) is no longer in balance with the radiative attachment rate (which is proportional only to the electron density).

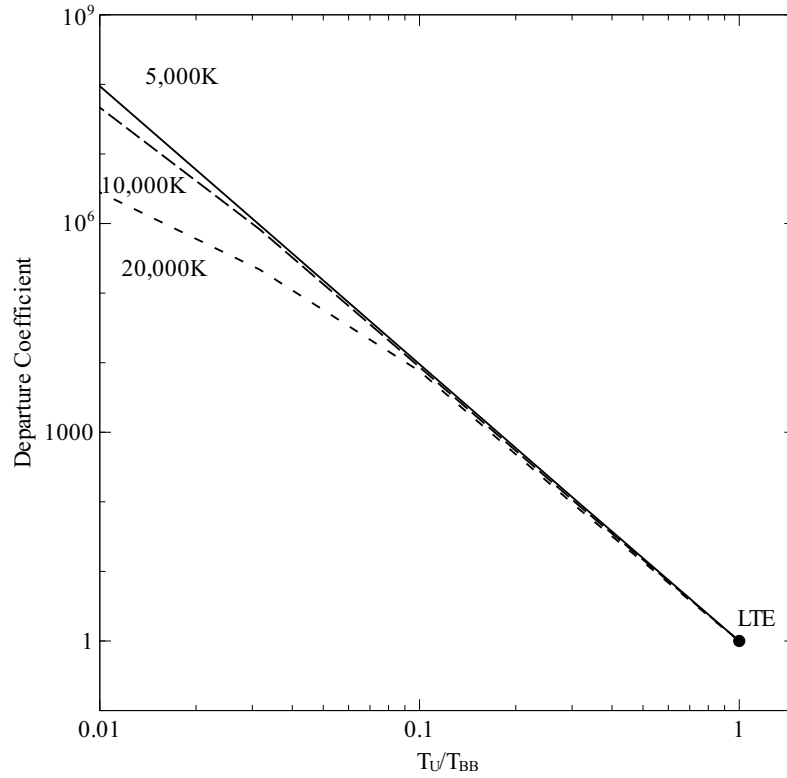


Figure 4.1: Departure coefficients for H^- . The figure shows tests in which the hydrogen density was held fixed at a low and the gas irradiated by black bodies with color temperatures of 5, 10, and 20×10^3 K. Gas temperature and color temperatures were equal. The energy density temperature T_u was varied up to its LTE limit. The H^- departure coefficient is within 0.2% of unity when $T_u = T_{color}$.

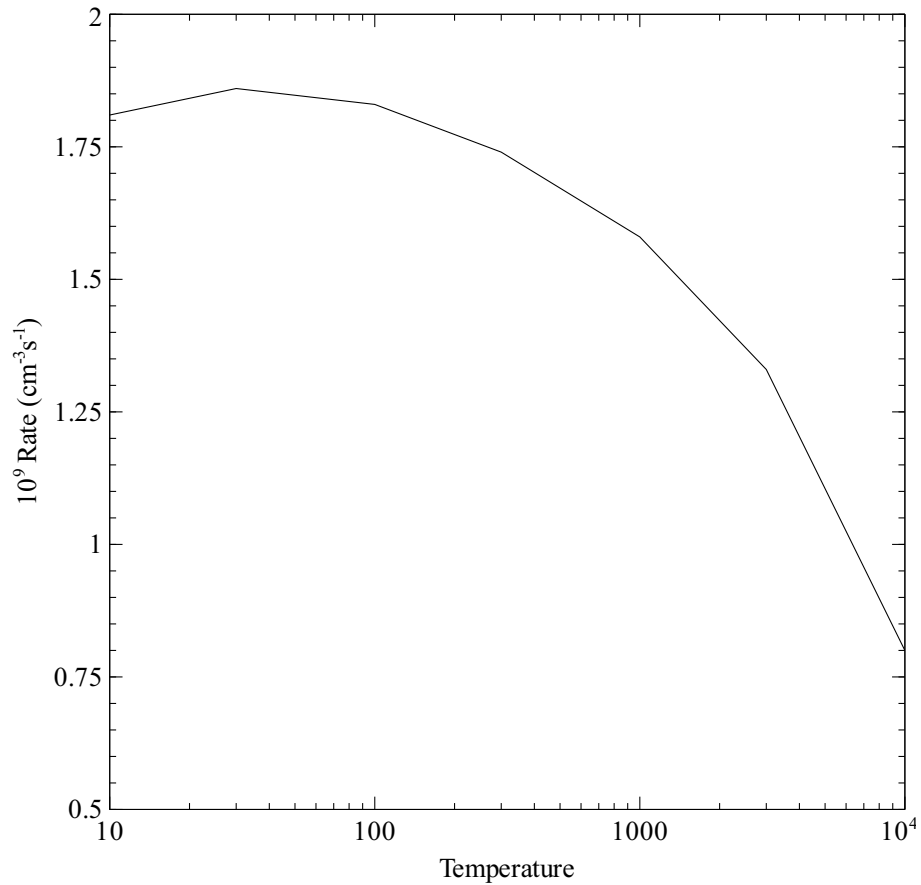


Figure 4.2: Rate coefficient for $\text{H}^- \rightarrow \text{H}_2$. The rates are taken from Launay et al. (1991)

4.5 The H^- balance; collisional processes

4.5.1 Associative detachment

The most important H_2 formation mechanism in grain-free environments, and a significant H^- destruction mechanism, is associative detachment,



where rate coefficients were originally from Bieniek and Dalgarno (1979) and have been updated to Launay et al. (1991). The rate is shown in Figure 4.2. The reverse reaction rate C_R , for electron collisional dissociation of H_2 , is related to the forward rate coefficient C_F by detailed balance;

$$C_R = C_F \frac{P^*(\text{H}^-)}{P^*(\text{H}_2)} \quad [\text{s}^{-1}]. \quad (4.26)$$

4.5.2 Electron collisional detachment

For nebular temperatures ($\sim 10^4$ K) and moderate levels of ionization, the process



is a competitive H^- destruction mechanism. Rates taken from the compendium of [Janev et al. \(1987\)](#) are used. The reverse process, electron three-body recombination with neutral hydrogen, is included via detailed balance;

$$C_R = C_F \frac{P^*(H^-)}{P^*(H^0)} \quad [s^{-1}] \quad (4.28)$$

4.5.3 Collisional ionization by suprathermal electrons

The total suprathermal collisional ionization rate is computed using approximations from [Shull and van Steenberg \(1985\)](#). Ionization of H^- by suprathermal electrons is scaled from the H^0 rates using cross sections at 20 eV given by [Janev et al. \(1987\)](#). This energy was chosen as representative of the mean energy of the secondary electron shower. The majority of these collisions are of the form $e^- + H^- \rightarrow H(1s) + 2e^-$, although $e^- + H^- \rightarrow H^+ + 3e^-$ collisions occur roughly 1% of the time.

4.5.4 Mutual neutralization

Neutral hydrogen can charge transfer with the negative ion through



The rate coefficients given in [Janev et al. \(1987\)](#) are used. By far the largest rate coefficients are for collisions that populate hydrogen in the $n = 3$ level. These rates are based on both experimental and theoretical data (see, for example, [Peart et al. \(1985\)](#)).

The reverse reaction is included using detailed balance. If the rate coefficient for the forward reaction is C_F then the reverse reaction rate, and its rate coefficient C_R , are given by

$$C_F P^*(H^-) P^*(H^+) = C_R P^*(H^0) P^*(H^0) \quad (4.30)$$

where n_i and b_i are the population and departure coefficient of hydrogen in the i th level.

4.5.5 Charge neutralization with heavy elements

The process



is considered by [Dalgarno and McCray \(1973\)](#), who give rate coefficients for very low temperatures and ionization levels. Judging from the curves given by [Peterson et al. \(1971\)](#), upon which the [Dalgarno and McCray \(1973\)](#) rates are based, the approximation they give should still be valid (although very uncertain) at temperatures of general interest ($\sim 0.5 - 1.0 \times 10^4$ K). Here A^+ is all singly ionized species, which are assumed to be neutralized at the same rate.

4.5.6 Neglected processes

Collisional detachment by protons ($p^+ + H^- \rightarrow H + p^+ + e^-$), which has a negligible rate coefficient according to [Janev et al. \(1987\)](#), is neglected, as is collisional detachment by atomic hydrogen ($H^- + H \rightarrow 2H + e^-$), which has no reliable rate coefficient according to [Lites and Mihalas \(1984\)](#).

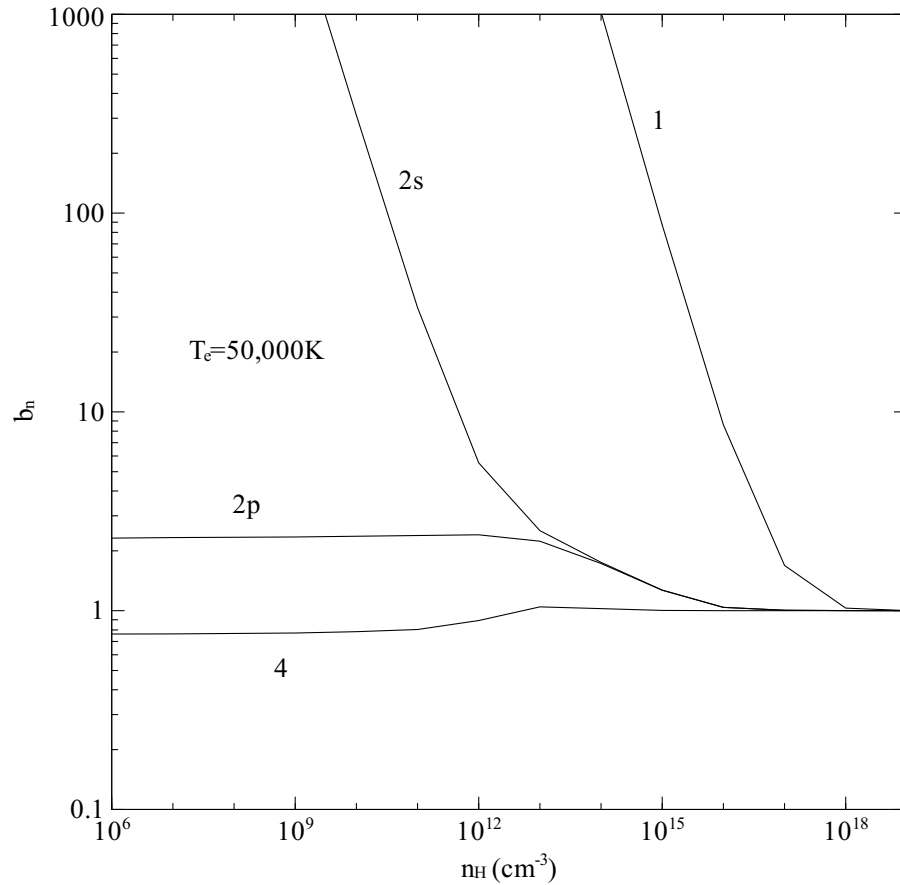


Figure 4.3: Departure coefficients for H^- are shown. The radiation density was low and the total hydrogen density varied. Three gas temperatures are shown. Collisions bring H^- to LTE at high densities.

4.5.7 The approach to LTE; high hydrogen densities

A series of models in collisional equilibrium was computed. Radiative processes were also included, but the incident radiation field, a 10^4 K blackbody, was given a negligible intensity (an ionization parameter of 10^{-12}). Three temperatures, 0.5, 1, and 2×10^4 K, were considered to span the temperature range typical of regions with significant H^- population. The hydrogen density was varied between 10^8 and 10^{18} cm^{-3} to confirm the approach to LTE at high densities. The results of these calculations are shown in Figure 4.3.

For the majority of the calculations hydrogen is largely neutral, and for the smaller temperatures a significant fraction of the hydrogen was in the molecular form (H_2 and H_2^+). The calculation confirms that the departure coefficients are within 2% of unity at the highest densities computed.

4.6 The HeH^+ molecular ion

Rates for radiative association of He and H^+ to form HeH^+ are taken from [Zygelman and Dalgarno \(1990\)](#).

4.7 Linearization of the balance equations

In the case of a molecular balance equation it is common to have a single reaction that is the product of two unknowns. The code works by complete linearization, and uses the following scheme to produce a linear chemical network.

Suppose we have two molecules with abundance a and b , and with previous abundances a_o and b_o . Then $\delta a = a - a_o$; $\delta b = b - b_o$ and the cross terms, ab , can be written as

$$\begin{aligned} ab &= (a_o + \delta a)(b_o + \delta b) \\ &\approx a_o \delta b + b_o \delta a + a_o b_o \\ &\approx a_o(b - b_o) + b_o(a - a_o) + a_o b_o \\ &= a_o b + a b_o - a_o b_o \end{aligned} \quad (4.32)$$

4.8 The H_2 molecule

The treatment of the hydrogen is described in [Shaw et al. \(2005\)](#). Other details are in [Ferland and Persson \(1989\)](#), [Ferland et al. \(1994\)](#), [Ferland et al. \(2002\)](#), and [Abel et al. \(2005\)](#), while [Röllig et al. \(2007\)](#) compare predictions of various codes.

4.8.1 Stoichiometry

The time dependent form of a reaction can be written as

$$\frac{\partial n_i}{\partial t} = n_j R_f - n_i R_d \quad (4.33)$$

where R_f is the rate that species with density n_i is created from a species with density n_j , and R_d is the rate that n_i is destroyed. In the case of hydrogen in the interstellar medium, the dominant formation process is catalysis on grain surfaces, and the dominant destruction process is photodissociation by the Solomon process. This reaction corresponds to the process $2n(\text{H}^0) \rightarrow n(\text{H}_2)$ and H^0 is removed from the gas at twice the rate that H_2 is formed. The balance equation is

$$\frac{\partial n_i}{\partial t} = \frac{1}{2} n(\text{H}^0) n(\text{H}^0) R_f - n(\text{H}_2) R_d. \quad (4.34)$$

The convention in physical chemistry is to include only microphysical processes in a reaction rate coefficient R , and to explicitly write the stoichiometric factors in the equation, as done in equation 4.34.

Tragically, the convention in astrophysics is to write the balance equation as $n(\text{H}^0) n(\text{H}^0) R_f = n(\text{H}_2) R_d$ and absorb the stoichiometric factor of $\frac{1}{2}$ into the rate coefficient. So, the standard or [Jura \(1974\)](#), [Jura \(1975\)](#) rate of H_2 formation of grain surfaces, $3 \times 10^{-17} \text{ cm}^3 \text{ s}^{-1}$ at 100 K, includes a stoichiometric factor of $\frac{1}{2}$.

4.8.2 Associative detachment of H^-

The process



is the main H₂ formation mechanism in low-density grain-free regions, and is treated as described above. At temperatures of interest here ($\sim 10^3$ K) the rate for H₂ formation by this process is set by the rate for radiative association to form H⁻, and is of order 10^{-15} cm³ s⁻¹ (see above).

4.8.3 Catalysis on grain surfaces

The process



is a competitive H₂ formation process when grains are present. The rate coefficient is taken from [Hollenbach and McKee \(1979\)](#) and [Cazaux and Tielens \(2002\)](#). Defining the fraction of atoms which form molecules as

$$f_a = (1 + 10^4 \exp(-600/T_{gr}))^{-1} \quad (4.37)$$

then the rate coefficient is given by

$$\alpha_{gr}(\text{H}_2) = 3 \times 10^{-18} \frac{\sqrt{T} A_{gr} f_a}{1 + 0.04 \sqrt{T_{gr} + T} + 0.002T + 8 \times 10^{-6} T^2} \quad [\text{cm}^3 \text{s}^{-1}] \quad (4.38)$$

where A_{gr} is the grain abundance relative to the ISM value, and T and T_{gr} are the electron and grain temperatures respectively. The grain temperature is determined self-consistently, including radiative and collisional heating and cooling, as described in the section *Grain Physics*.

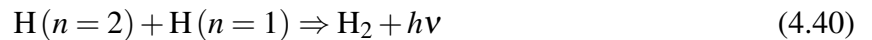
At $T = 10^3$ K and $T_{gr} = 100$ K (representative values of the gas and grain temperature in regions near a H⁰ – H₂ interface) the rate coefficient for grain catalysis is $\sim 4 \times 10^{-18}$ cm³ s⁻¹. For most conditions where carbon is at least once ionized radiative association through H⁻ is at least a competitive H₂ formation mechanism. The ratio of the two processes (referred to as the H⁻ and grain H₂ formation routes) is then

$$\frac{r(\text{H}^-)}{r(\text{grain})} = \frac{n_e \alpha(\text{H}^-)}{n_H \alpha(\text{grain})} \approx \frac{n_e}{n_H} 250 \quad (4.39)$$

i.e., the H⁻ route is faster for conditions of moderate ionization ($n_e/n_H > 4 \times 10^{-3}$) even when grains are present. When grains are absent (or deficient) the H⁻ route dominates.

4.8.4 Excited atom radiative association

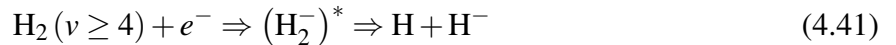
Rates for the process



are taken from [Latter and Black \(1991\)](#).

4.8.5 Excited molecular dissociation

Rates for the process



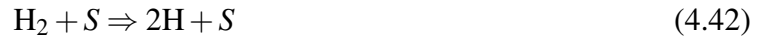
are given in [Janev et al. \(1987\)](#) (their process 2.2.17), and these have been adopted by [Lenzuni et al. \(1991\)](#) and [Crosas and Weisheit \(1993\)](#) in their work on high density gas. Tests show that

this process, if taken at face value, is by far the fastest destruction mechanism for molecular hydrogen under ISM conditions.

The process outlined by [Janev et al. \(1987\)](#) involves an electron capture by H_2 into vibrationally excited levels ($4 \leq v \leq 9$). The process is fast at low temperatures because the energy barrier is small, and the excited levels have large populations at laboratory densities. The process proceeds much more slowly at ISM densities, however, because excited levels have populations below their LTE value. This situation is thus similar to that described by [Dalgarno and Roberge \(1979\)](#). We have modified the [Janev et al. \(1987\)](#) rates using the physics outlined by [Dalgarno and Roberge \(1979\)](#).

4.8.6 Collisional dissociation by H^0 , He^0 , and e^-

The rate coefficient for the forward process, collisional dissociation by the species S (one of H^0 , He^0 , or e^-),



is taken from [Dove and Mandy \(1986\)](#) (dissociation by H^0), [Dove et al. \(1987\)](#) (dissociation by He^0) and [Janev et al. \(1987\)](#) (dissociation by electrons). These can be important destruction mechanisms only for warm regions of the ISM because of the large binding energy of H_2 (~ 50000 K).

The reverse reactions are included via detailed balance. Three-body formation of H_2 is important only for very high densities [$n \cong 10^{10} \text{ cm}^{-3}$].

4.9 Heavy element molecules

4.9.1 Cooling

Cooling due to collisional excitation of vibration-rotation levels of CH , OH , and H_2O is treated using the scheme outlined by HM79.

Of these CO is the most important. ^{12}CO and ^{13}CO are treated as multi-level rigid rotors, with the full spectrum of the ground vibration state predicted.

Chapter 5

THE HEAVY ELEMENTS

5.1 Overview

The code considers all 465 atoms and ions of the lightest 30 elements. The treatment of the ionization equilibrium of ions with more than two electrons is conventional (see AGN3). This treatment is more approximate than that of the H and He iso-sequences because the majority of ions are treated considering only the ground term and continuum for each ionization stage. In all cases, collisional ionization from ground and a net three-body recombination coefficient are included. Photoionization rates are modified for induced recombination as described by equation 1.10. All published charge transfer rate coefficients are also included (Kingdon and Ferland, 1996). Inner shell photoionization is treated using Auger yields given by Kaastra and Mewe (1993). Photoionization cross sections are from Verner et al. (1996a).

This treatment is approximate at high densities for two reasons. First, net radiative recombination coefficients, which have been summed over all levels are used. These sums are correct only in the low-density limit. At high densities levels can undergo collisional ionization before radiative decays to the ground state occur. This brings high levels into LTE, which actually increases the recombination rate. A second problem is that substantial populations can build up in highly excited states when the density and temperature are high. When this occurs, the partition function of the atom or ion is no longer equal to the statistical weight of the ground state. As a result the ionization equilibrium of the heavy elements is approximate for very high densities ($n \gg 10^{10} \text{cm}^{-3}$), with uncertainties increasing for higher densities. The statistical and thermal equilibrium of high-density gas is an area of on-going research.

Many exotic line transfer effects can influence certain lines due to coincidental line overlap. A good general reference to a number of these processes is the paper by Swings and Struve (1940). All of these processes are included in the line formation processes for those lines that are predicted by the code. Morton et al. (1988) and Verner et al. (1996b) provide a line list for UV resonance lines, and Bowen (1960)'s paper on forbidden lines remains a classic.

The effects of resonant structures often dominate collision strengths for infrared transitions. Oliva et al. (1996) and van Hoof et al. (2000) stress the uncertainties these may introduce.

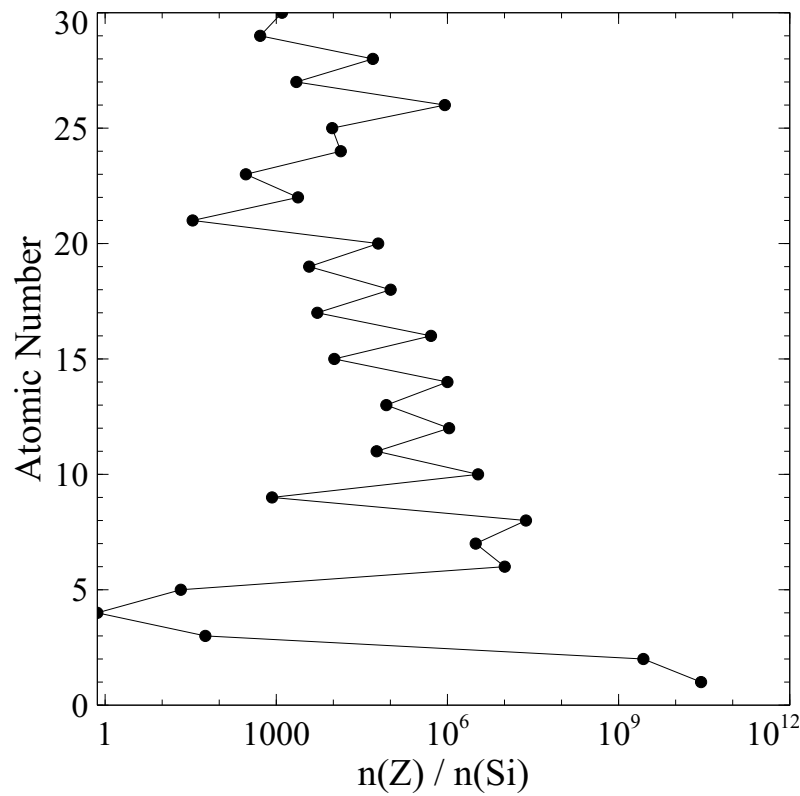


Figure 5.1: Solar system abundances are shown.

5.2 Solar system abundances

Figure 5.2 plots the solar system abundances of the elements, as tabulated by [Allende Prieto et al. \(2001\)](#), [Allende Prieto et al. \(2002\)](#), [Holweger \(2001\)](#) and [Grevesse and Sauval \(1998\)](#). The independent variable is the abundance by number relative to a scale where the abundance of silicon is 10⁶. The dependent variable lists the atomic number and the chemical symbol for the element.

5.3 Periodic table

A periodic table of the first 36 elements follows.

1																	2
H																	He
3	4											5	6	7	8	9	10
Li	Be											B	C	N	O	F	Ne
11	12											13	14	15	16	17	18
Na	Mg											Al	Si	P	S	Cl	Ar
19	20	21	22	23	24	25	26	27	28	29	30	31	32	33	34	35	36
K	Ca	Sc	Ti	V	Cr	Mn	Fe	Co	Ni	Cu	Zn	Ga	Ge	As	Se	Br	Kr

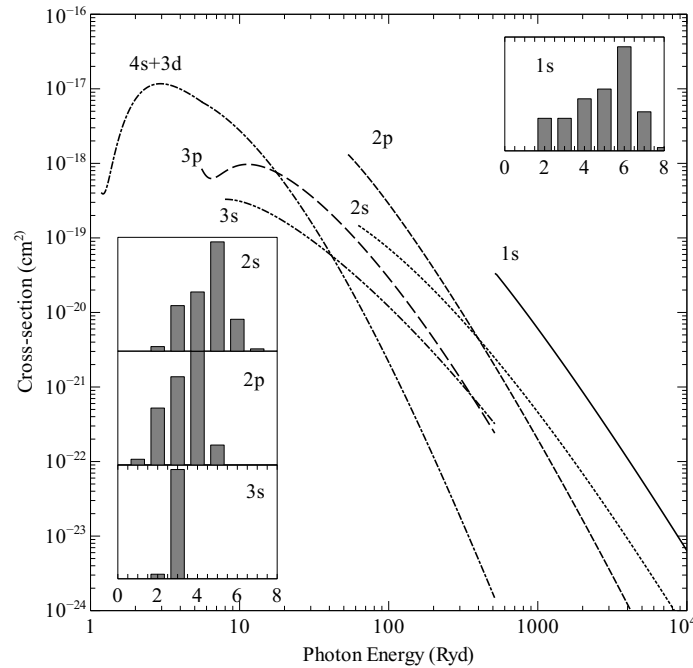


Figure 5.2: Photoionization cross sections and electron yields for singly ionized iron. Each subshell is shown along with the corresponding electron yield.

5.4 Ionization balance

5.4.1 Photoionization cross sections

Photoionization cross sections for all elements are evaluated using Dima Verner's fits to Opacity Project data where possible, and the best theoretical or experimental data for other cases. The fitting procedure is described in [Verner et al. \(1993\)](#), [Verner and Yakovlev \(1995\)](#), and [Verner et al. \(1996a\)](#).

5.4.2 Auger multi-electron ejection

Many electrons may be ejected following removal of an inner electron. This is fully treated using electron yields taken from [Kaastra and Mewe \(1993\)](#). This process couples non-adjacent stages of ionization.

Figure 5.2 shows photoionization cross sections for each shell of singly ionized iron, along with plots of the electron yield, assuming data given by [Kaastra and Mewe \(1993\)](#). A single photoionization of the 1s shell can remove as many as 8 electrons.

5.4.3 Compton scattering ionization of bound electrons

Ionization of outer valence electrons by Compton scattering is treated for all species by assuming that the cross section is the relativistic Compton cross section, multiplied by the number of valence electrons.

Table 5.1: Ionization Potentials of the Elements (Rydbergs)

	1 H	2 He	3 Li	4 Be	5 B	6 C	7 N	8 O	9 F	10 Ne
1	9.996(-1)	1.807	3.963(-1)	6.852(-1)	6.099(-1)	8.276(-1)	1.068	1.001	1.280	1.585
2		4.000	5.559	1.338	1.849	1.792	2.176	2.581	2.570	3.010
3			9.003	1.131(+1)	2.788	3.520	3.487	4.038	4.609	4.664
4				1.600(+1)	1.907(+1)	4.740	5.694	5.689	6.405	7.138
5					2.500(+1)	2.882(+1)	7.195	8.371	8.393	9.275
6						3.601(+1)	4.058(+1)	1.015(+1)	1.155(+1)	1.161(+1)
7							4.903(+1)	5.434(+1)	1.361(+1)	1.524(+1)
8								6.405(+1)	7.011(+1)	1.757(+1)
9									8.107(+1)	8.790(+1)
10										1.001(+2)

5.4.4 Collisional ionization rate coefficients

Fits to collisional ionization rate coefficients are evaluated in Dima Verner's routine *cfit*. These rates come mainly from [Arnaud and Raymond \(1992\)](#) and [Arnaud and Rothenflug \(1985\)](#), and by interpolation where rates are not given.

5.4.5 Charge transfer

Rates for charge transfer between hydrogen and the heavy elements are evaluated using Jim Kingdon's routines. For species more than 4 times ionized, a statistical estimate made by Alex Dalgarno ([Ferland et al., 1997](#)) is used. The rate coefficient for transfer between atomic hydrogen and a highly ionized species is given by $1.92 \times 10^{-9} \zeta \text{ cm}^{-3} \text{ s}^{-1}$, where ζ is the charge of the ion. Other atoms are treated analogously.

All of these include the thermal effects of charge transfer, as described by [Kingdon and Ferland \(1999\)](#).

5.5 Ionization potentials

Table 5.1 lists ionization potentials for photoionization of the outer shell of the first thirty elements. These are given in Rydbergs for infinite mass nuclei.

Figure 5.3 shows the number of ions with valence shell ionization potentials within logarithmically increasing energy widths, as a function of the log of the ionization potentials in Rydbergs. Two large peaks occur, one near ~ 25 Ryd (~ 350 eV) and a second near ~ 160 Ryd (~ 2 keV). The continuum binning used in the code is designed to resolve these as separate features.

5.6 Isoelectronic sequences

Figure 5.4 shows energy-level diagrams for second row iso-sequences. For sequences of elements heavier than K the ground configuration is correct for ions twice or more times ionized. For these heavier elements the atom and first ion may have non-standard configurations for the outer shell.

Table 5.6 lists all isoelectronic sequences for the first thirty elements. The bottom row on the

Table 5.1: Ionization Potentials of the Elements (Rydbergs) – Continued

[illegible]

Table 5.1: Ionization Potentials of the Elements (Rydbergs) – Continued

[illegible]

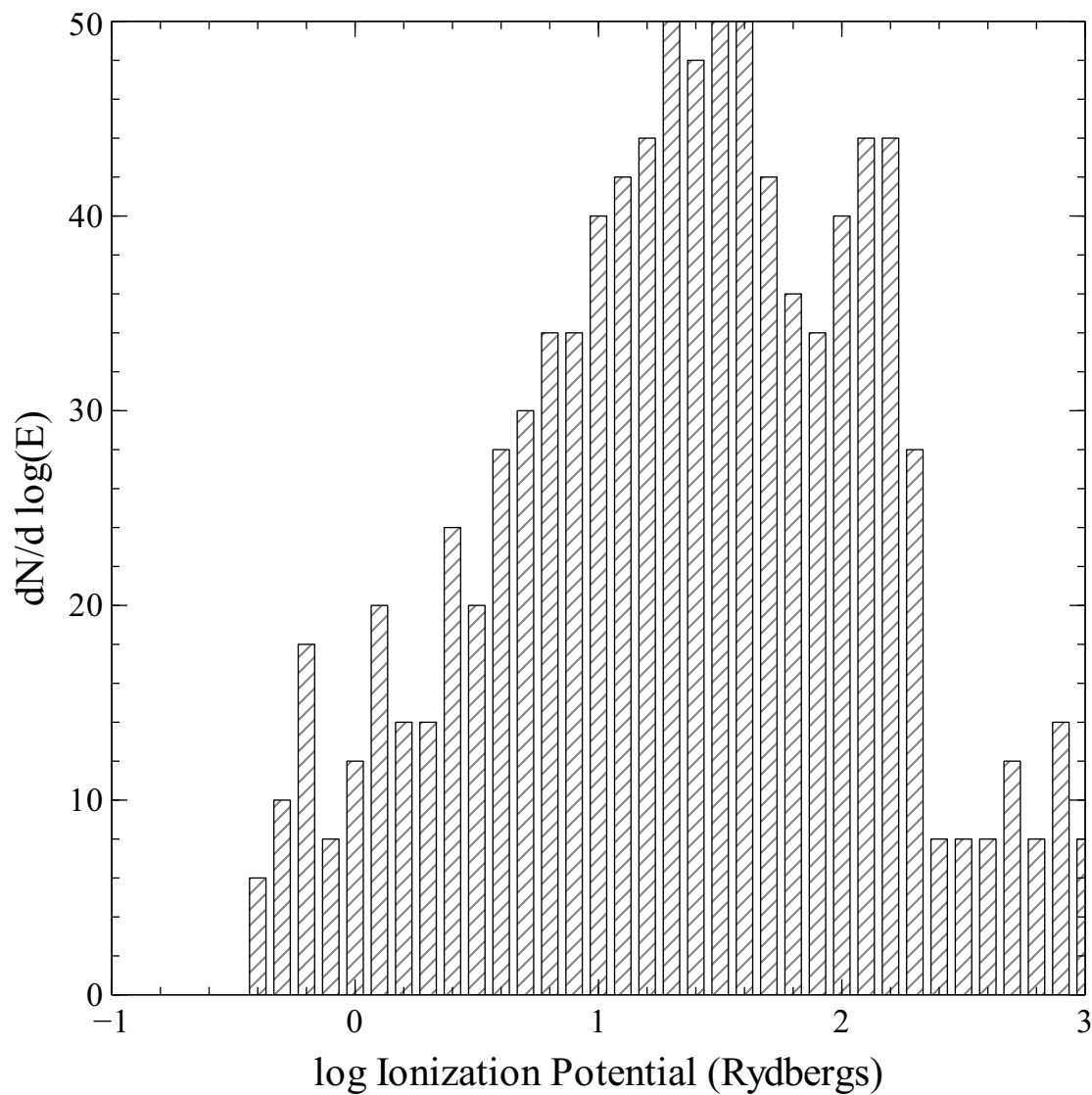


Figure 5.3: The number of elements with valence shell ionization potentials within logarithmically increasing energy widths is shown as a function of the log off the ionization potential.

<p>Li $3/2$ ——— $2P^0$ $2s$ $1/2$ ———</p> <p>$1/2$ ——— $2S$</p>	<p>Be 1 ——— $1P^0$ $2s^2$ 2 ——— 1 ——— $3P^0$ 0 ——— 0 ——— $1S$</p>
<p>B $3/2$ ——— $2D$ $2p$ $5/2$ ——— $5/3$ ——— $4P$ $3/2$ ——— $1/2$ ——— $3/2$ ——— $2P^0$ $1/2$ ———</p>	<p>C 0 ——— $1S$ $2p^2$ 2 ——— $1D$ 2 ——— 1 ——— $3P$ 0 ———</p>
<p>N $1/2$ ——— $2P^0$ $2p^3$ $3/2$ ——— $3/2$ ——— $2D^0$ $5/2$ ——— $3/2$ ——— $4S^0$</p>	<p>O 0 ——— $1S$ $2p^4$ 2 ——— $1D$ 0 ——— 1 ——— $3P$ 2 ———</p>
<p>F $1/2$ ——— $4P$ $2p^5$ $3/2$ ——— $5/2$ ——— $1/2$ ——— $2S$ $1/2$ ——— $2P^0$ $3/2$ ———</p>	<p>Ne 1 ——— $2p^6$ 2 ——— 0 ——— $1S$</p>

Figure 5.4: Energy-level diagrams for the second row isoelectronic sequences. The levels are correct for first ion and higher, but may not be for some atoms, or for ions of elements with more mass than K.

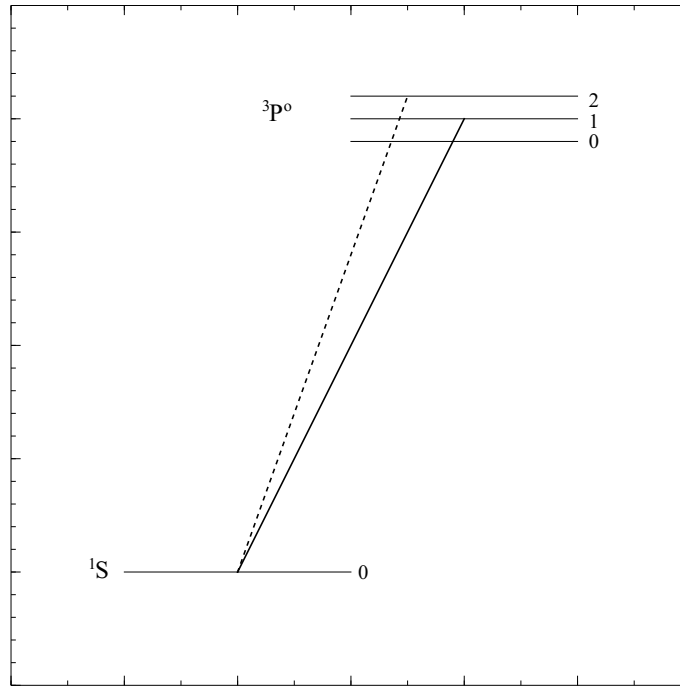


Figure 5.5: The Be-sequence model atom. The permitted transition is marked “UV1,” while the forbidden and intercombination transitions are “For” and “Int.”

table indicates the shell number, in the nomenclature used for the photoionization shell layering¹. A superscript “1” indicates that the atom or first ion has a non-standard configuration in the outer shell.

5.7 Be-sequence

The model atom used for Be-like ions (C III, N IV, O V, Al II, Si III, S IV, etc) is shown in Figure 5.5.

5.8 Carbon

...

5.9 Nitrogen

Photoionization from the excited 2D level of N^0 is included, and can be the dominant ionization mechanism in well-shielded regions.²

¹The arrays within the code count on the C scale so start from 0 and are one less than the index shown in the table.

²Neutral and first ion have non-standard filling.

Table 5.2: Isoelectronic Sequences

1 H	2 He	3 Li	4 Be	5 B	6 C	7 N	8 O	9 F	10 Ne
1s ² S	1s ² ¹ S	2s ² S	2s ² ¹ S	2p ² P	2p ² ³ P	2p ³ ⁴ S	2p ⁴ ³ P	2p ⁵ ² P	2p ⁶ ¹ S
H 1	He 1	Li 1	Be 1	Bo 1	C 1	N 1	O 1	F 1	Ne 1
He 2	Li 2	Be 2	Bo 2	C 2	N 2	O 2	F 2	Ne 2	Na 2
Li 3	Be 3	Bo 3	C 3	N 3	O 3	F 3	Ne 3	Na 3	Mg 3
Be 4	Bo 4	C 4	N 4	O 4	F 4	Ne 4	Na 4	Mg 4	Al 4
Bo 5	C 5	N 5	O 5	F 5	Ne 5	Na 5	Mg 5	Al 5	Si 5
C 6	N 6	O 6	F 6	Ne 6	Na 6	Mg 6	Al 6	Si 6	P 6
N 7	O 7	F 7	Ne 7	Na 7	Mg 7	Al 7	Si 7	P 7	S 7
O 8	F 8	Ne 8	Na 8	Mg 8	Al 8	Si 8	P 8	S 8	Cl 8
F 9	Ne 9	Na 9	Mg 9	Al 9	Si 9	P 9	S 9	Cl 9	Ar 9
Ne10	Na10	Mg10	Al10	Si10	P 10	S 10	Cl10	Ar10	K 10
Na11	Mg11	Al11	Si11	P 11	S 11	Cl11	Ar11	K 11	Ca11
Mg12	Al12	Si12	P 12	S 12	Cl12	Ar12	K 12	Ca12	Sc12
Al13	Si13	P 13	S 13	Cl13	Ar13	K 13	Ca13	Sc13	Ti13
Si14	P 14	S 14	Cl14	Ar14	K 14	Ca14	Sc14	Ti14	V 14
P 15	S 15	Cl15	Ar15	K 15	Ca15	Sc15	Ti15	V 15	Cr15
S 16	Cl16	Ar16	K 16	Ca16	Sc16	Ti16	V 16	Cr16	Mm16
Cl17	Ar17	K 17	Ca17	Sc17	Ti17	V 17	Cr17	Mm17	Fe17
Ar18	K 18	Ca18	Sc18	Ti18	V 18	Cr18	Mm18	Fe18	Co18
K 19	Ca19	Sc19	Ti19	V 19	Cr19	Mm19	Fe19	Co19	Ni19
Ca20	Sc20	Ti20	V 20	Cr20	Mm20	Fe20	Co20	Ni20	Cu 20
Sc21	Ti21	V 21	Cr21	Mm21	Fe21	Co21	Ni21	Cu 21	Zn 21
Ti22	V 22	Cr22	Mm22	Fe22	Co22	Ni22	Cu 22	Zn 22	
V 23	Cr23	Mm23	Fe23	Co23	Ni23	Cu 23	Zn 23		
Cr24	Mm24	Fe24	Co24	Ni24	Cu 24	Zn 24			
Mm25	Fe25	Co25	Ni25	Cu 25	Zn 25				
Fe26	Co26	Ni26	Cu 26	Zn 26					
Co27	Ni27	Cu 27	Zn 27						
Ni28	Cu 28	Zn 28							
Cu 29	Zn 29								
Zn 30									
1	1	2	2	3	3	3	3	3	3

Table 5.2: Isoelectronic Sequences – Continued

11 Na	12 Mg	13 Al	14 Si	15 P	16 S	17 Cl	18 Ar	19 K	20 Ca
3s ² S	3s ² 1S	3p ² P	3p ² 3P	3p ³ 4S	3p ⁴ 3P	3p ⁵ 2P	3p ⁶ 1S	3d ² D	3d ² 3F
Na 1	Mg 1	Al 1	Si 1	P 1	S 1	Cl 1	Ar 1	K 1 ¹	Ca 1 ¹
Mg 2	Al 2	Si 2	P 2	S 2	Cl 2	Ar 2	K 2	Ca 2 ¹	Sc 2 ¹
Al 3	Si 3	P 3	S 3	Cl 3	Ar 3	K 3	Ca 3	Sc 3	Ti 3
Si 4	P 4	S 4	Cl 4	Ar 4	K 4	Ca 4	Sc 4	Ti 4	V 4
P 5	S 5	Cl 5	Ar 5	K 5	Ca 5	Sc 5	Ti 5	V 5	Cr 5
S 6	Cl 6	Ar 6	K 6	Ca 6	Sc 6	Ti 6	V 6	Cr 6	Mm 6
Cl 7	Ar 7	K 7	Ca 7	Sc 7	Ti 7	V 7	Cr 7	Mm 7	Fe 7
Ar 8	K 8	Ca 8	Sc 8	Ti 8	V 8	Cr 8	Mm 8	Fe 8	Co 8
K 9	Ca 9	Sc 9	Ti 9	V 9	Cr 9	Mm 9	Fe 9	Co 9	Ni 9
Ca10	Sc10	Ti10	V 10	Cr10	Mm10	Fe10	Co10	Ni10	Cu 10
Sc11	Ti11	V 11	Cr11	Mm11	Fe11	Co11	Ni11	Cu 11	Zn 11
Ti12	V 12	Cr12	Mm12	Fe12	Co12	Ni12	Cu 12	Zn 12	
V 13	Cr13	Mm13	Fe13	Co13	Ni13	Cu 13	Zn 13		
Cr14	Mm14	Fe14	Co14	Ni14	Cu 14	Zn 14			
Mm15	Fe15	Co15	Ni15	Cu 15	Zn 15				
Fe16	Co16	Ni16	Cu 16	Zn 16					
Co17	Ni17	Cu 17	Zn 17						
Ni18	Cu 18	Zn 18							
Cu 19	Zn 19								
Zn 20									
4	4	5	5	5	5	5	5	6	6

Table 5.2: Isoelectronic Sequences – Continued

[illegible]

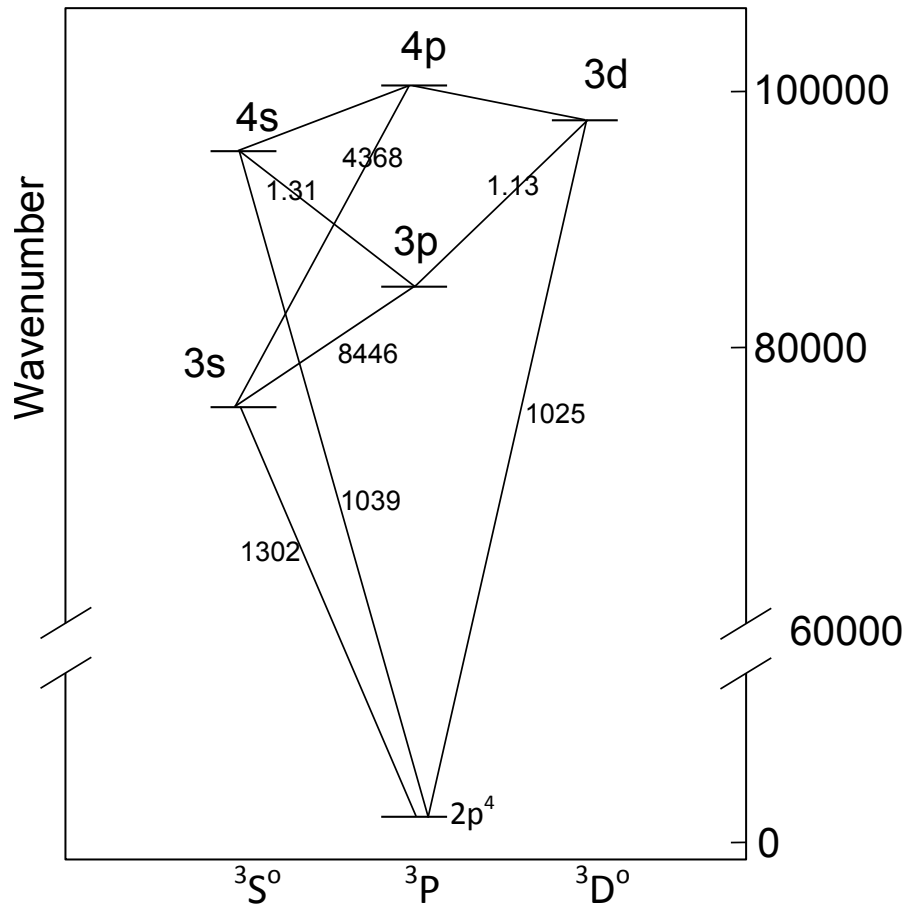


Figure 5.6: The levels of O^o included in the calculation of the $OI-L\beta$ pumping problem are shown.

5.10 Oxygen

Photoionization from the first two excited states of O^{2+} is included as a general ionization mechanism. This can dominate the ionization of the ion since it occurs behind the $He^+ - He^{++}$ ionization front, which shields the region from 4 Ryd and higher radiation. Similarly, photoionization from the first excited state and all inner shells of O^0 are included.

5.10.1 The O I model atom

A partial Grotrian diagram for the O I atom considered in the $L\beta$ -O I fluorescence problem is shown in Figure 5.6. Multiplet averaged transition probabilities are taken from unpublished Opacity Project data, and the collision strengths are from the \bar{g} approximation for collisions between electrons and neutrals. Rates for fluorescence between the two transitions are computed as in Netzer et al. (1985).

5.11 Neon

5.12 Magnesium

Photoionization from the excited $^2P^0$ level of Mg^+ is included as a general Mg^+ destruction mechanism using Opacity Project data retrieved from *TOPBase*. This can easily be the dominant Mg^+ destruction mechanism in dense gas since the excited state has an ionization potential below 1 Ryd. The code will generate a comment at the end of the calculation if this is a competitive Mg^+ destruction mechanism.

5.13 Aluminum

5.14 Calcium

The Ca II ion is treated as a five-level atom plus continuum. The model atom is shown in Figure 5.7, and is similar to that described by Shine and Linsky (1974). Collision strengths for j-mixing collisions are from Saraph (1970). Collision and radiative data for the $4s - 4p$ transition are taken from the compendium of Mendoza (1983), and all other collision data are from Chidichimo (1981) and Saraph (1970). Radiative data for the $3d - 4p$ and $4s - 3d$ transitions are from Black et al. (1972); these are in good agreement with the calculations of Osterbrock (1951). The compendium by Shine and Linsky (1974) provides photoionization cross sections for excited levels, which are adopted here. Photoionization of the excited 2D level by $L\alpha$ (Wyse, 1941) and all other line or continuum sources is explicitly included. Recombination contributions to the population of individual levels are included by dividing the excited state recombination coefficient among the excited levels considered, according to their statistical weight and the rules of LS coupling.

All Ca II transitions (including the forbidden lines) can become quite optically thick. Radiative transfer is treated with the escape probability formalism, assuming incomplete redistribution, including destruction by background opacities.

5.15 Iron

Low temperature dielectronic recombination rate coefficients have not been computed for this element. Means of first-ion rates are used. Charge transfer rate coefficients are from Neufeld (1989) and Ferland et al. (1997).

The Fe II ion is described by Verner et al. (1999) and in sections of Part I of this document. In the current implementation up to 376 levels can be included. This is an area of extensive activity. Figure 5.15 shows the lowest 16 levels of the atom and some of the lines predicted.

Fe IV is treated as a twelve-level atom, with energies from Sugar and Corliss (1985), transition probabilities from Garstang (1958), and collision strengths from Berrington and Pelan (1995). Figure 5.15 shows the model atoms with the lines predicted by the code indicated.

Fe VII is treated as an eight-level system. Figure 5.15 shows the levels and stronger emission lines. Atomic data are from Berrington et al. (2000).

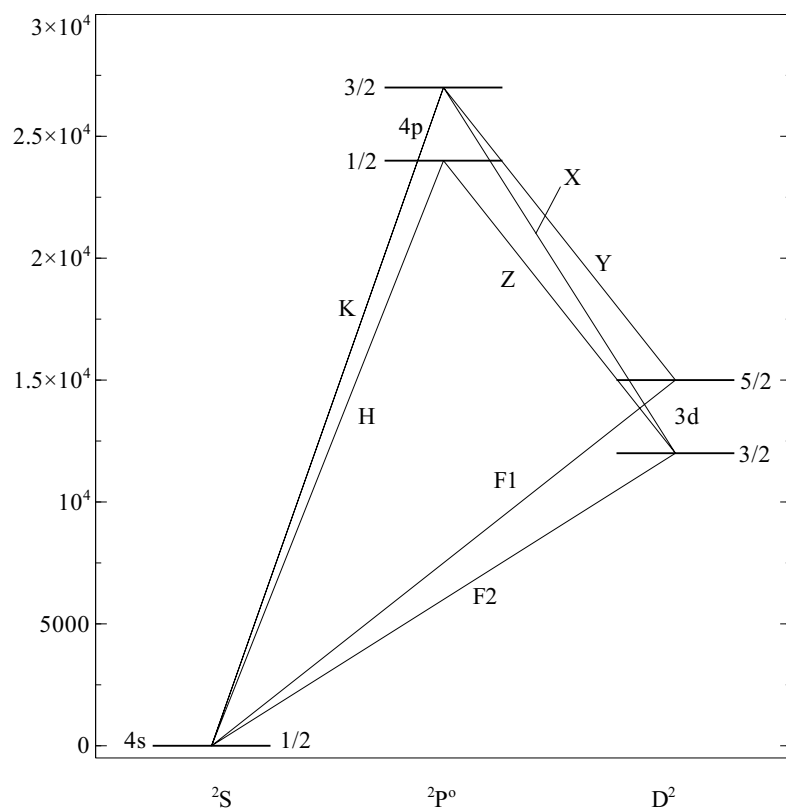


Figure 5.7: The five levels of Ca^+ included in the calculations are shown. The wavelengths of the predicted lines are K (3934), H (3969), X (8498), Y (8542), Z (8662), F1 (7291), and F2 (7324).

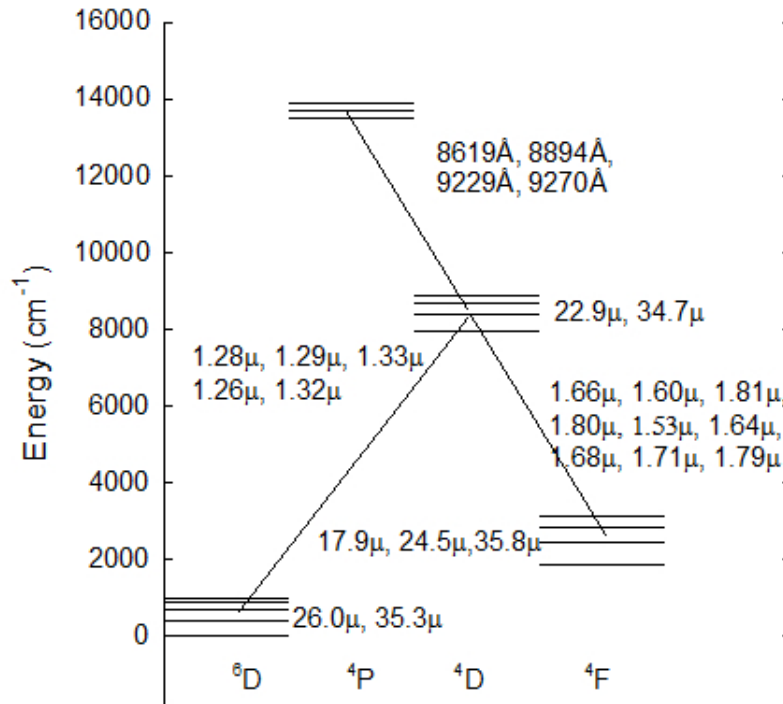


Figure 5.8: The sixteen level atom used to compute Fe II IR emission. Lines predicted are indicated.

5.15.1 Fe K α emission

The intensity of the Fe K α line is predicted including both recombination and fluorescence. Figure 5.15.1 shows the fluorescence yield and K α energy. The line predictions are separated into “cold” iron (i.e., iron with M-shell electrons present) and “hot” iron (those ionization states producing lines with energies greater than ~ 6.4 keV). This includes the recombination and collisional contribution. The “TOTL” K α is the sum of the two.

5.16 Heavy element opacities

Figure 5.16 shows a calculation of the opacity of a solar gas with very low ionization.

5.17 Overall reliability

It is difficult to estimate the overall uncertainty present in an ionization balance calculation. The current photoionization cross-section data are based on accurate experiments or the Opacity Project (Verner et al., 1996a). These should be accurate to roughly 10% except near resonances. Although resonances are included in the Opacity Project data, the positions of these resonances are uncertain by more than their width because the OP was not intended as an atomic structure calculation. Recombination coefficients including low temperature dielectronic recombination have yet to be computed for the majority of the stages of ionization of the elements now in

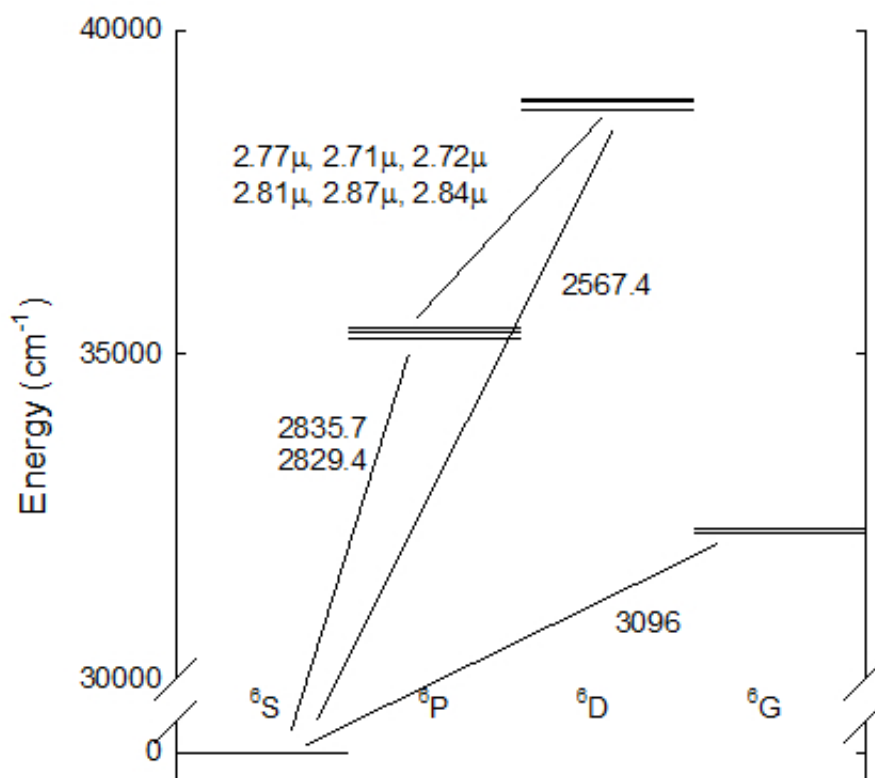


Figure 5.9: The twelve level atom used to compute Fe IV emission. Lines predicted are indicated.

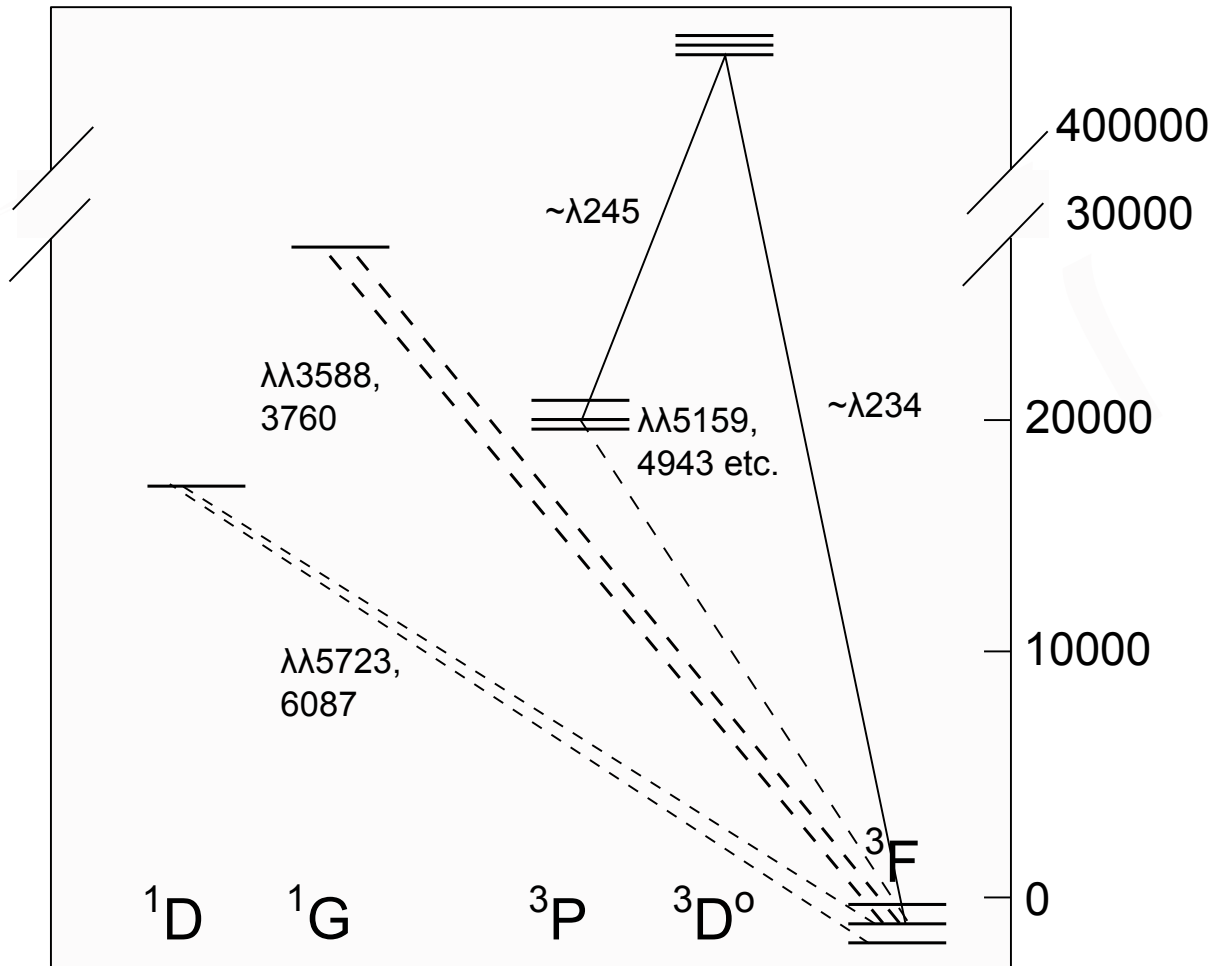


Figure 5.10: The eight-level atom used to compute Fe VII emission. Lines predicted are indicated.

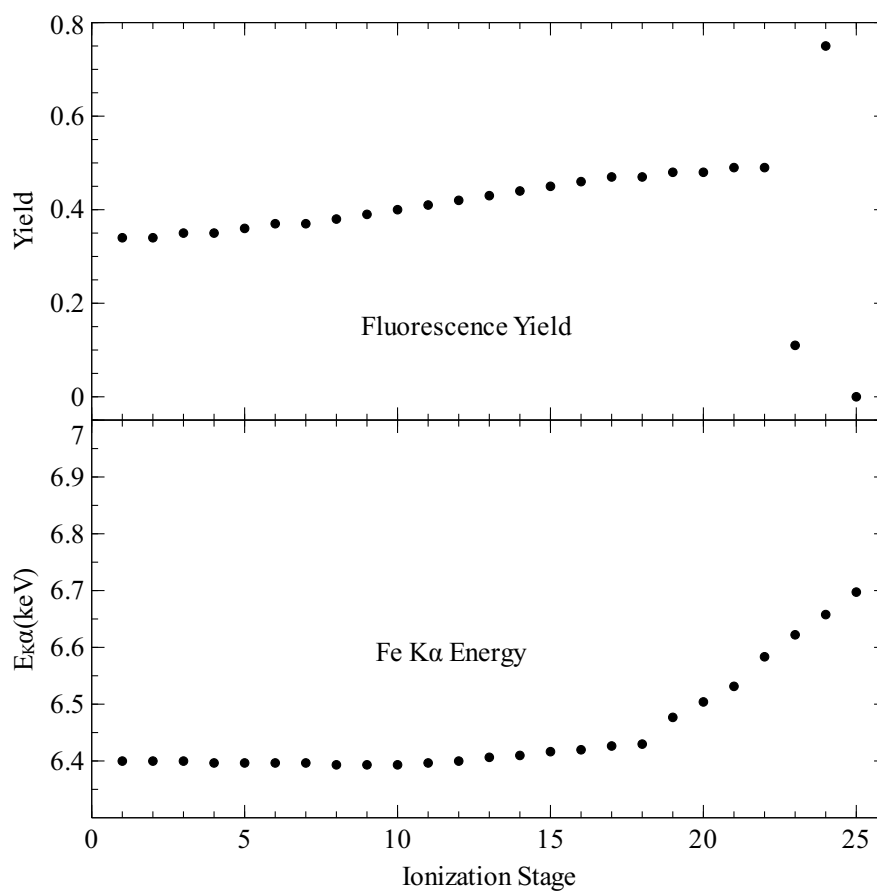


Figure 5.11: The fluorescence yield and energy of the emitted Fe K α photon are shown as a function of ionization stage.

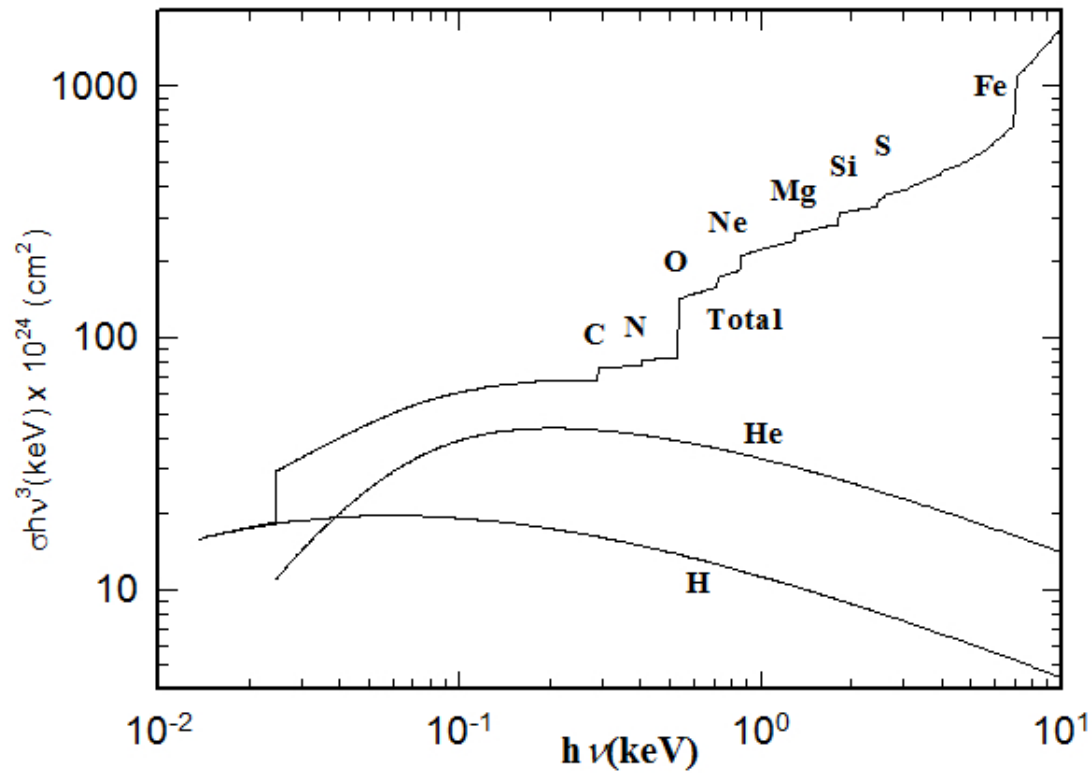


Figure 5.12: The opacity of a neutral gas with solar abundances is shown as a function of energy. The curve is scaled to allow direct comparison with conventional calculations of opacity at X-Ray energies (i.e., [Morrison and McCammon \(1983\)](#)). hevopc

Table 5.3: Ionization Balance Reliability

	1 H	2 He	3 Li	4 Be	5 B	6 C	7 N	8 O	9 F	10 Ne
1	A	A	A	B	B	B	B	B	B	B
2		A	A	A	B	B	B	B	B	B
3			A	A	A	B	B	B	B	B
4				A	A	A	B	B	B	B
5					A	A	A	B	B	B
6						A	A	A	B	B
7							A	A	A	B
8								A	A	A
9									A	A
10										A

CLOUDY, but recombination from parent ions with closed shells is not affected, and good rates exist (Verner and Ferland, 1996).

It is possible to make a subjective estimate of the uncertainty in the calculation of the ionization balance for nebular temperatures. Table 5.3 lists the elements now included in the calculations and gives this estimate of the uncertainty. For recombination from a closed shell autoionization resonances do not occur near threshold, recombination is primarily radiative, and the calculations should be virtually exact. Dielectronic recombination rates are also known for those species treated by Nussbaumer and Storey. These are given a quality weighting of A.

These uncertainties refer to the ionization balance of an optically thin cell of gas at nebular temperatures. The intensities of emission lines will be less uncertain than this for two reasons. First, the thermostat effect of any collisionally excited line prevents its intensity from changing by much. Second is the fact that the integrated column density in an ion is affected as much by (fairly exact) quantities such as the ionization structure of H or He, as by the atomic data of a particular ion. At coronal temperatures the Burgess mechanism dominates, and the situation should be somewhat better.

Nigel Badnell and collaborators have begun a program to compute dielectronic recombination rate coefficients along isoelectronic sequences. These have appeared in a series of papers in A&A starting in 2003. Ions which have been done by Badnell et al. appear as B in the table. They have not yet produced radiative recombination rates.

5.18 Solving the ionization ladder

The rate of change of the density of a particular ionization state i is given by

$$\frac{\partial n_i}{\partial t} = G_i + \sum_{j \neq i} R_{j \rightarrow i} n_j - n_i \left(L_i + \sum_{j \neq i} R_{i \rightarrow j} \right) \quad [\text{cm}^{-3} \text{s}^{-1}]. \quad (5.1)$$

Gains G_i [$\text{cm}^{-3} \text{s}^{-1}$] and losses L_i [s^{-1}] represent physical processes that remove atoms from the ionization ladder. Advection, or molecular processes that create or destroy atoms and ions, are

Table 5.3: Ionization Balance Reliability – Continued

[illegible]

[illegible]

examples. The terms R_{nm} are rates (s^{-1}) for processes that move atoms up or down the ionization ladder.

Several physical processes strongly couple non-adjacent stages of ionization. Charge transfer on grain surfaces and advection are examples. The full system of equations is solved using standard linear algebra methods.

5.19 Ionization potentials of subshells

Table [5.19](#) gives ionization potentials of the subshells.

Table 5.4: Ionization Potentials of Subshells (eV)

Element									
H	1								
1s	13.60								
He	1	2							
1s	24.59	54.42							
Li	1	2	3						
1s	64.39	75.64	122.5						
2s	5.392								
Be	1	2	3	4					
1s	119.3	129.9	153.9	217.7					
2s	9.323	18.21							
B	1	2	3	4	5				
1s	194.0	209.8	227.4	259.4	340.2				
2s	14.05	25.16	37.93						
2p	8.298								
C	1	2	3	4	5	6			
1s	291.0	307.6	328.9	352.2	392.1	490.0			
2s	19.39	30.47	47.89	64.49					
2p	11.26	24.38							
N	1	2	3	4	5	6	7		
1s	404.8	423.6	447.3	475.3	504.3	552.1	667.1		
2s	25.41	37.96	55.45	77.47	97.89				
2p	14.53	29.60	47.45						
O	1	2	3	4	5	6	7	8	
1s	538.0	558.1	584.0	614.4	649.1	683.7	739.3	871.4	
2s	28.48	45.99	65.51	87.37	113.9	138.1			
2p	13.62	35.12	54.94	77.41					
F	1	2	3	4	5	6	7	8	9
1s	694.0	712.2	739.2	770.9	809.1	850.2	890.5	953.9	1103
2s	37.86	54.59	76.10	99.57	126.2	157.2	185.2		
2p	17.42	34.97	62.71	87.14	114.2				

Table 5.4: Ionization Potentials of Subshells (eV) – Continued

Ne	1	2	3	4	5	6	7	8	9	10
1s	870.1	883.1	913.1	948.0	987.3	1031	1078	1125	1196	1362
2s	48.47	63.74	87.21	113.2	141.5	171.9	207.3	239.1		
2p	21.56	40.96	63.46	97.12	126.2	157.9				
Na	1	2	3	4	5	6	7	8	9	10
1s	1079	1097	1118	1143	1185	1230	1281	1335	1386	1465
2s	70.84	73.47	99.45	126.9	156.7	189.9	224.4	264.2	299.9	
2p	38.14	47.29	71.62	98.92	138.4	172.2	208.5			
3s	5.139									
Na	11									
1s	1649									
Mg	1	2	3	4	5	6	7	8	9	10
1s	1311	1320	1336	1356	1400	1449	1501	1558	1618	1675
2s	94.00	98.81	111.1	141.1	173.5	207.6	244.4	283.9	328.2	367.5
2p	54.90	65.69	80.14	109.3	141.3	186.5	224.9	266.0		
3s	7.646	15.04								
Mg	11	12								
1s	1762	1963								
Al	1	2	3	4	5	6	7	8	9	10
1s	1567	1571	1583	1604	1634	1688	1739	1799	1862	1929
2s	125.6	128.1	140.7	155.8	190.3	226.8	266.2	306.5	350.2	399.4
2p	80.40	89.97	102.6	120.0	153.8	190.5	241.4	284.6	330.1	
3s	11.33	18.83	28.45							
3p	5.986									
Al	11	12	13							
1s	1992	2086	2304							
2s	442.1									
Si	1	2	3	4	5	6	7	8	9	10
1s	1846	1848	1852	1868	1887	1946	2001	2058	2125	2194
2s	156.0	161.9	174.4	189.9	207.6	246.8	287.2	331.0	375.6	423.4
2p	106.0	118.6	131.1	146.6	166.8	205.1	246.5	303.2	351.1	401.4
3s	15.17	22.40	33.49	45.143p	8.152	16.35				

Si	11	12	13	14						
1s	2268	2336	2438	2673						
2s	476.1	523.5								
P	1	2	3	4	5	6	7	8	9	10
1s	2154	2155	2157	2173	2192	2214	2280	2337	2407	2477
2s	194.0	198.7	212.4	228.0	246.1	266.3	309.8	355.2	401.8	452.2
2p	140.0	149.5	163.9	179.5	197.7	220.4	263.2	309.4	371.7	424.5
3s	20.17	27.09	38.28	51.44	65.03					
3p	10.49	19.73	30.20							
P	11	12	13	14	15					
1s	2553	2633	2707	2817	3070					
2s	503.5	560.4	611.9							
2p	479.6									
S	1	2	3	4	5	6	7	8	9	10
1s	2477	2478	2486	2502	2522	2544	2569	2641	2705	2782
2s	235.0	238.7	253.6	270.3	288.8	309.4	332.1	379.7	429.6	480.4
2p	170.0	184.6	199.5	216.4	235.0	255.7	280.9	328.2	379.1	447.1
3s	21.30	31.90	44.15	57.50	72.68	88.05				
3p	10.36	23.33	34.83	47.31						
S	11	12	13	14	15	16				
1s	2859	2941	3029	3107	3224	3494				
2s	534.6	590.6	651.7	707.2						
2p	504.8	564.7								
Cl	1	2	3	4	5	6	7	8	9	10
1s	2830	2832	2838	2851	2875	2898	2923	2951	3030	3100
2s	278.0	283.7	297.9	315.1	335.4	356.6	379.7	404.8	456.5	510.9
2p	209.0	223.6	238.2	255.2	276.0	297.4	320.7	348.3	400.1	455.6
3s	25.31	36.86	50.19	64.70	79.97	97.03	114.2			
3p	12.97	23.81	39.61	53.47	67.82					
Cl	11	12	13	14	15	16	17			
1s	3184	3266	3356	3448	3534	3659	3946			
2s	566.0	624.9	684.6	749.8	809.4					
2p	529.3	592.0	656.7							

Table 5.4: Ionization Potentials of Subshells (eV) – Continued

Ar	1	2	3	4	5	6	7	8	9	10
1s	3203	3208	3216	3228	3253	3277	3303	3331	3361	3446
2s	326.0	331.7	345.5	364.2	385.2	407.6	431.4	457.0	484.5	540.3
2p	249.2	266.2	280.1	298.7	320.0	342.6	366.7	392.5	422.5	478.7
3s	28.92	41.98	56.37	71.74	88.28	105.6	124.3	143.5		
3p	15.76	27.63	40.74	59.81	75.02	91.01				
Ar	11	12	13	14	15	16	17	18		
1s	3523	3613	3702	3798	3898	3988	4121	4426		
2s	599.2	658.4	721.7	785.6	854.8	918.0				
2p	539.0	618.3	686.1	755.8						
K	1	2	3	4	5	6	7	8	9	10
1s	3614	3617	3623	3633	3651	3679	3706	3735	3766	3799
2s	384.3	386.7	399.0	416.5	437.4	461.8	486.8	513.3	541.3	571.2
2p	301.4	306.7	327.9	345.2	366.5	390.9	416.2	443.0	471.3	503.8
3s	40.80	47.28	62.69	79.25	96.57	115.2	134.4	154.7	175.8	
3p	24.66	31.63	45.81	60.91	82.66	99.44	117.6			
3d	1.000									
4s	4.341									
K	11	12	13	14	15	16	17	18	19	
1s	3890	3974	4070	4166	4269	4375	4471	4611	4934	
2s	631.0	694.5	757.8	825.5	893.5	968.0	1035			
2p	564.7	629.5	714.7	786.7	861.1					
Ca	1	2	3	4	5	6	7	8	9	10
1s	4043	4047	4053	4063	4078	4105	4133	4163	4198	4229
2s	442.5	444.5	454.2	471.9	494.8	519.3	545.5	573.2	601.8	632.6
2p	352.3	363.8	373.1	394.4	417.5	442.3	468.7	496.7	527.0	556.9
3s	48.30	60.37	69.20	86.80	105.4	124.9	145.2	166.4	188.3	211.3
3p	34.43	40.90	50.91	67.27	84.51	108.8	127.2	147.2		
3d	1.000	1.000								
4s	6.113	11.87								
Ca	11	12	13	14	15	16	17	18	19	20
1s	4265	4362	4453	4555	4659	4767	4880	4982	5129	5470
2s	664.9	728.7	796.8	864.2	935.7	1008	1087	1157		
2p	591.9	657.2	726.7	817.7	894.6	974.5				

Table 5.4: Ionization Potentials of Subshells (eV) – Continued

V	11	12	13	14	15	16	17	18	19	20
1s	5704	5745	5787	5831	5941	6058	6174	6302	6431	6563
2s	874.6	911.4	948.8	988.3	1063	1146	1225	1311	1396	1487
2p	783.4	820.9	858.9	896.0	975.8	1060	1168	1260	1355	
3s	281.0	308.1	336.3							
3p	255.7									
V	21	22	23							
1s	6682	6852	7246							
2s	1570									
Cr	1	2	3	4	5	6	7	8	9	10
1s	5996	6009	6021	6033	6046	6062	6080	6114	6152	6187
2s	703.0	707.4	716.1	733.1	759.8	784.2	814.0	843.2	879.7	910.8
2p	585.0	597.0	616.4	634.4	660.2	685.5	715.3	744.4	781.9	813.0
3s	79.00	87.45	103.2	121.9	142.7	165.6	190.0	214.8	241.9	268.0
3p	49.00	58.79	74.36	92.75	113.4	135.9	160.2	184.7	209.3	244.4
3d	8.660	16.50	30.96	49.16	69.46	90.64				
4s	6.767									
Cr	11	12	13	14	15	16	17	18	19	20
1s	6231	6274	6318	6362	6409	6523	6650	6769	6907	7042
2s	951.2	989.3	1029	1068	1110	1189	1276	1359	1450	1539
2p	854.6	893.3	933.4	973.8	1011	1097	1185	1299	1396	1497
3s	296.9	325.5	354.8	384.2						
3p	270.8	298.1								
Cr	21	22	23	24						
1s	7181	7306	7482	7895						
2s	1634	1721								
Mn	1	2	3	4	5	6	7	8	9	10
1s	6550	6564	6576	6589	6602	6617	6635	6664	6698	6741
2s	781.6	784.9	794.7	811.8	831.9	861.4	890.0	923.0	953.6	993.9
2p	655.4	671.4	682.2	706.3	728.0	756.0	786.0	819.1	849.2	891.03
s	94.60	101.5	112.0	130.0	153.0	176.8	201.6	228.2	254.7	284.0
3p	59.40	70.09	80.62	98.79	121.0	144.4	169.1	194.5	221.8	248.3
3d	14.30	20.58	33.67	51.20	72.40	95.75	119.3			
4s	7.434	15.64								

Table 5.4: Ionization Potentials of Subshells (eV) – Continued

Cu	11	12	13	14	15	16	17	18	19	20
1s	9237	9282	9317	9384	9423	9493	9550	9610	9668	9729
2s	1386	1431	1467	1522	1563	1619	1670	1722	1773	1827
2p	1262	1307	1340	1400	1439	1499	1551	1604	1657	1690
3s	377.8	412.9	445.8	483.8	518.4	557.2	594.9	633.0	670.6	
3p	333.5	368.8	401.0	435.0	484.0	520.0	557.0			
3d	266.1									
Cu	21	22	23	24	25	26	27	28	29	
1s	9844	10040	10160	10360	10530	10700	10850	11060	11570	
2s	1920	2037	2133	2253	2363	2459	2585			
2p	1793	1905	2045	2173	2298					
Zn	1	2	3	4	5	6	7	8	9	10
1s	9667	9691	9713	9733	9751	9770	9788	9809	9831	9854
2s	1203	1209	1222	1239	1259	1298	1323	1362	1397	1436
2p	1037	1065	1077	1101	1129	1162	1193	1227	1267	1302
3s	145.0	147.9	160.1	182.6	207.5	236.9	263.3	296.9	325.7	360.9
3p	97.00	102.1	114.3	136.5	161.2	189.6	216.5	248.7	278.5	312.8
3d	17.30	26.94	39.72	59.40	82.60	108.0	136.0	175.0	203.0	238.0
4s	9.394	17.96								
Zn	11	12	13	14	15	16	17	18	19	20
1s	9915	9960	10010	10040	10120	10150	10230	10290	10350	10420
2s	1482	1528	1576	1613	1673	1716	1775	1828	1882	1936
2p	1353	1399	1448	1481	1546	1586	1650	1704	1760	1815
3s	393.9	429.9	467.1	501.5	541.6	578.0	618.7	658.3	698.0	737.4
3p	346.7	382.8	419.7	454.0	490.0	542.0	579.0	619.0		
3d	274.0	310.8								
Zn	21	22	23	24	25	26	27	28	29	30
1s	10480	10590	10800	10920	11130	11310	11490	11650	11870	12390
2s	1992	2087	2210	2309	2435	2550	2647	2780		
2p	1846	1953	2070	2216	2363	2479				

Chapter 6

THERMAL EQUILIBRIUM

6.1 Overview

This section describes the system of equations setting the local thermal balance of a cloud. The electron temperature is the only thermodynamic quantity used to characterize a photoionized cloud. The electron velocity distribution is predominantly Maxwellian ([Bohm and Aller, 1947](#)) although a trace constituent of non-thermal electrons may contribute when high-energy photons are present ([Spitzer and Tomasko, 1968](#)). A kinetic temperature can then characterize most of the electron velocity distribution. This in turn is defined by the balance between processes that add energy (heat) and remove energy (cool) the electrons.

Heating or cooling can be defined relative to either the ground state or continuum, and this difference has caused some confusion in the literature. CLOUDY defines heating and cooling relative to the continuum AGN3). Note that, in this scheme of bookkeeping, photoionization contributes an amount of heat given by $h(\nu - \nu_o)$, where $h\nu_o$ is the ionization potential of the atom or ion and ν is the photon energy. Emission of a recombination line *does not* constitute a cooling process. Heating and cooling rates are computed in cgs units (ergs, not Rydbergs) throughout CLOUDY.

6.2 Thermal stability

The criterion for thermal stability used by CLOUDY is that the net cooling (i.e., cooling minus heating) has a positive temperature derivative ([Field, 1965](#)). This can be expressed as

$$\frac{d(\Lambda - G)}{dT} > 0. \quad (6.1)$$

The code will print a “u” next to the temperature in the zone results, and make a comment at the end of the calculation, if possibly thermally unstable solutions were found. The criterion used by the code is that the derivative *at constant density* (isochoric) be positive. The more traditional criterion is that the derivative *at constant pressure* (isobaric) be positive ([Field, 1965](#)).

The fact that the code identifies a region as possibly thermally unstable does not necessarily show that it is. The derivatives used in equation 6.1 are those found during the search for the thermal solution. As such they are evaluated out of equilibrium as part of the temperature solver.

Their primary purpose was not to perform this thermal stability analysis. A section of Part III of this document goes into more detail about the stability check performed by the code, and how to do a better one.

6.3 Compton energy exchange

There are two parts to the Compton energy exchange problem. First, photons scatter off an electron at an angle θ , causing a change of photon energy due to Compton recoil given by

$$\frac{\Delta\epsilon_-}{\epsilon_o} = \left[1 - \frac{1}{1 + (\epsilon_o/m_e c^2)(1 - \cos\theta)} \right]. \quad (6.2)$$

For isotropic scattering the median scattering angle corresponds to $\cos\theta = 0.5$. Scattering by thermal electrons crates a shift with a distribution centered at

$$\frac{\Delta\epsilon_-}{\epsilon_o} = \frac{4kT}{m_e c^2} \quad (6.3)$$

and a standard deviation given by

$$\frac{\sigma}{\epsilon_o} = \sqrt{\frac{2kT}{m_e c^2}} \quad (6.4)$$

(see, e.g., [Zycki et al., 1994](#)).

The net volume-heating rate due to Compton energy exchange is given by

$$G_{Comp} - \Lambda_{Comp} = \frac{4\pi n_e}{m_e c^2} \left\{ \int \sigma_h J_\nu h\nu [1 + \eta_\nu] d\nu - 4kT \int \sigma_c J_\nu d\nu \right\} \quad [\text{erg s}^{-1} \text{cm}^{-3}] \quad (6.5)$$

See, for instance, ([Levich and Sunyaev, 1970](#)) and ([Krolik et al., 1981](#)). The two terms in braces are the heating and cooling terms respectively, while the factor in brackets in the first term accounts for heating due to both spontaneous and stimulated Compton scattering. Induced Compton heating is important when η_ν is large at frequencies where $h\nu \geq kT$. In fact it is, at most, a few percent effect in most circumstances.

The terms σ_h and σ_c appearing in equation 6.5 are the effective energy exchange (scattering) cross section for energy exchange, and differ from the Thomson cross section for energies $h\nu \sim m_e c^2$, where the Klein-Nishina cross section must be used. The numerical fits to the ([Winslow, 1975](#)) results, as used by ([Krolik et al., 1981](#)) and kindly provided by Dr. C.B. Tarter, are used. Defining

$$\alpha = \left\{ 1 + \nu_{Ryd} (1.1792 \times 10^{-4} + 7.084 \times 10^{-10} \nu_{Ryd}) \right\}^{-1} \quad (6.6)$$

and

$$\beta = \left\{ 1 - \alpha \nu_{Ryd} (1.1792 \times 10^{-4} + 2 \times 7.084 \times 10^{-10} \nu_{Ryd}) / 4 \right\}, \quad (6.7)$$

where ν_{Ryd} is the photon frequency in Rydbergs, the Compton energy-exchange rate coefficients are then $\sigma_h = \sigma_T \alpha$ and $\sigma_c = \sigma_T \alpha \beta$. Tests show that these are in excellent (much better than 1%) agreement with ([Guilbert, 1986](#))'s calculations for $h\nu < 10$ MeV, the energies where Guilbert's calculations are valid.

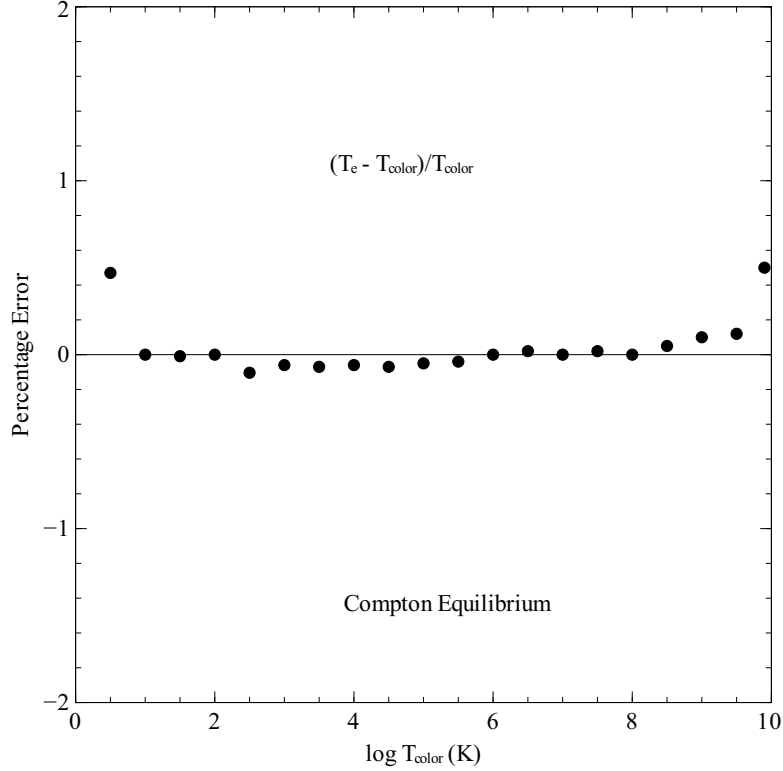


Figure 6.1: Thermal equilibrium in the Compton Limit. Calculations are for blackbody continua of various temperatures, given as T_{color} along the x-axis. The energy density temperature T_u is set equal to T_{color} . The density is adjusted to maintain ionization parameters $U \sim 10^{10}$, so that the thermal equilibrium equations are dominated by the Compton exchange problem. The deviation of the computed equilibrium temperature T_e from the asymptotic Compton temperature T_{color} is shown.

The coefficients for the heating and cooling terms, i.e., α and the product $\alpha\beta$, are calculated at the beginning of the calculation and stored in the vectors *csigh*(*v*) and *csigc*(*v*). The heating is determined by summing over the continuum;

$$G_{Comp} = \frac{n_e}{mc^2} \sigma_T (h\nu_{Ryd})^2 \sum \alpha_i \phi_i \nu_i^2 (1 + \eta_i) \quad (6.8)$$

where ϕ_i is the photon flux, η_i is the photon occupation number, σ_T is the Thomson cross section, and ν_i is the photon energy in Rydbergs .

Figure 6.3 shows results of a series of calculations in which Compton energy exchange was the dominant physical process affecting the temperature. These are a series of models in which the gas was irradiated by black body continua in strict thermodynamic equilibrium (i.e., $T_u = T_{color}$) and various hydrogen densities. Over the temperature range $3 \text{ K} \leq T_{color} \leq 10^{10} \text{ K}$ the computed equilibrium electron temperature equaled the color temperature within much better than 1% ($\langle T_e - T_{color} \rangle / T_{color} = -0.00073 \pm 0.0019$).

The intended temperature range of validity for CLOUDY is $2.8 \text{ K} - 1.001 \times 10^{10} \text{ K}$. Over the more limited range $10 \text{ K} - 10^9 \text{ K}$ the computed Compton temperature, for conditions in which strict TE is expected, is generally equal to the color temperature within three significant figures

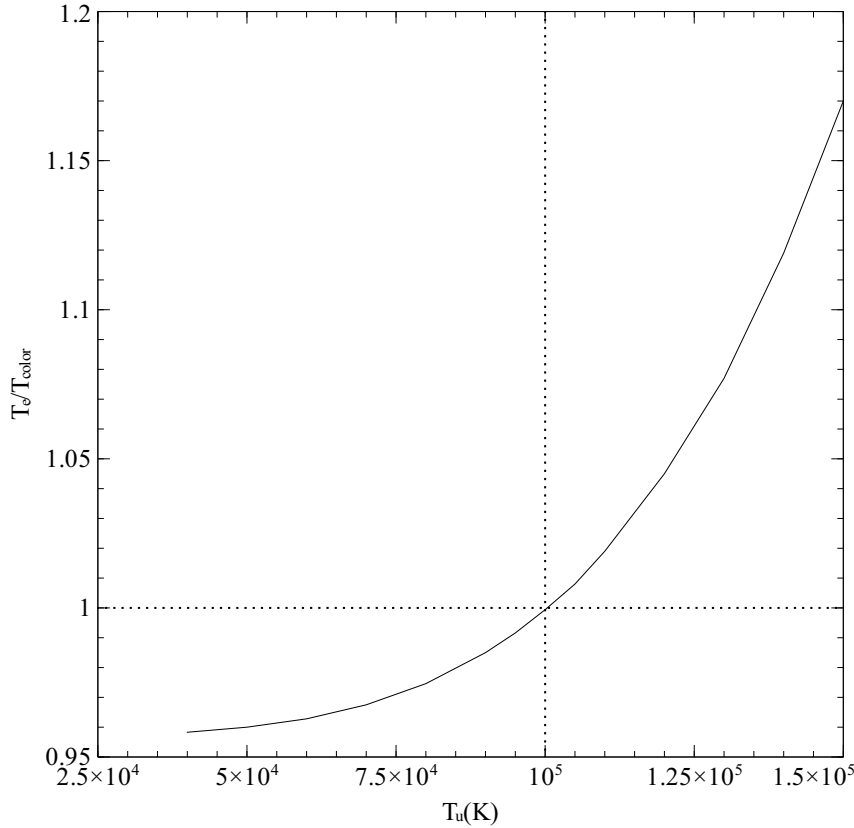


Figure 6.2: Calculations are for 10^5 K blackbodies and various values of the energy density temperature T_u , indicated along the x-axis. The ratio of the computed equilibrium temperature T_e to the color temperature T_{color} is shown. The two are equal when the energy density and color temperatures are equal. cmplte

(see Figure 6.3). At temperatures much greater than 10^9 K the electrons become relativistic; CLOUDY is not intended for these conditions. For temperatures much less than 10 K the computed temperature fails high because the energy bandwidth of the continuum array does not extend below 3.040×10^{-9} Ryd. As a further test, the models presented by (Krolik et al., 1981) were recomputed with excellent agreement (typically within 3%) with their computed Compton temperatures.

For a blackbody radiation field with $T_u \neq T_{color}$ the Compton temperature will not be equal to T_{color} because induced scattering will not contribute the required amount of heating-cooling. This case is shown in Figure 6.3, the results of a series of calculations in which the energy density temperature was varied (this is shown as the x-axis), but the color temperature held fixed at 10^5 K.

Note also that when $T_u > T_{color}$ induced Compton heating drives T_e above T_{color} . Only when the color and energy density temperatures are equal do the equilibrium and color temperatures match.

6.4 Bound Compton ionization, heating

Compton scattering can ionize atoms for photons of sufficiently high energy (≈ 2.3 keV for hydrogen). The energy given to an electron by a 90° scattering is found by rearranging equation 6.2 above

$$e = h\nu \left(1 - \frac{1}{1 + \frac{h\nu}{mc^2}} \right). \quad (6.9)$$

Setting this equal to the ionization potential of the species, $h\nu_o$, electrons will be removed by photons having an energy greater than

$$h\nu = \sqrt{h\nu_o mc^2}. \quad (6.10)$$

6.5 Expansion cooling

Adiabatic cooling ($\text{erg cm}^{-3} \text{ s}^{-1}$) due to the hydrodynamic expansion of the gas is given by

$$L_{\text{exp}} = -\frac{DU}{Dt} = -\frac{p}{\rho} \frac{D\rho}{Dt} + U \nabla \cdot \mathbf{v} = -\frac{5}{2} kT \frac{dn}{dt} = -\frac{5}{2} nkT \left[\frac{a}{u} + \frac{2u}{r} \right] \quad [\text{erg s}^{-1} \text{ cm}^{-3}] \quad (6.11)$$

where n, a, u , and r are the total particle density, acceleration, wind velocity, and radius respectively. This cooling term is only included when a wind geometry.

It should be noted that in this case, a quasi-static assumption is being made, so the results are only valid so long as all heating/cooling and ionization timescales are much shorter than the dynamical timescale.

Where this is not the case, the expansion cooling needs to be treated by an explicit time dependent approach, as detailed in the time dependent flow section.

6.6 Free-free heating-cooling

The volume free-free heating rate is given by

$$G_{ff} = 4\pi \int_{\nu_c}^{\infty} n_e \alpha_{\nu}(ff) J_{\nu} d\nu [\text{erg s}^{-1} \text{ cm}^{-3}] \quad (6.12)$$

where the free-free cross section is denoted by $\alpha_{\nu}(ff)$ and ν_c is the critical frequency defined below, and J_{ν} is the sum of the attenuated incident radiation field and the OTS line fields. Diffuse reemission, mainly free-free emission, *is not* included in this integral, as discussed below.

The code works with the difference between cooling and heating, since this is numerically more stable than considering each term as an independent heat source or coolant.

Cooling due to diffuse continua are treated by defining a critical frequency ν_c as follows. Gas at a depth r into the cloud is transparent to photons with energies above a critical frequency ν_c such that

$$\tau_c = \int_0^r \kappa(\nu_c) f(r) dr = \int_0^r \alpha_{\nu}(ff, \nu_c) n_e f(r) dr = 1 \quad (6.13)$$

and optically thick at lower frequencies. The critical frequency ν_c is evaluated for each zone.

The free-free cooling rate is then given by

$$\Lambda_{ff}(\tau) = \int_{\nu_c}^{\infty} n_e \alpha_{\nu}(ff) 4\pi B_{\nu}(T_e) d\nu = \Lambda_{ff}(0) \times \exp(-h\nu_c/kT) \quad (6.14)$$

where $\Lambda_{ff}(0)$ is the optically thin cooling rate and $B_{\nu}(T)$ is Planck's function. This is equivalent to assuming that, for $\nu < c$, where the cloud is optically thick, free-free heating and cooling exactly balance, as suggested by Kirchhoff's law and detailed balance considerations. Energies below ν_c are not included in free-free heating or cooling. This critical frequency is not allowed to be less than the plasma frequency for the current conditions.

6.7 Photoelectric heating, recombination cooling

The net heating rate due to photoelectric heating less spontaneous and induced recombination cooling of level n is given by

$$G = G_{n,\kappa} - \Lambda_{ind,n} - \Lambda_{spon,n} \quad [\text{erg s}^{-1}\text{cm}^{-3}] \quad (6.15)$$

where the volume heating rate due to photoionization is

$$G_{n,\kappa} = n_n \int_{\nu_o}^{\infty} \frac{4\pi J_{\nu}}{h\nu} \alpha_{\nu} h(\nu - \nu_o) d\nu \quad [\text{erg s}^{-1}\text{cm}^{-3}], \quad (6.16)$$

the volume cooling rate due to induced recombination is

$$L_{ind,n} = n_e n_p 4\pi P_n^* \int_{\nu_o}^{\infty} \frac{J_{\nu}}{h\nu} \alpha_{\nu} \exp(-h\nu/kT) h(\nu - \nu_o) d\nu \quad [\text{erg s}^{-1}\text{cm}^{-3}] \quad (6.17)$$

and the cooling rate due to spontaneous radiative recombination is

$$L_{spon,n} = n_e n_p kT \beta(T, n) \quad [\text{erg s}^{-1}\text{cm}^{-3}]. \quad (6.18)$$

The cooling rate coefficient $\beta(T, n)$ is evaluated as described elsewhere in this document.

6.8 Collisional ionization—three-body recombination

The net volume-heating rate due to collisional ionization less three-body recombination is given by

$$G_{n,\kappa} - L_{n,\kappa} = \sum_n P_n^* n_e n_p C_{n,\kappa} h\nu_o (1 - b_n) \quad [\text{erg s}^{-1}\text{cm}^{-3}] \quad (6.19)$$

where $C_{n,\kappa}$ is the collisional ionization rate, P_n^* are STE populations, and b_n is the departure coefficient. The term $(1 - b_n)$ is only large and positive for very low levels, in which $I_n > kT$. Far from thermodynamic equilibrium this is usually a net cooling process only for the ground term. This is because departure coefficients for excited states are nearly unity while the ground level usually has $b_n \cong 1$.

6.9 H^- heating and cooling

H^- bound-free

The volume-heating rate due to spontaneous absorption (photodissociation) is

$$G_{H^-} = n(H^-) \int_{\nu_o}^{\infty} \frac{4\pi J_\nu}{h\nu} \alpha_\nu h(\nu - \nu_o) d\nu \quad [\text{erg s}^{-1} \text{cm}^{-3}] \quad (6.20)$$

where symbols have their usual meaning. The volume-cooling rate due to induced radiative attachment is

$$L_{ind, H^-} = n_e n_{H^o} P^*(H^-) \int_{\nu_o}^{\infty} \alpha_\nu \frac{4\pi J_\nu}{h\nu} \exp(-h\nu/kT) h(\nu - \nu_o) d\nu \quad [\text{erg s}^{-1} \text{cm}^{-3}] \quad (6.21)$$

while the volume cooling rate for spontaneous radiative attachment is

$$L_{spon, H^-} = n_e n_{H^o} 8\pi P^*(H^-) \int_{\nu_o}^{\infty} \alpha_\nu \frac{\nu^2}{c^2} \exp(-h\nu/kT) h(\nu - \nu_o) d\nu \quad [\text{erg s}^{-1} \text{cm}^{-3}]. \quad (6.22)$$

6.9.1 H^- free-free

Free-free heating and cooling by H^- is also significant, although less so than bound-free heating. This is included, making the appropriate correction for stimulated emission, using the cross sections given by (Vernazza et al., 1981).

Under most circumstances H^- bound-free heating and cooling are much more important than H^- free-free processes. This is surprising at first sight, since standard opacity curves comparing bound-free and free-free opacities (Bates et al. 1975; Mihalas, 1978) show that the two are comparable. These curves are for strict thermodynamic equilibrium, with H^- departure coefficients of unity. Like the ground state of hydrogen, the departure coefficient for H^- is often many orders of magnitude larger than unity, so that the H^- bound-free opacity and the resulting heating greatly exceed the H^- free-free opacity.

6.10 Line heating and cooling

6.10.1 Overview

All lines will be treated as data types *EmLine*. The following sections describe the major routines for computing heating and cooling for n -level atoms. Emission lines are often optically thick. All lines are transferred using escape probabilities, by determining level populations including both collisional and radiative processes (see, for example, Elitzur, 1992). Line masing can sometimes occur, and again is treated using escape probabilities.

In all cases the net cooling due to a transition is given as

$$L_{line} = h\nu_{u,l} (n_l C_{l,u} - n_u C_{u,l}) \quad [\text{erg cm}^{-3} \text{s}^{-1}] \quad (6.23)$$

where the populations of levels are given by n_i and C_{ij} is the collision rate. This cooling is evaluated in a series of routines which are responsible for evaluating the line intensity, cooling,

and destruction rate, and entering these into the appropriate stacks. Each routine sets the following attributes.

Lines can act to *heat* rather than cool the gas when the gas is irradiated by a continuum with a brightness temperature greater than the gas temperature at the line energy. This is an important gas heating mechanism for PDRs, for instance (Tielens and Hollenbach, 1985). If η is the photon occupation number of the attenuated incident continuum at the line frequency, then the rate atoms are excited from the ground level is given by $\eta \epsilon A_{ul}$ where ϵ is the line escape probability. A fraction $C_{ul}/(C_{ul} + \epsilon A_{ul})$ of these radiative excitations is converted into heat by collisional de-excitation. The net heating due to this process is then

$$G_{FIR} = n_l \eta_v \epsilon_{lu} A_{ul} \left(\frac{C_{ul}}{C_{ul} + \epsilon_{lu} A_{ul}} \right) h\nu \quad [\text{erg cm}^{-3} \text{s}^{-1}] \quad (6.24)$$

where n_l is the density of the ground level. This process is included for all transferred lines.

6.10.2 Two level atoms

Cooling due to collisional excitation of two level atoms of the heavy elements is evaluated in routine *level2*. This routine does the following: a) finds the abundance of the two levels by balancing collisional and radiative processes, subject to the sum $n_l + n_u = \text{abundance}$. b) adds the line cooling (or heating) to the total cooling, c) adds the line derivative to dC/dT , d) evaluates the fraction of the escaping line destroyed by background opacity, e) adds this to the local OTS radiation field, f) records the line opacity population $n_l - n_u g_l/g_u$. The populations of the atom are saved in the vector *PopLevls*.

6.10.3 Three level atoms

The level populations, cooling, and line destruction by background opacity sources are computed for three level atoms in routine *level3*.

Routine *level3* is called with three arguments, the three line structures. Levels are designated by the indices 0, 1, and 2, with 0 being the lowest level. The routine is called with three line structures, indicated by $t10$, $t21$, and $t20$, each representing the downward radiative transition between the indicated levels. Any one of these transitions may be a dummy transition, using the dummy line *TauDmmy* provided for this purpose. The total rates between any two levels $i \rightarrow j$ is indicated by R_{ij} . This includes collisions, radiative decays (both photon escape and destruction by background opacity), and induced transitions. If the total abundance of the parent ion is A , the three balance equations are

$$n_0 + n_1 + n_2 = A \quad (6.25)$$

$$n_0 (R_{01} + R_{02}) = n_1 R_{10} + n_2 R_{20} \quad (6.26)$$

$$n_1 (R_{10} + R_{12}) = n_2 R_{21} + n_0 R_{01}. \quad (6.27)$$

Setting n_0 to $A - n_1 - n_2$ the above becomes

$$(R_{01} + R_{02}) (A - n_1 - n_2) = n_1 R_{10} + n_2 R_{20}. \quad (6.28)$$

After gathering terms this equation becomes

$$A(R_{01} + R_{02}) = n_1(R_{10} + R_{01} + R_{02}) + n_2(R_{20} + R_{01} + R_{02}). \quad (6.29)$$

Substituting for n_0 we find

$$n_1(R_{10} + R_{12}) = n_2 R_{21} + R_{01}(A - n_1 - n_2). \quad (6.30)$$

Gathering terms this equation becomes

$$n_1(R_{10} + R_{12} + R_{01}) = AR_{01} + n_2(R_{21} - R_{01}). \quad (6.31)$$

Solving we obtain

$$n_1 = \frac{A(R_{01} + R_{02})}{R_{10} + R_{01} + R_{02}} - \frac{n_2(R_{20} + R_{01} + R_{02})}{R_{10} + R_{01} + R_{02}} \quad (6.32)$$

and we find

$$n_1 = \frac{AR_{01}}{R_{10} + R_{12} + R_{01}} + \frac{n_2(R_{21} - R_{01})}{R_{10} + R_{12} + R_{01}} \quad (6.33)$$

Equating the two and gathering terms we obtain

$$n_2 \left(\frac{R_{21} - R_{01}}{R_{10} + R_{12} + R_{01}} + \frac{R_{20} + R_{01} + R_{02}}{R_{10} + R_{01} + R_{02}} \right) = \frac{A(R_{01} + R_{02})}{R_{10} + R_{01} + R_{02}} - \frac{AR_{01}}{R_{10} + R_{12} + R_{01}} \quad (6.34)$$

with the solution

$$n_2 = A \left(\frac{(R_{01} + R_{02})}{R_{10} + R_{01} + R_{02}} - \frac{R_{01}}{R_{10} + R_{12} + R_{01}} \right) / \left(\frac{R_{21} - R_{01}}{R_{10} + R_{12} + R_{01}} + \frac{R_{20} + R_{01} + R_{02}}{R_{10} + R_{01} + R_{02}} \right). \quad (6.35)$$

In the code the term in the numerator in the previous equation is called *alpha*, and the denominator *beta*. Replacing n_2 in the above we obtain

$$n_1 = [A(R_{01} + R_{02}) - n_2(R_{20} + R_{01} + R_{02})] / (R_{10} + R_{01} + R_{02}). \quad (6.36)$$

Again the two terms are called *alpha* and *beta*.

6.10.4 Li Sequence

Table 6.1 gives the stronger lines of Li-sequence ions. **Level3** is used for this sequence.

6.10.5 Boron Sequence

Figure 6.10.5 shows levels within the lowest three configurations of the Boron sequence.

Table 6.1: Lithium Sequence Lines

N	Ion	$j = 3/2 - 1/2$	$j = 1/2 - 1/2$	$j = 3/2 - 1/2$	$j = 1/2 - 1/2$
6	C IV	1548.195	1550.770	312.422	312.453
7	N V	1238.821	1242.804	209.2702	09.303
8	O VI	1031.9261	1037.6167	150.088	150.124
10	Ne VIII	770.409	780.324	88.134	
12	Mg X	609.79	624.95	57.88	57.92
13	Al XI	550.03	568.15	48.30	48.34
14	Si XII	499.40	520.67	40.92	
16	S XIV	417.61	445.77	30.43	
18	Ar XVI	353.92	389.14	25.53	
20	Ca XVIII	302.215	344.772	18.69	18.73
26	Fe XXIV	192.017	255.090	10.62	10.66

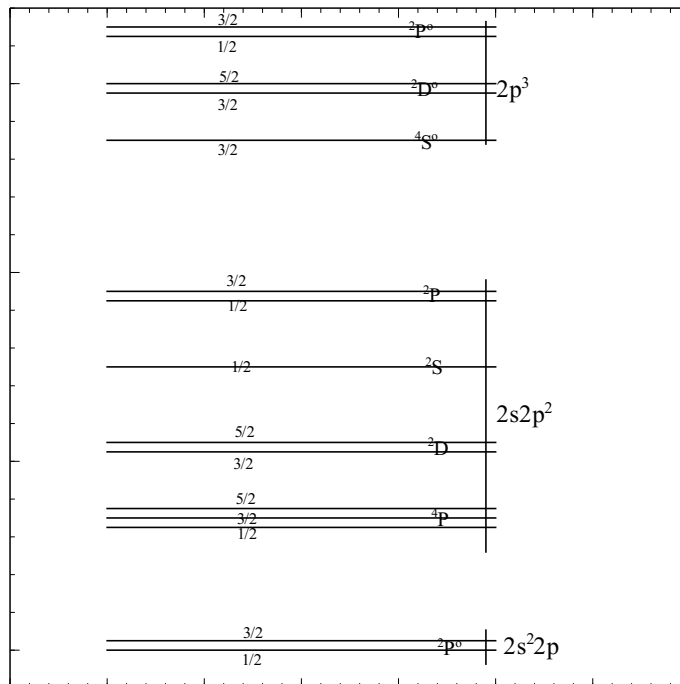


Figure 6.3: Energy Level Diagram for Boron Sequence.

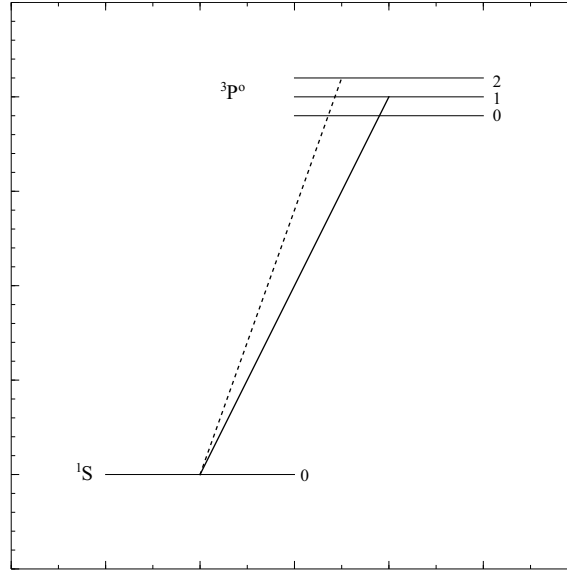


Figure 6.4: Energy Level Diagram for Beryllium Sequence.

6.10.6 Beryllium sequence atoms

Figure 6.10.6 shows the model of the Beryllium sequence. The level populations, cooling, and line destruction by background opacity sources are computed for a specialized four level atom in routine *AtomSeqBeryllium*.

Routine *beseq* is called with five arguments, the collision strengths between the excited triplet levels, the line optical depth array for the fast ($j = 1$ to $j = 0$) transition, and the transition probability for the slow ($j = 2$ to $j = 0$) transition. Induced processes are only included for the fast transition. The collision strength stored in the line array is the collision strength for the entire multiplet. Rates to levels within the term are assumed to scale as the ratio of level statistical weight to term statistical weight. The level populations for the ground and excited states, with no correction for stimulated emission, are returned in the array *PopLevls*, contained in the common block of the same name.

The total rates between any two levels $i\Lambda j$ is indicated by R_{ij} . This includes collisions, radiative decays (for the fast transition, both photon escape and destruction by background opacity, and induced transitions). If the total abundance of the parent ion is A , the three balance equations are

$$n_0 + n_1 + n_2 + n_3 = A \quad (6.37)$$

$$n_0 (R_{01} + R_{02} + R_{03}) = n_1 R_{10} + n_2 R_{20} + n_3 R_{30} \quad (6.38)$$

$$n_1 (R_{10} + R_{12} + R_{13}) = n_3 R_{31} + n_2 R_{21} + n_0 R_{01}. \quad (6.39)$$

$$n_2 (R_{20} + R_{21} + R_{23}) = n_3 R_{32} + n_1 R_{12} + n_0 R_{02}. \quad (6.40)$$

Collisions are included in all these terms. R_{32} includes the slow downward line escape, while R_{02} and R_{20} includes escape, destruction by background opacity, and fluorescent excitation—deexcitation. In the code the terms on the LHS of equations 39, 40, and 38 are called α , β , and γ .

6.11 Evaluation of the cooling function

6.11.1 Total cooling

The cooling function is evaluated in routine *coolr*. This in turn calls other routines which compute cooling for individual elements. Each individual coolant is entered as a separate quantity in the array *cooling*. Under some extreme circumstances agents that are normally coolants can actually heat the gas. Negative coolants are stored in a parallel array, *heatnt*.

The total cooling is the sum of this array, referred to as the variable *ctot*, and evaluated in routine *SumCool*.

6.11.2 The cooling derivative

As the cooling is evaluated, its approximate temperature derivative is computed by making analytic expansions of the cooling for individual agents. For instance, collisionally excited lines of positive ions have collisional excitation rates that depend on the product

$$L_{line} \propto n_e n_{ion} T_e^{-1/2} \exp(-T_{exc}/T_e) \quad (6.41)$$

where T_{exc} is the excitation temperature of the line. In this case the derivative of the cooling function can be expressed as

$$\frac{dL_{line}}{dT} \propto n_e n_{ion} \frac{d}{dT} T_e^{-1/2} \exp(-T_{exc}/T_e) = L_{line} \left[\frac{T_{exc}}{T_e^2} - \frac{1}{2T_e} \right] \quad (6.42)$$

This derivative is used by the thermal predictor-corrector routine to make the initial guess at a new temperature. This is approximate since both electron and ionic densities also depend on the temperature.

6.12 Evaluation of the heating function

Various contributions to the heating function are evaluated throughout the code. Each heating agent stores its contribution to the total heating within a cell of the two dimensional array *heating*. The total heating is always the sum of the total contents of the *heating* array.

6.13 Equilibrium calculations

This is largely taken after [Ferland and Rees \(1988\)](#).

6.13.1 Hydrogen only

Figure 6.13.1 shows the results of a series of calculations in which the full set of statistical and thermal equilibrium equations are solved for thin cells of pure hydrogen gas with various densities.

The ionizing continuum is, in all cases, a black body with $T_{color} = 5 \times 10^4$ K, and the energy density of the radiation field is varied, up to the thermodynamic equilibrium limit, $T_u = T_{color}$.

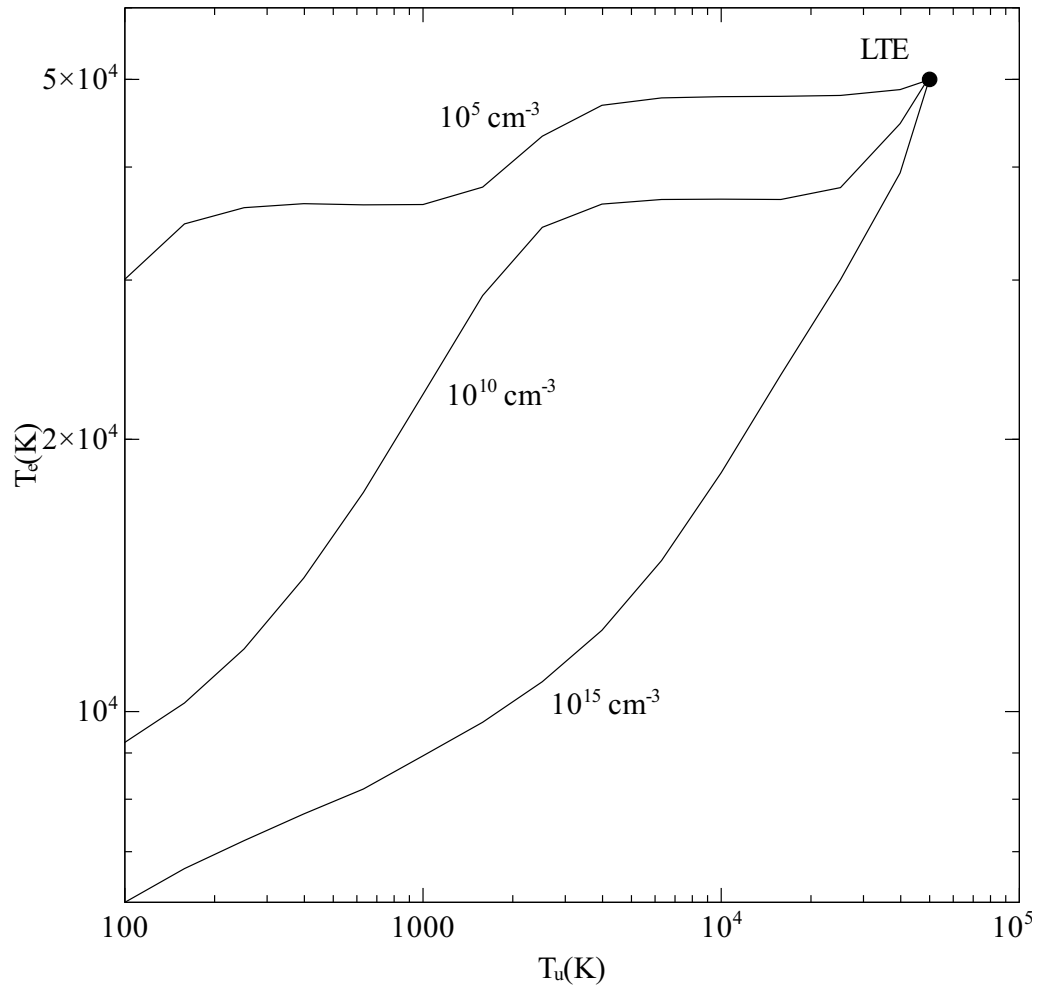


Figure 6.5: Thermal equilibrium calculations for an optically thin gas with 3 hydrogen densities are shown as a function of the radiation field energy density, parameterized as T_u . Ionization is by a 5×10^4 K black body. Various processes drive the gas to thermodynamic equilibrium when T_u reaches 5×10^4 K.

Although the gas temperature in the thermodynamic equilibrium limit does not depend on the gas density, the physical processes that drive the gas to this temperature do. Thermal equilibrium calculations were performed with three densities chosen to span a fairly wide range. For low densities ($n(H) = 10^5 \text{ cm}^{-3}$) the gas remains highly ionized for all values of T_u shown. The temperature in thermodynamic equilibrium is set by the balance between Compton and inverse-Compton scattering. The intermediate density case ($n(H) = 10^{10} \text{ cm}^{-3}$) reaches thermodynamic equilibrium with $\sim 3/4$ of the heating-cooling set by Compton scattering and the remainder due to free-free and free-bound processes. The high-density ($n(H) = 10^{15} \text{ cm}^{-3}$) case reaches its thermodynamic equilibrium temperature with a balance between free-free (1/3 of the total) and free-bound (2/3 of the total) processes. In all cases the level populations and electron temperature are within $\sim 1\%$ of their expected thermodynamic equilibrium values when $T_u = T_{color}$.

6.13.2 Helium-only gas

To do

6.13.3 Metal rich gas

Simulations of very metal rich gas has been a major emphasis of the code as described by (Hamann and Ferland, 1993) and (Ferland et al., 1996). In these cases the thermal and ionization balance is totally dominated by the heavy elements.

Figure 6.13.3 shows the results of a series of calculations in which gas with strongly enhanced abundances of the heavy elements is exposed to a series of black body radiation fields with different temperatures and energy densities. (Ferland and Rees, 1988) and (Ferland and Persson, 1989) gave analogous calculations for pure hydrogen clouds. The filled circles represent the cases where the energy densities of the radiation field are equal to the color temperature, and strict thermodynamic equilibrium is expected. This is indeed the case. The distribution of ionization for each color temperature is radically different, but the line interactions with the radiation field bring the gas to the expected equilibrium temperature. This tests both the ionization and thermal balance in this extreme environment.

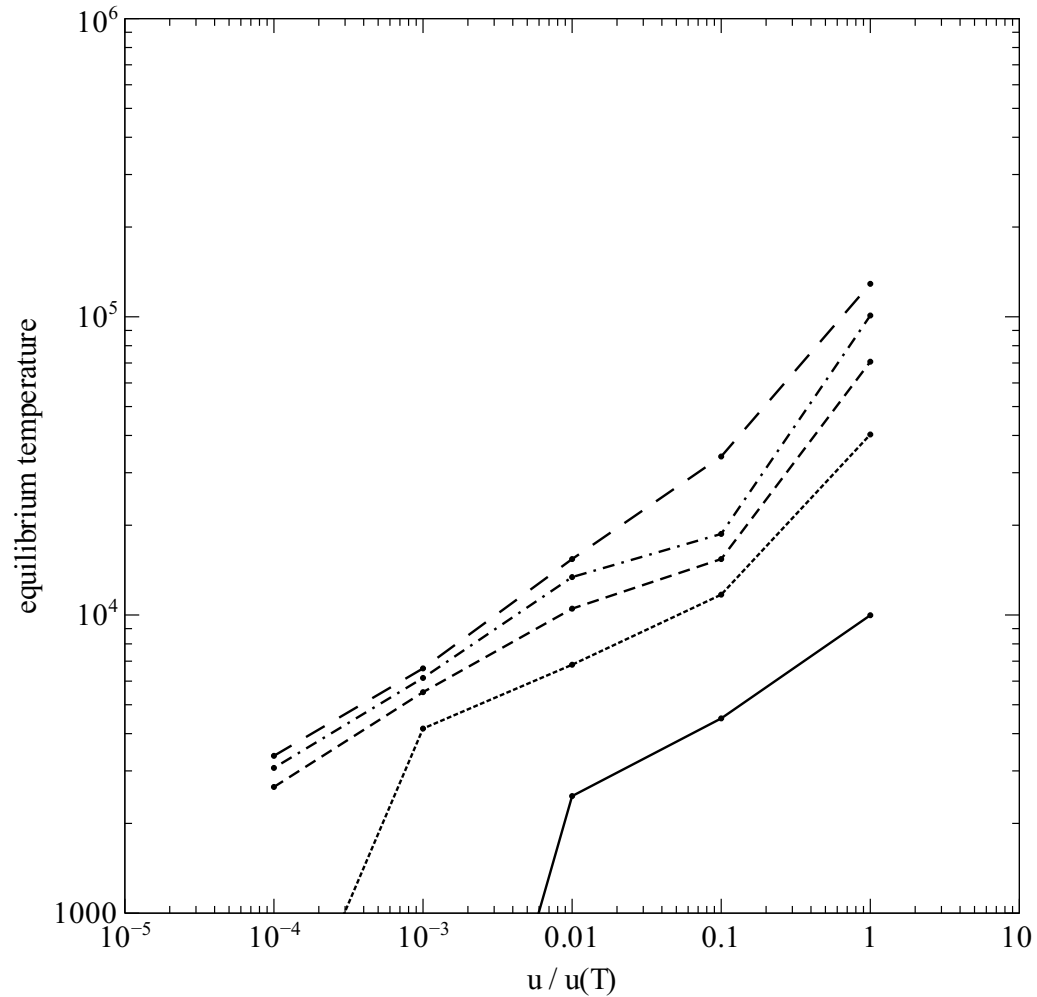


Figure 6.6: Equilibrium temperature of gas exposed to five black bodies with various energy density temperatures. The color temperatures of the blackbodies are 10000 K, 40000 K, 70000 K, 100000 K and 130000 K. The metallicity was 10 times solar (Hamann and Ferland 1993) so that heating cooling of thousands of heavy element emission lines dominates the thermal equilibrium. The simulation is of an optically thin cell of gas with density 10^{10} cm^{-3} (results do not depend on this density). The x-axis is the local energy density relative to the energy density in thermodynamic equilibrium at that temperature. The gas goes to thermodynamic equilibrium when the radiation field does (the color and energy density temperatures are equal).

Chapter 7

GRAIN PHYSICS

7.1 Overview

The following discussion outlines some physical processes relating to grains, as incorporated in CLOUDY. It is adopted from [Baldwin et al. \(1991\)](#), and was written in close collaboration with P.G. Martin.

Much of this physics has been updated to that described by [van Hoof et al. \(2004\)](#), which is based on ([Weingartner and Draine, 2001](#)).

Several grain populations, types of graphite and “astronomical silicates”, are available. Usually one of each type, for a total of two, is selected, although there is no limit to the number of grain populations. Optical properties like opacity of the species are based on a realistic power-law size distribution. Other properties (like potential and temperature) are computed for a mean grain size rather than calculated for each individual size.

The following describes the “old”, default, grains that were originally incorporated into the code in the late 1980’s ([Baldwin et al., 1991](#)). These use optical properties that correspond to averages over the grain size distribution. The current treatment both resolves the grain size distribution and includes single photon heating for the smaller grains. This new treatment is described in [van Hoof et al. \(2001\)](#) and will be included in this document at a later time.

7.2 Grain opacity

Grains are not included in the calculation by default. When enabled with the grain command the default mixture has interstellar medium (ISM) properties. Grains more similar to those seen in Orion or planetary nebulae are also available.

7.2.1 ISM grains

The optical constants for the default (ISM) grain species are from the calculations of ([Martin and Whittet, 1990](#)). These extend the work of ([Draine and Lee, 1984](#)) to ionizing energies where the grains are strongly absorbing. These opacity calculations were based on the ([Mathis et al., 1977](#)) power-law size distribution to simulate interstellar extinction in diffuse clouds.

7.2.2 Orion grains

Grains within the Orion Nebula have a relatively large ratio of total to selective extinction R and an exceptionally gray opacity in the ultraviolet. These are both indicative of a deficiency in small grains and a larger mean grain size. To account for this, a second set of opacity functions is included, the Orion group. For this the value of the smallest size (a_{-}) in the (Mathis et al., 1977) size distribution was increased from $0.0025\mu\text{m}$ to $0.03\mu\text{m}$. While this simple adjustment of the size distribution is not entirely adequate for explaining the details of the visible and near ultraviolet Orion extinction curve (Mathis and Wallenhorst, 1981), it should be an improvement for the ionizing ultraviolet portion, which is most important.

The Orion extinction curve is designed to simulate the large R grains observed in this H II region. Relative to ISM standard grains the total amount of grain material was preserved, so that α_{abs} in the infrared and in the EUV and X-Ray regions remains unchanged. The main differential effect is to lower the cross section through a broad peak at 1 Ryd.

7.2.3 PN grains

Infrared opacities for the silicate component are taken from unpublished work by K. Volk. Ultraviolet silicate cross sections, and the graphite constituent, are standard ISM.

7.2.4 Extinction

The ISM extinction properties, both effective scattering (subscript scat) and absorption (subscript abs), are shown in Figure 7.2.4.

The quantities plotted are cross sections (cm^2) per H nucleon: $\sigma = \kappa/n(H)$, where κ (cm^{-1}) is the opacity due to grains and $n(H)$ (cm^{-3}) is the local density of H in any form. Rather than the total scattering cross section σ_s an effective scattering cross section $\sigma_{\text{scat}} = \sigma_s(1 - g)$ is plotted. This discounts the radiation scattered near the forward direction. The asymmetry parameter g approaches unity at high and low energies, particularly for larger grains, so that σ_{scat} becomes much less than α_{abs} .

The optical depth τ is σ times the hydrogen column density (or κ integrated over the path). Absorption attenuates the incident radiation field as $\exp(-\tau_{\text{abs}})$. The effects of scattering are more difficult to model. In an open geometry, scattering attenuates approximately as $(1 + 0.5\tau_{\text{scat}})^{-1}$. However, in a closed geometry, to within factors of order unity, the scattered light is not lost from the beam, and the scattering opacity can be ignored. In either case, effective grain scattering optical depth is generally fairly small through the ionized nebula at ionizing energies.

7.3 Photoelectric emission

As discussed below, photoelectric emission from grains contributes directly to heating the gas and, through the grain potential U_g established, affects radiative and collisional heating of the grains and the grain drift velocity.

The photoionization rate of a grain, per unit projected area, is

$$\Gamma_g = \int_{\nu_o}^{\infty} Q_{\text{abs}} \frac{4\pi J}{h\nu} \hat{Y} d\nu \quad (7.1)$$

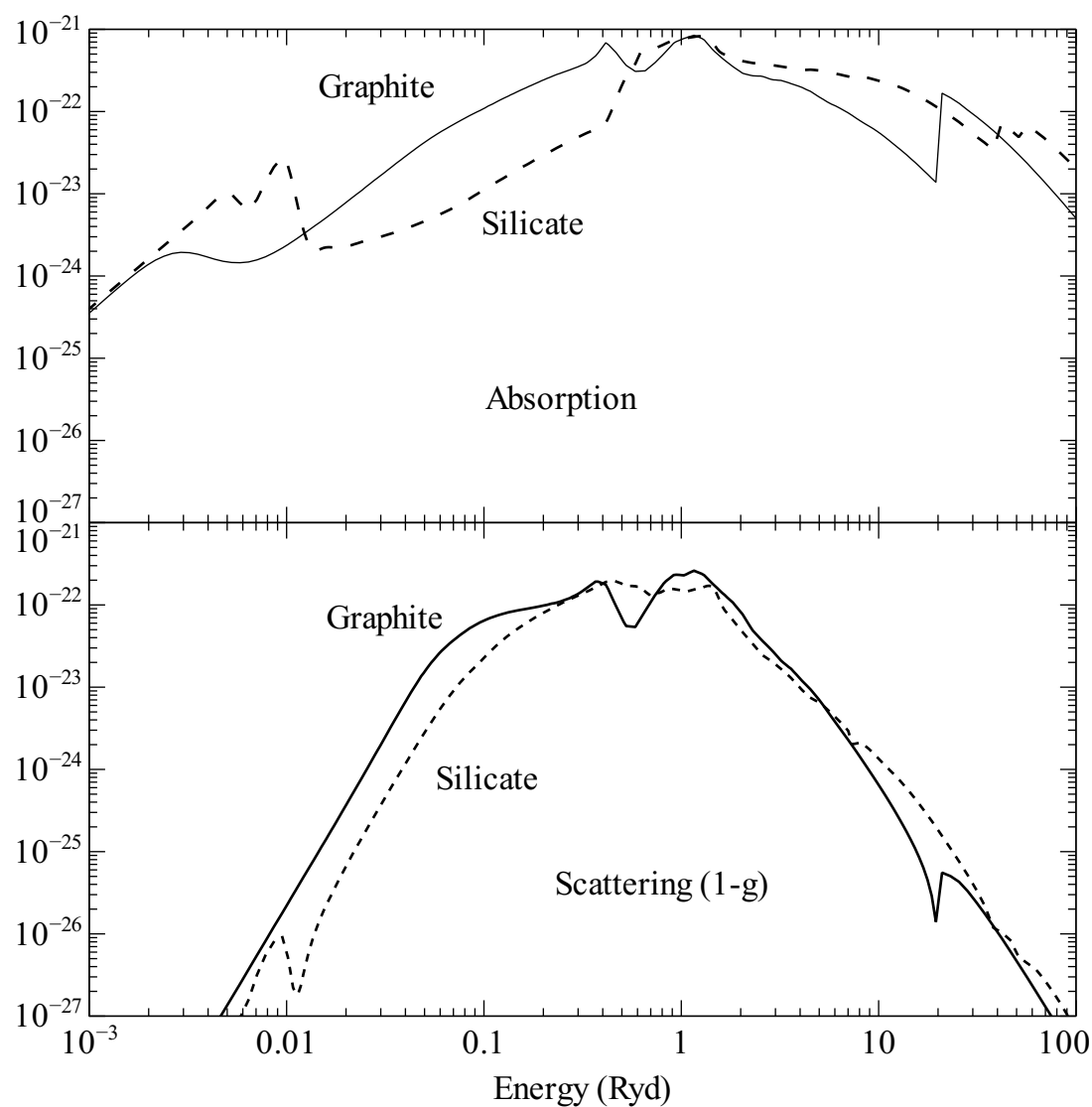


Figure 7.1: The absorption and scattering cross sections (cm^2 per hydrogen nucleon) for the two ISM grain populations, graphite and silicate, are shown. The effective scattering cross section is the scattering cross section multiplied by $1 - g$, where g is the asymmetry parameter.

where \hat{Y} is the effective photoelectric yield per absorbed photon, Q_{abs} is the absorption efficiency factor, and $4\pi J/h\nu$ symbolizes the photon flux of direct, diffuse, and OTS radiation fields. For the OTS line component, the integral is of course just a sum over the line photons that are sufficiently energetic. The threshold for photoemission, to be determined self-consistently, is given by $h\nu_o = \max\{V_n + V_g, V_n\}$, where V_n is the photoelectric threshold for a neutral grain and $V_g = eU_g$.

V_g will depend on grain size through Q_{abs} and \hat{Y} . In the present implementation, a typical V_g is defined for each species by using Q_{abs} averaged over the size distribution:

$Q_{abs} = \alpha_{abs}/\Sigma = \kappa_{abs}/n(H)\Sigma$. The projected grain area per H, Σ , is similar for each species: $2.1 \times 10^{-22} \text{ cm}^2$ for graphite and $2.4 \times 10^{-22} \text{ cm}^2$ for silicates.

\hat{Y} is constructed as follows. The basic laboratory data measure the yield (per absorbed photon) for a neutral surface, Y_n . For each incident photon energy $h\nu$, the photoelectrons emerging from the neutral surface have varying energies E , with a probability distribution $p_n(E)$. To account for electron escape from finite sized grains, yields measured for semi-infinite sheets in the laboratory have to be corrected by a factor $f(E)$ (which introduces a size dependence). Such a correction would change the shape of the probability distribution as well as increase the integrated emission from a neutral surface (Draine, 1978 gives an approximate expression for the overall increase). Then, formally

$$\hat{Y} = Y_n \int_{E_o}^{(h\nu - V_n)} f p_n dE \quad (7.2)$$

where $E_o = \max\{0, V_g\}$ introduces the fact that the lowest energy photoelectrons do not escape from positively charged grains.

The form adopted is

$$Y_n = \min\{Y_o(1 - V_n/h\nu), Y_1\} \quad (7.3)$$

for $h\nu \geq V_n$, and $V_n = 8 \text{ eV}$ and $Y_o = 0.5$ is assumed for both grain populations; according to Draine (1978) this combination gives about the right amount of photoelectric emission to heat neutral H I clouds in interstellar space ($h\nu \leq 13.6 \text{ eV}$). For the higher energies a cap at $Y_1 = 0.2$ is introduced, which is suggested by experimental data. For p_n a simple form that is independent of E (Draine, 1978) is adopted:

$$p_n = (h\nu - V_n)^{-1} \quad (7.4)$$

While only approximate, this induces the physically correct response (decrease) in \hat{Y} (and the photoelectric heating) when the grain is positively charged. Because the form of $f(E)$ is highly uncertain $f = 1$ is assumed (this again avoids a size dependency). Extension of the flat cap in Y_n to high energies also addresses this issue to some degree. With these assumptions, \hat{Y} is known in analytic form:

$$\hat{Y} = Y_n \min\{1, 1 - V_g/(h\nu - V_n)\} \quad (7.5)$$

7.4 Collisional charging of a grain

Per unit projected area of a grain, collisions with particles of space density n , mass m , and charge Z ($Z = -1$ for electrons) give an effective recombination rate

$$\alpha(gr) = -n \bar{v} S Z \eta \quad (7.6)$$

where

$$\bar{v} = \sqrt{8kT/\pi m_e} \quad (7.7)$$

is the mean particle speed. In this expression, and for other collisional rates involving n below, it is implicit that there is a sum of similar terms over all species in the gas. For electrons S is the sticking probability which we take to be 1 (Spitzer, 1948; Watson, 1972; Draine, 1978). For positively charged nuclei, SZ is the charge transfer efficiency, taken to be Z here. The last factor v , the correction for Coulomb interactions between the grain and the recombining particles of charge Z , is given in terms of

$$\psi = ZV_g/kT_e \quad (7.8)$$

by

$$\eta = \begin{cases} 1 - \psi & \text{if } \psi \leq 0 \\ \exp(-\psi) & \text{if } \psi > 0 \end{cases} \quad (7.9)$$

Terms for positively charged nuclei are included, but are usually small relative to the contribution from free electrons.

7.5 Grain potential

The steady state grain potential is determined for each grain species independently by requiring charge balance. Expressed as a balance per unit area this is $\alpha_{gr} = \Gamma_{gr}$. Because of the many dependencies on V_g , this is carried out numerically.

7.6 Grain drift velocity

The grain drift velocity is determined by balancing the radiative acceleration due to the direct attenuated radiation field with the drag forces given by equations 1–6 of Draine and Salpeter (1979). The equations are solved numerically for the drift velocity, including interactions with electrons and all ions present in the gas.

7.7 Radiative heating and cooling of a grain

Once the grain potential is known, the rate of radiative heating of the grain per unit projected area is

$$G_{grain}(rad) = \int_0^{V_o} Q_{abs} 4\pi J d\nu + \int_{V_o}^{\infty} Q_{abs} \frac{4\pi J}{h\nu} (h\nu - EY) d\nu. \quad (7.10)$$

The last term represents the portion of the photon energy that does not heat the grain, but rather passes to the escaping electrons:

$$EY = Y_n \int_{E_o}^{(h\nu - V_n)} E f p_n dE. \quad (7.11)$$

With the above approximations for f and p_n this is given analytically by

$$EY = 0.5 Y_n \left[(h\nu - V_n)^2 - [\max(0, V_g)]^2 \right] / (h\nu - V_n) \quad (7.12)$$

The cooling of a grain by radiative losses, per unit projected area, is given by

$$\Lambda_{\text{grain}}(\text{rad}) = \int_0^\infty Q_{\text{abs}} 4\pi B_\nu(T_g) d\nu \quad (7.13)$$

where $B_\nu(T_g)$ is the Planck function for the grain temperature.

7.8 Collisional heating of a grain

Collisions with electrons, ions, and neutral particles also heat the grains. Per unit projected area of the grain, this heating rate may be written as

$$G_{\text{grain}}(\text{col}) = n \bar{v} S (2kT_e \xi - ZV_g \eta + I \eta - 2kT_g \eta). \quad (7.14)$$

The first term corresponds to kinetic energy extracted from the gas. The factor makes adjustment for Coulomb interactions and is given by

$$\xi = \begin{cases} 1 - \psi/2 & \text{if } \psi \leq 0 \\ (1 + \psi/2) \exp(-\psi) & \text{if } \psi > 0 \end{cases} \quad (7.15)$$

The second term in $G_{\text{grain}}(\text{col})$ allows for the change of the particle's energy in the grain potential. In the third term, the product $I\eta$ is the average chemical energy released per impact. Here it is assumed that when impinging ions recombine the ionization energy released is deposited as heat in the grain (there is then no corresponding term for heating the gas in Λ_g below). The last term describes the effect of thermal evaporation of neutralized ions and thermally accommodated neutral particles (there is no corresponding term for electrons).

In implementing the above processes, S for electrons is again the sticking probability. For positively charged nuclei, S is the energy transfer efficiency, taken here to be unity (this process should be evaluated consistently with that for charge transfer). For neutral particles of mass m striking a grain whose typical atom has mass M , the accommodation coefficient $S \approx 2mM/(m+M)^2$ (Draine, 1978).

7.9 Grain temperature

The equilibrium grain temperature is determined by the balance between cooling (Λ) and heating (G) by radiative and collisional processes. For the radiative terms, Q_{abs} averaged over the size distribution is used to obtain a typical temperature for each species.

As a test of the bandwidth of the code, and its behavior in a well-defined limit, tests were computed in which the grains were irradiated by black body radiation in strict thermodynamic equilibrium (i.e., the color and energy density temperatures were equal). Radiation temperatures between 10 K and 10^9 K, the temperature limits to the code, were used. These tests showed that the deduced grain equilibrium temperature was within much better than 1 percent of the blackbody temperature.

7.10 Photoelectric heating of the gas

Heating of the gas by photoemission from grains can be an important process in ionized regions (Spitzer, 1948; Oliveira and Maciel, 1986). For charged grains this heating rate ($\text{erg cm}^{-3} \text{ s}^{-1}$) is given by

$$G_{\text{gas}} = \int_{\nu_0}^{\infty} \kappa_{\text{abs}} \frac{4\pi J}{h\nu} (EY - V_g \hat{Y}) d\nu. \quad (7.16)$$

The first term describes the energy of the photoelectrons as they leave the surface, balancing the similar term in $G_{\text{grain}}(\text{rad})$. The second term compensates for the grain potential, and can be seen to balance the related term in $G_g(\text{col})$ when charge balance holds.

7.11 Collisional cooling of the gas

The gas is cooled as the gas particles hit the cooler grain surface. Per unit volume, this cooling rate may be written as

$$\Lambda_{\text{gas}} = n n(H) \Sigma \bar{v} S (2kT_e \xi - 2kT_{\text{grain}} \eta), \quad (7.17)$$

the individual terms consistently balancing the corresponding ones in $G_g(\text{col})$.

7.12 Grain sublimation

The code checks that grain survival is likely by comparing the highest grain temperature with the sublimation temperatures. These are taken to be 1400 K for silicates and 1750 K for graphite and are based on the paper by Laor and Draine (1993). A warning will be printed at the end of the calculation if the grain temperature rises above the sublimation point. A caution will be printed if the temperature rises above 90% of the sublimation point.

7.13 Ionic recombination on grain surfaces

Positive ion recombination on grain surfaces proceeds at a rate $n_{\text{ion}} n_H \alpha_{gr}$ where the recombination coefficient is taken from Draine and Sutin (1987); their equation 5.15). For a standard grain size distribution this rate coefficient is $\sim 5.8 \times 10^{-13} T_e^{-0.5} \text{ cm}^3 \text{ s}^{-1}$. This process is included for all ions included in the calculation when grains are present, but is not generally important.

Chapter 8

OTHER PHYSICAL PROCESSES

8.1 Overview

This section describes other physics processes that have been incorporated into CLOUDY. Some of these are taken from published papers that have described the formalism used by CLOUDY in detail. The original papers are cited in the beginning of each section.

8.2 Magnetic fields

Magnetic fields are not normally considered by the code, but can be included with the **magnetic field** command.

Cooling due to electron cyclotron emission, using equations from [Fabian et al. \(1976\)](#); these assume optically thin emission) are included when the field is specified. The volume-cooling rate is given by

$$\Lambda_{cyclotron} = n_e \frac{B^2}{8\pi} \frac{4}{3} \sigma_{Thom} c \left(\frac{v_e}{c} \right)^2 = 4.5433 \times 10^{-25} n_e B^2 T_e \quad [\text{erg cm}^{-3} \text{s}^{-1}] \quad (8.1)$$

where σ_T is the Thomson cross-section and

$$u_e = \left(\frac{8kT_e}{\pi m_e} \right)^{1/2} = 6.2124 \times 10^5 T_e^{1/2} \quad [\text{cm s}^{-1}] \quad (8.2)$$

is the mean electron speed. See, however, [Masters et al. \(1977\)](#). They show that this emission process is likely to be optically thick under some circumstances. Cyclotron optical depth effects are not now treated, so this cooling rate is likely to be an overestimate.

Magnetic pressure is included in the gas equation of state.¹ The magnetic pressure in the general case will be

$$P_{mag} = \frac{B_{\text{tangled}}^2}{8\pi} + \frac{B_{\text{tangential}}^2 - B_{\text{parallel}}^2}{8\pi} \quad [\text{dynes cm}^{-2}] \quad [\text{erg cm}^{-3}]. \quad (8.3)$$

¹The pressure associated with the magnetic field was not included in the total pressure in versions 95 and earlier of the code.

and the enthalpy density is

$$w_{mag} = \frac{\gamma}{\gamma - 1} \frac{B_{\text{tangled}}^2}{8\pi} + \frac{B_{\text{tangential}}^2 + B_{\text{parallel}}^2}{4\pi} \quad [\text{dynes cm}^{-2}] [\text{erg cm}^{-3}]. \quad (8.4)$$

The field strength is determined from local conditions across the cloud. A tangled field will have a strength that is related to the local density by equation 8.4. To force a constant magnetic field specify $\gamma = 0$. An ordered field is assumed to have constant strength if the gas is stationary. If the gas is moving (a wind solution is being performed) then the component in the radial direction (the parallel component) is constant and the transverse field has a strength that is given by (Cowling, 1976)

$$B_t = B_t^0 \frac{u_o^2 - u_A^2}{u u_0 - u_A^2}. \quad (8.5)$$

where u_A is the Alfvén velocity at illuminated face,

$$u_A^2 = \frac{B_{\text{parallel}}^2}{4\pi\rho_0} \quad [\text{cm}^2\text{s}^{-2}]. \quad (8.6)$$

For reference, a tangled field will have a pressure equivalent to the thermal pressure of a gas with density n and temperature T when

$$P_{mag}/k = \frac{B^2}{8\pi} \frac{1}{k} = B^2 2.882 \times 10^{14} \approx nT \quad [\text{cm}^{-3}\text{K}]. \quad (8.7)$$

In the ISM this magnetic pressure is often roughly equal to the ram or turbulent pressure

$$P_{ra,}/k = pu^2/2k = 60.14nu_{km}^2 s^{-1} \approx nT \quad [\text{cm}^{-3}\text{K}]. \quad (8.8)$$

where the last velocity is in km/s and n is the nucleon density (cm^{-3}). For comparison, the Alfvén velocity, the speed at which magnetic fields convey information, is

$$u_A = \frac{B}{(4\pi\rho)^{1/2}} \approx 2.19 \times 10^6 B n^{-1/2} \quad [\text{km s}^{-1}]. \quad (8.9)$$

Cosmic rays should not be included when a magnetic field is specified, since the effects of a field on cosmic ray transport are not now treated. A warning will be printed if both are included.

8.3 Cosmic ray interactions

The implementation of cosmic rays was done in collaboration with Richard Mushotzky. This section is taken from Ferland and Mushotzky (1984).

Synchrotron radio sources are usually modeled in terms of an interaction between a magnetic field and a relativistic gas with a typical energy per electron of a few hundred MeV (see Pacholczyk, 1970; Longair, 1981). The spectral index of the radio emission for radio-loud active galaxies is usually ~ -0.7 , and this suggests that the electrons, which make the dominant contribution to synchrotron emission, have a density (per unit energy interval) given by

$n(cr, E) \sim E^{-2.4}$ (Kellermann, 1966). The total relativistic electron density is sensitive to the lower bound of the energy distribution, which is typically of order 10–100 MeV, corresponding to relativistic factor of $\gamma \sim 10 - 100$ (Lea and Holman, 1978).

The cosmic ray density used by CLOUDY is defined as

$$n(cr) = \int_{E_{\min}}^{E_{\max}} n(cr, E) dE \quad [\text{cm}^{-3}] \quad (8.10)$$

with the lower bound set to $E_{\min} = 5$ MeV, corresponding to $\gamma \sim 10$. The density is only weakly sensitive to the upper limit $E_{\max} \approx 10$ GeV because of the strong convergence of the electron density function, although uncertainties in the lower energy bound introduce a fundamental uncertainty. Cosmic ray protons should have much smaller affects than the electrons, so the total cosmic ray electron density $n(cr)$ is the only parameter.

The code assumes that the gas is “optically thin” to the energetic electrons. Serious and fundamental uncertainties afflict detailed treatments of the penetration of energetic particles into gas, particularly if magnetic fields are present. In the simplest case penetration is impeded only by ionization and heating losses resulting from two-body collisions. In this case the ability to heat an entire cloud is determined by the range of a particle, or the column density of gas required to stop it (see Rossi, 1952). Relativistic electrons have a range that is given to within 15% by (Berger and Seltzer, 1965)

$$R_e = 10^{25} \left(\frac{E}{100 \text{ MeV}} \right)^{0.8} \quad [\text{cm}^{-2}] \quad (8.11)$$

for a gas composed of neutral hydrogen. The range of a 100 MeV electron in a fully ionized gas, in which bremsstrahlung and Coulomb losses are more important than ionization, would be some 10 times smaller.

The relativistic particles both heat and ionize the gas. The main concern is for the rate with which energy is transferred to the cold gas as discussed by Lea and Holman (1978) and Ginzburg and Syrovatskii (1964). In the H^+ zone the main interaction will be with free electrons. Kinetic energy is passed to the cold electrons at a rate

$$G_{cr} = 8.5 \times 10^{-19} n_e n(cr) \quad [\text{erg cm}^{-3} \text{s}^{-1}] \quad (8.12)$$

by direct Coulomb interactions (Jackson, 1975; Spitzer, 1962; Ginzburg and Syrovatskii, 1964; Pacholczyk, 1970). Here n_e is the thermal electron density, and the integration is over the electron distribution given above.

In regions where hydrogen is neutral the main interaction between thermal and relativistic gases is through ionization of the cold gas. For large neutral fractions very little of the energy of secondary electrons goes into actually heating the gas (Rossi, 1952; Spitzer and Tomasko, 1968). Calculations show that secondary electrons have typical energies of ~ 40 eV, and that there is roughly one ionization per 15 eV deposited. Using the Bethe-Bloch approximation (Ginzburg and Syrovatskii, 1964) the neutral heating rate is

$$G_{cr} = 3.7 \times 10^{-20} n(H^0) n(cr) \quad [\text{erg cm}^{-3} \text{s}^{-1}] \quad (8.13)$$

and the H^0 ionization rate is

$$\Gamma = 1.5 \times 10^{-8} n(cr) n(H^0) \quad [\text{s}^{-1}]. \quad (8.14)$$

This ionization rate was scaled through [Lotz \(1967\)](#)'s curves to include collisional ionization of heavy elements in the calculation of heavy element ionization equilibria.

If cosmic rays are not included, and the hydrogen ground state photoionization rate falls below the galactic background cosmic ray ionization rate, then a comment will be generated warning that the cosmic ray background should perhaps be included. According to [Spitzer \(1978\)](#), the background cosmic ray ionization rate is very uncertain, but of the order of $2 \times 10^{-17} \text{ s}^{-1}$ for neutral hydrogen. According to the equations above, this rate corresponds to a cosmic ray density of $\sim 2 \times 10^{-9} \text{ cm}^{-3}$, the value used as the “background” cosmic ray density option for the **cosmic ray** command.

The discussion above, as well as the code, includes only two-body Coulomb interactions, and *does not* include collective effects, such as those discussed by [Scott et al. \(1980\)](#). [Rephaeli \(1987\)](#) notes that collective effects may not be important in most circumstances.

8.4 Secondary ionization

8.4.1 Ionization, heating, and cooling

Although the electron velocity distribution is predominantly Maxwellian ([Bohm and Aller, 1947](#)), a small constituent of non-thermal secondary electrons may be present when high-energy radiation is present. Secondary ionizations by supra-thermal electrons are treated following [Xu and McCray \(1991\)](#) and [Dalgarno et al. \(1999\)](#). All sources of energetic electrons, including both Auger and primary electrons, are considered in the initial input of high-energy electrons into the gas. A typical energy of an electron in the non-thermal shower is $\sim 20 \text{ eV}$; this energy is used to evaluate collisional ionization and excitation cross sections. Secondary ionization is included among the general ionization processes considered for all species.

8.4.2 Secondary rates per atom

The heating efficiency, the ionization efficiency, and the efficiency for exciting $L\alpha$ are functions of the neutral fraction and must be determined. In the following equations ϵ_{Ryd}^* is the initial energy of the hot photoelectron. These efficiencies are defined relative to this energy.

heating efficiency This is a fraction (between 0 and 1) of the energy of the photoelectron that goes into heating the Maxwellian electron bath. The heat actually deposited in the free electrons ($\text{Ryd cm}^3 \text{ s}^{-1}$) is given by

$$L_{\text{sec}} = \epsilon_{Ryd}^* \times \text{HEATEF} \quad [\text{erg cm}^{-3} \text{ s}^{-1}]. \quad (8.15)$$

H ionization rate This is the number of hydrogen ionizations produced per Rydberg of heat input by suprathemal electrons. The number (s^{-1}) of knock-on secondary ionizations is given by

$$r_{\text{ion}} = \text{CSUPRA} = \epsilon_{Ryd}^* \times \text{EFIONZ} \quad [s^{-1}], \quad (8.16)$$

excitation rate This is the energy in Rydbergs that goes into $L\alpha$ excitations. The number of excitations of $L\alpha$ is given by

$$r_{Ly\alpha} = \text{SECLA} = \epsilon_{Ryd}^* \times \text{EXCTEF} \times 4/3 \quad [s^{-1}], \quad (8.17)$$

Table 8.1: Secondary Ionization Efficiencies

Electron Fraction	Secondary Ionization	Heating Efficiency	Ly α Excitations	Sum
1.00E-04	3.75E-01	1.11E-01	4.19E-01	9.06E-01
3.16E-04	3.66E-01	1.51E-01	3.99E-01	9.15E-01
1.00E-03	3.51E-01	2.03E-01	3.71E-01	9.25E-01
3.16E-03	3.28E-01	2.73E-01	3.35E-01	9.36E-01
1.00E-02	2.92E-01	3.66E-01	2.87E-01	9.45E-01
3.16E-02	2.39E-01	4.87E-01	2.25E-01	9.51E-01
1.00E-01	1.64E-01	6.40E-01	1.50E-01	9.54E-01
3.16E-01	6.98E-01	8.24E-01	6.50E-01	9.59E-01
1.00E+00	0.00E+00	9.97E-01	0.00E+00	9.97E-01

8.4.3 Total interaction rates

The interaction rates per unit volume are given by the rates per atom and the density of the atom. This results in the total number of secondary interactions per unit volume. This total rate is converted into a rate per target atom by dividing the volume rate by the number of *atoms* per unit volume. The results are the rates (with units s^{-1}) referred to by the variable *csupra* (secondary ionization rate) and *x12* (secondary rate of excitation of Lyman lines).

8.4.4 Rates during the hydrogen balance solution

In deep regions of x-ray ionized clouds the dominant source of secondaries is often inner shell ionization of the heavy elements, especially oxygen. Often secondary ionization is the dominant ionization source of hydrogen, and in this case the secondary ionization rate changes as the electron density changes, during searches for the ionization balance. It would not be computationally expedient to reevaluate all heavy element ionization rates during the search for the hydrogen ionization balance, so, during this search an effective secondary ionization rate, given by a simple scaling law using the current electron fraction, and the secondary rate and electron fraction where it was last evaluated.

8.4.5 Molecules and Suprathermal Electrons

The collisional and heating effects of the suprathermal secondary electrons following inner-shell photoionization are treated using standard assumptions (Bergeron and Souffrin, 1971; Shull and van Steenberg, 1985; Voit, 1991). Eight eV of heat is deposited for each H_2 ionization by a cosmic ray (Tielens and Hollenbach, 1985). Relative rates are taken from Hollenbach and McKee (1989).

The result of this is a secondary ionization rate that must then be multiplied by scale factors that account for the relative collision cross section for each species relative to hydrogen. These are taken from (Tielens and Hollenbach, 1985) and Hollenbach and McKee (1989).

Secondary electrons also produce a diffuse background of electronic H_2 lines that can photodissociate most molecules. This is treated using the scaling rule of (Gredel et al., 1987) and Gredel et al. (1989).

8.5 Pressure laws

8.5.1 Units

Pressure is force per unit area. The unit of force in the cgs system is the dyn, which is 10^{-5} N. The fundamental units of the dyn are g cm s^{-2} . For pressure these are dyn cm^{-2} or $\text{gm cm}^{-1} \text{s}^{-2}$.

8.5.2 Ideal gas laws

For a non-relativistic non-degenerate gas the energy density is

$$u = \frac{3}{2} n_{tot} k T_e \quad [\text{dyne cm}^{-2}; \text{erg cm}^{-3}] \quad (8.18)$$

and the pressure is

$$P_{gas} = n_{tot} k T_e = \frac{2}{3} u \quad [\text{dynes cm}^{-2}; \text{erg cm}^{-3}]. \quad (8.19)$$

n_{tot} is the total particle density (cm^{-3}). For a relativistic non-degenerate gas the energy density is

$$u = 3 n_{tot} k T_e \quad [\text{dynes cm}^{-2}; \text{erg cm}^{-3}] \quad (8.20)$$

and the pressure is

$$P_{gas} = n_{tot} k T_e = \frac{1}{3} u \quad [\text{dynes cm}^{-2}; \text{dynes cm}^{-2}]. \quad (8.21)$$

In general the internal energy of a gas with pressure P and volume V is

$$U = PV / (\gamma - 1) \quad [\text{erg}] \quad (8.22)$$

where γ is the ratio of principal specific heats, $\gamma = 5/3$ for a non-relativistic plasma.

8.5.3 Equation of state

When the pressure is held constant (with the **constant pressure** command) the pressure law is given by

$$P(r) = P_{gas}(r_o) + \int a_{rad} \rho dr = P_{gas}(r) + P_{line}(r) \quad (8.23)$$

where

$$P_{gas}(r_o) = n_{tot} k T \quad (8.24)$$

is the gas pressure at the illuminated face of the cloud, the total particle density is n_{tot} , and r is the radius of the current position.

8.5.4 Turbulent pressure

Turbulence can be included as a line broadening mechanism. It modifies line opacities and the resulting optical depths, and adds a component of ram pressure to the total pressure, given by

$$P_{turb}(r_o) = \frac{1}{2} \rho u_{turb}^2 = 5.8 \times 10^6 \left(\frac{n}{10^5 \text{ cm}^{-3}} \right) \left(\frac{u_{turb}}{1 \text{ km s}^{-1}} \right)^2 \quad [\text{dynes cm}^{-2}; \text{cm}^{-3} \text{K}] \quad (8.25)$$

where n is the density and u_{turb} is the turbulent velocity. Turbulent pressure is not included in the constant pressure law since it would be either negligible, or so large that it would not be possible to determine the gas pressure.

8.5.5 Ram or dynamic pressure

Pressure associated with energy of bulk motion can be referred to as ram or dynamic pressure. Ram pressure is given by ρu^2 .

8.6 Line radiation pressure

Line radiation pressure was implemented in CLOUDY in collaboration with Moshe Elitzur. The following was written in collaboration with Moshe, and is adopted from [Elitzur and Ferland \(1986\)](#).

8.6.1 Formalism

For radiation intensity I_ν , the standard expression for the radiation pressure per unit frequency, P_ν , is (e.g. [Schwarzschild \(1965\)](#))

$$P_\nu = \frac{1}{c} \int I_\nu \mu^2 d\Omega \quad [\text{dynes cm}^{-2}; \text{erg cm}^{-3}], \quad (8.26)$$

where $\mu = \cos(\theta)$ and θ is the direction of propagation of the radiation. When the radiation field is isotropic, its pressure and energy density,

$$u_\nu = \frac{1}{c} \int I_\nu d\Omega \quad [\text{dynes cm}^{-2}; \text{erg cm}^{-3}], \quad (8.27)$$

are related by the familiar expression

$$P_\nu = \frac{1}{3} u_\nu \quad [\text{dynes cm}^{-2}; \text{erg cm}^{-3}]. \quad (8.28)$$

This relation holds for a rather wide range of circumstances. If the angular distribution of I_ν is expanded in a power series in μ , then only powers higher than the second will lead to violations of equation 28. However, the successive coefficients of this expansion are decreasing approximately like the optical depth (e.g. [Schwarzschild, 1965](#), p 40), so deviations from equation 28 will only be proportional to $1/\tau^2$. Hence, when the medium is optically thick at the frequency equation 28 is an excellent approximation for the radiation pressure.

The only radiative quantity we need to know in order to calculate the radiation pressure is the angle-averaged flux, J_ν , since

$$u_\nu = \frac{1}{c} 4\pi J_\nu \quad [\text{dynes cm}^{-2}; \text{erg cm}^{-3}]. \quad (8.29)$$

The integrated radiation pressure is then

$$P(\nu) = \frac{4\pi}{3c} \int J_\nu d\nu \quad [\text{dynes cm}^{-2}; \text{erg cm}^{-3}]. \quad (8.30)$$

Introducing the line-width, defined by

$$\Delta\nu = \frac{1}{\bar{J}_{u,l}} \int J_\nu d\nu \quad [\text{Hz}] \quad (8.31)$$

where

$$\bar{J}_{u,l} = \int J_\nu \Phi(\nu) d\nu \quad [\text{erg cm}^{-2} \text{s}^{-1} \text{sr}^{-1}] \quad (8.32)$$

is the integrated mean intensity in the line and Φ is the normalized line profile $[\int \Phi(\nu) d\nu = 1]$. The quantity \bar{J} is readily available in the escape probability approximation because it is related directly to the source function S by

$$\bar{J}_{u,l} = S(1 - P_{u,l}) \quad [\text{erg cm}^{-2} \text{s}^{-1} \text{sr}^{-1}] \quad (8.33)$$

where $P_{u,l}$ is the photon escape probability. The line source function S is simply $B_\nu(T_{\text{exc}})$, the Planck function of the line excitation temperature. The final expression for the pressure due to a line at frequency ν is therefore

$$P(\nu) = \frac{4\pi}{3c} B_\nu(T_{\text{exc}}) \Delta\nu (1 - P_{u,l}) \quad [\text{dynes cm}^{-2}; \text{erg cm}^{-3}]. \quad (8.34)$$

Combining equation 8.34 with the definition of the line source function we obtain the final form of the line radiation pressure,

$$P(\nu) = \frac{8\pi h \nu^3}{3c^3} \frac{n_u/g_u}{(n_l/g_l - n_u/g_u)} \Delta\nu (1 - P_{u,l}) \quad [\text{dynes cm}^{-2}; \text{erg cm}^{-3}]. \quad (8.35)$$

In these expressions the line width is given in frequency units. Within the code the line width is given in velocity units, and the line pressure is given as

$$\begin{aligned} P(\nu) &= \frac{8\pi h \nu^4}{3c^4} \frac{n_u/g_u}{(n_l/g_l - n_u/g_u)} \Delta\nu (1 - P_{u,l}) = \frac{8\pi h}{3\lambda^4} \frac{n_u/g_u}{(n_l/g_l - n_u/g_u)} \Delta\nu (1 - P_{u,l}) \\ &= 6.872 \times 10^{68} \nu^4 \frac{n_u/g_u}{(n_l/g_l - n_u/g_u)} \Delta\nu (1 - P_{u,l}) \\ &= 5.551 \times 10^{26} \lambda^{-4} \frac{n_u/g_u}{(n_l/g_l - n_u/g_u)} \Delta\nu (1 - P_{u,l}) \end{aligned} \quad (8.36)$$

8.6.2 Line width

The line width is a crucial parameter in the calculations since the line radiation pressure is directly proportional to it. For lines with a moderate optical depth (i.e., $\tau \leq 10^4$) the damping wings are optically thin, and the line emission profile is essentially identical to the absorption profile. Then the profile is simply described by the Doppler profile $\pi^{1/2} \exp(-x^2)$, where $x = (v - v_o)/\Delta v_{Dop}$ is the dimensionless frequency shift from line center and $\Delta v_{Dop} = (2kT/m)^{1/2} v_o/c$ is the Doppler width. The line full width is then

$$\Delta v = \Delta v_{Dop} \times 2(\ln \tau)^{1/2} \quad [\text{Hz}] \quad (8.37)$$

for $\tau \cong 1$.

The situation when the line optical depth exceeds $\sim 10^4$ is much more complicated. This is because scattering in the damping wings becomes significant, and the frequency dependence of the emission profile is not known before the entire radiative transfer problem is solved. In general, it is known that, for $L\alpha$ (generally the most important source of line radiation pressure) and large optical depths, the line width (in dimensionless units) is

$$x = k(a\tau)^{1/3}, \quad (8.38)$$

(Adams, 1972; Harrington, 1973; Bonilha et al. 1979). In this expression a is the damping constant ($a \approx 4.72 \times 10^{-4} t_4^{-1/2}$ for $L\alpha$), τ is the line center optical depth, t_4 is the temperature in units of 10^4 K, and k is a number of order unity.

The frequency width required here is the value that will provide a rectangular profile with the same area as the proper integral of the source function. The results of Adams (1972) are adopted, and the resulting expression for the full line width in the case of large optical depths ($\tau \cong 1$) is

$$\Delta v = \Delta v_{Dop} 2.3(\tau)^{1.3} \quad (8.39)$$

An important point, evident from the plots provided by Adams for the source function as a function of frequency (his Fig 3), is that the width of the frequency distribution varies very little with position in the slab. This is also evident from the mean intensity plots of Harrington, as mentioned above, and is a result of the strong coupling between distant regions caused by scattering in the line wings. The expression provided in equation 39 for all locations in the slab, with being half the total slab thickness.

8.6.3 Background opacity and thermalization

Background opacity is included in the determination of the level populations using the formalism outlined in the section on line radiative transfer. Its main effect is to lower the line excitation temperature by providing a second “escape” (actually destruction) route for trapped photons. This is assumed to be the only effect background opacity has on radiation pressure. Balmer continuous absorption typically has an optical depth only of order unity, while the line optical depths are many orders of magnitude larger. Absorption in the Balmer continuum can only compete with line scattering in the extreme wings, at frequency shifts exceeding $\sim (a\tau)^{1/2}$, which are much larger than the line width predicted by equation 8.39.

Collisional de-excitation can also break the assumption of pure scattering because a photon will be lost to the thermal pool before the radiative process can take place. This will happen when the density is high enough that the rate for collisional de-excitation, C_{ul} , exceeds the probability for the effective rate for the transition, $P_{ul}A_{ul}$, where P_{ul} is the line escape probability and A_{ul} is the Einstein coefficient. Because at large optical depths P_{ul} is essentially equal to τ^1 , the “effectively thin” assumption breaks down when

$$\tau \approx A_{u,l}/C_{u,l}. \quad (8.40)$$

Once the line optical depth exceeds $\sim A/C$, a “thermalization limit” is encountered, and the assumption of a purely scattering nebula does not apply anymore. Therefore, in evaluating the optical depth for the line width expression (equation 8.39) the minimum of the actual line optical depth and the one prescribed by A/C is used. This is a conservative estimate of the effect of collisions on photon scattering. This is probably the most poorly understood part of the calculation of the line radiation pressure.

8.7 Radiative acceleration

The radiative acceleration due to the direct attenuated continuum flux F_v , for density ρ , is given by

$$a_{rad} = \frac{1}{\rho c} \int F_v \bar{\kappa}_v dv + \frac{1}{\rho c} \sum_l F_v(l) \kappa_l \gamma_l B_{l,u} \quad [\text{cm s}^{-2}]. \quad (8.41)$$

Here $\bar{\kappa}_v$ is the effective continuous opacity. The radiative acceleration includes the usual photoelectric and free-free absorption in the gas, and Compton and Rayleigh scattering. In addition it includes the term $\kappa_{abs} + (1 - g)\kappa_s$ for the grain contributions if grains are present. The integral is over all energies considered by the code (from $\nu = 10$ MHz to $h\nu \approx 100$ MeV).

The second term is a sum is over all transferred lines (typically 10^4 to 10^5 transitions). Here κ_l is the line opacity, $B_{l,n}$ is the Einstein coefficient, and γ_l is the escape probability in the direction towards the source of ionizing radiation (Ferland and Rees, 1988).

8.8 Wind geometry

CLOUDY will do a wind geometry if the **wind** command is specified with a positive velocity. The effective acceleration is written as $a_{eff} = a_{rad} - g_{grav}$, where a_{rad} is computed in equation 8.41 above, and g_{grav} is the inward gravitational acceleration due to the central object. By default the mass of the central object is one solar mass. The velocity is computed assuming that the acceleration is constant across the zone. In this case the change in the wind velocity v between the inner and outer edges of a zone of thickness dr will be

$$u^2 - u_o^2 = 2a_{eff} dr \quad [\text{cm}^2\text{s}^{-2}] \quad (8.42)$$

where u_o is the velocity at the inner edge. The calculation will stop if the velocity ever falls below zero.

The density is varied across the model to conserve mass flux (i.e., the product $\rho(r)r^2u(r)$ is kept constant). Because of this, a filling factor would not make physical sense, and should not be used.

Note also that it is usually necessary to set an outer radius when a wind model is computed to stop the calculation from extending to infinity.

The Sobolev or large velocity gradient (LVG) approximation is used for line transfer when a wind is computed. In the constant expansion velocity case the effective optical depth is given by;

$$\tau_{l,u}(r) = \alpha_{l,u} \left(n_l - n_u \frac{g_l}{g_u} \right) r \frac{u_{th}}{\max(u_{th}, u_{exp})} \quad (8.43)$$

where r is the smaller of the radius or depth and u_{th} and u_{exp} are the thermal and expansion velocities respectively. The choice of the smaller of the radius or depth is not in strict keeping with the Sobolev approximation, but is necessary since calculations often begin at very large radii from the central object. The optical depths would have unphysically large values were this choice not made.

In the case where the code actually solves for the velocity, which is then not constant, the effective optical depth is given by (Castor et al., 1975)

$$\tau_{l,u}(r) = \alpha_{l,u} \left(n_l - n_u \frac{g_l}{g_u} \right) v_{th} \left| \frac{dv}{dr} \right|^{-1} \quad (8.44)$$

where dv/dr is the acceleration.

Figure 8.1 shows a test case in which a wind is driven in the plane parallel electron scattering limit. As can be seen the numerical solution is in excellent agreement with the analytically predicted result.

8.9 Eddington limit

The Eddington limit is given by

$$L_{Edd} = \frac{4\pi GcM}{\kappa} = 1.45 \times 10^{38} \frac{M}{M_o} \frac{\kappa_T}{\kappa} \quad [\text{erg s}^{-1}] \quad (8.45)$$

where κ_T is the Thomson opacity and κ is the actual gas opacity (generally several orders of magnitude above Thomson).

8.10 Jeans length and mass

The Jeans length and mass are computed for each zone in the calculation. The smallest computed Jeans length and mass are saved, and a note is printed at the end of the calculation if the computed structure is Jeans unstable.

The expression for the Jeans length is

$$\lambda_J = \left(\frac{\pi k T}{\mu m_u G \rho} \right)^{1/2} = 6.257 \times 10^7 \left(\frac{T}{\mu \rho} \right)^{1/2} \quad [\text{cm}] \quad (8.46)$$

where μ is the mean mass per particle of the gas

$$\mu = \frac{\sum n_i m_i}{\sum n_i} \quad [\text{gm}]. \quad (8.47)$$

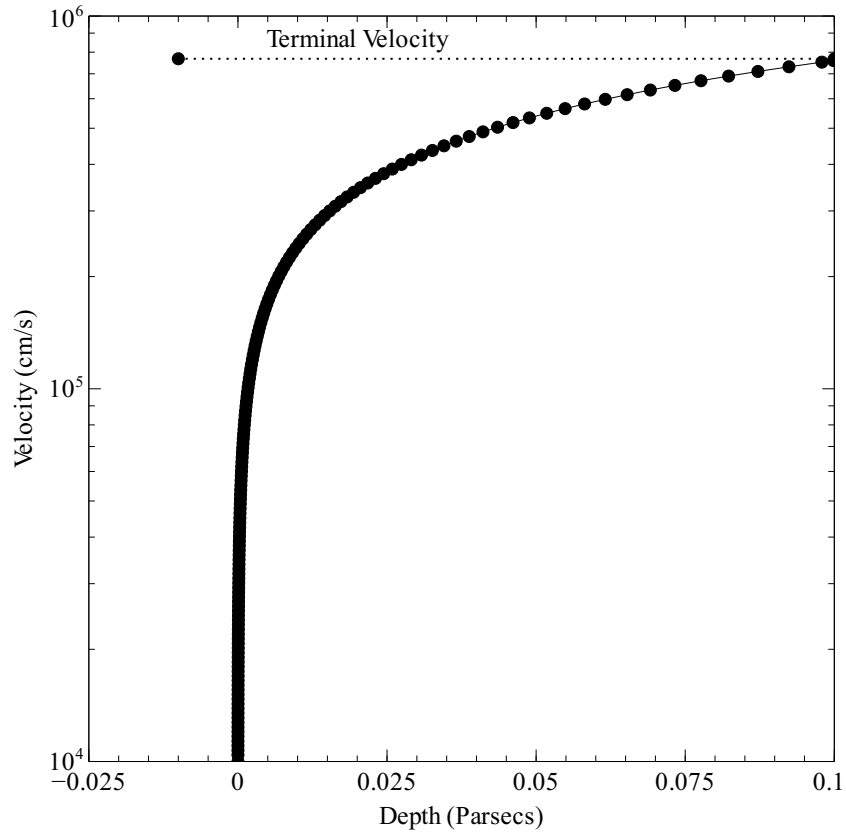


Figure 8.1: The wind velocity is computed using the input stream shown in one of the test cases in the last section. Parameters were chosen to have a readily computed final velocity. The velocity at the outer edge of the slab is within 1 percent of its expected value.

The Jeans mass is then given by

$$M_J = \frac{4\pi}{3} \rho \left(\frac{\lambda_J}{2} \right)^3 \quad [\text{gm}] \quad (8.48)$$

where the mass is that of a sphere with radius $\lambda_J/2$.

The minimum Jeans mass is evaluated as the calculation progresses. The code will generate a comment if the computed structure is Jeans unstable.

8.11 Luminosity Distance

The luminosity distance DL is given by

$$D_L = \begin{cases} \frac{cz}{H_o} (1+z/2) & q_o = 0 \\ \frac{c}{H_o q_o^2} \left\{ q_o z + (q_o - 1) \left[(2q_o z + 1)^{1/2} - 1 \right] \right\} & q_o > 0 \\ \frac{2c}{H_o} \left[1 + z - (1+z)^{1/2} \right] & q_o = 1/2 \end{cases} \quad [\text{cm}] \quad (8.49)$$

For $q_o = 1/2$ and $H_o = 70 \text{ km/s/Mpc}$ the luminosity distance is

$$D_L = 2.643 \times 10^{26} \left[1 + z - (1+z)^{1/2} \right] \quad [\text{cm}] \quad (8.50)$$

The proper distance D_P is given by $D_P = D_L (1+z)$.

[Liske \(2000\)](#) provides expressions giving the cosmological distance and redshift between any two objects. [Hogg \(1999\)](#) gives a nice pedagogical review of distance measures in cosmology.

REFERENCES

- N. P. Abel, G. J. Ferland, G. Shaw, and P. A. M. van Hoof. The H II Region/PDR Connection: Self-consistent Calculations of Physical Conditions in Star-forming Regions. *ApJS*, 161:65–95, November 2005. doi: 10.1086/432913.
- T. F. Adams. The Escape of Resonance-Line Radiation from Extremely Opaque Media. *ApJ*, 174:439, June 1972. doi: 10.1086/151503.
- C. Allende Prieto, D. L. Lambert, and M. Asplund. The Forbidden Abundance of Oxygen in the Sun. *ApJL*, 556:L63–L66, July 2001. doi: 10.1086/322874.
- C. Allende Prieto, D. L. Lambert, and M. Asplund. A Reappraisal of the Solar Photospheric C/O Ratio. *ApJL*, 573:L137–L140, July 2002. doi: 10.1086/342095.
- M. Arnaud and J. Raymond. Iron ionization and recombination rates and ionization equilibrium. *ApJ*, 398: 394–406, October 1992. doi: 10.1086/171864.
- M. Arnaud and R. Rothenflug. An updated evaluation of recombination and ionization rates. *A&AS*, 60: 425–457, June 1985.
- J. A. Baldwin, G. J. Ferland, P. G. Martin, M. R. Corbin, S. A. Cota, B. M. Peterson, and A. Slettebak. Physical conditions in the Orion Nebula and an assessment of its helium abundance. *ApJ*, 374: 580–609, June 1991. doi: 10.1086/170146.
- DR Bates, AE Kingston, and RWP McWhirter. Recombination Between Electrons and Atomic Ions. I. Optically Thin Plasmas. *Proceedings of the Royal Society of London. Series A, Mathematical and Physical Sciences (1934-1990)*, 267(1330):297–312, 1962.
- R. P. Bauman, R. L. Porter, G. J. Ferland, and K. B. MacAdam. J-Resolved He I Emission Predictions in the Low-Density Limit. *ApJ*, 628:541–554, July 2005. doi: 10.1086/430665.
- M. J. Berger and S. M. Seltzer. Results of Some Recent Transport Calculations for Electrons and Bremsstrahlung. *NASA Special Publication*, 71:437, August 1965.
- J. Bergeron and S. Souffrin. Optical line spectrum of a gas heated by hard UV radiation or energetic particles. *A&A*, 14:167–188, September 1971.
- K. A. Berrington and J. C. Pelan. Atomic data from the IRON Project. XII. Electron excitation of forbidden transitions in V-like ions MN III, Fe IV, CO V and NI VI. *A&AS*, 114:367, December 1995.
- K. A. Berrington, S. Nakazaki, and P. H. Norrington. Atomic data from the IRON Project. XLI. Electron excitation rates among the $3d^2$ fine-structure levels of Ca-like Fe VII. *A&AS*, 142:313–316, March 2000. doi: 10.1051/aas:2000152.
- J. H. Black. Molecules in planetary nebulae. *ApJ*, 222:125–131, May 1978. doi: 10.1086/156128.
- J. H. Black, J. C. Weisheit, and E. Laviana. Oscillator Strengths and Ground-State Photoionization Cross-Sections for Mg^+ and Ca^+ . *ApJ*, 177:567, October 1972. doi: 10.1086/151733.
- D. Bohm and L. H. Aller. The Electron Velocity Distribution in Gaseous Nebulae and Stellar Envelopes. *ApJ*, 105:131, January 1947.

- I. S. Bowen. Wave Lengths of Forbidden Nebular Lines. II. *ApJ*, 132:1, July 1960. doi: 10.1086/146893.
- J. T. Broad and W. P. Reinhardt. One- and two-electron photoejection from H^- : A multichannel J-matrix calculation. *PhRvA*, 14:2159–2173, December 1976. doi: 10.1103/PhysRevA.14.2159.
- R. L. Brown and W. G. Mathews. Theoretical Continuous Spectra of Gaseous Nebulae. *ApJ*, 160:939, June 1970. doi: 10.1086/150483.
- J. I. Castor, D. C. Abbott, and R. I. Klein. Radiation-driven winds in Of stars. *ApJ*, 195:157–174, January 1975. doi: 10.1086/153315.
- S. Cazaux and A. G. G. M. Tielens. Molecular Hydrogen Formation in the Interstellar Medium. *ApJL*, 575:L29–L32, August 2002. doi: 10.1086/342607.
- M. C. Chidichimo. Electron impact excitation cross sections of Ca^{+} at low energies. *Journal of Physics B Atomic Molecular Physics*, 14:4149–4164, November 1981. doi: 10.1088/0022-3700/14/21/026.
- T. G. Cowling. *Magnetohydrodynamics*. Bristol: Adam Hilger, 1976.
- M. Crosas and J. C. Weisheit. Hydrogen molecules in quasar broad-line regions. *MNRAS*, 262:359–368, May 1993.
- A. Dalgarno and A. E. Kingston. Radiative attachment of electrons to atomic hydrogen. *The Observatory*, 83:39–40, February 1963.
- A. Dalgarno and R. A. McCray. The Formation of Interstellar Molecules from Negative Ions. *ApJ*, 181:95–100, April 1973. doi: 10.1086/152032.
- A. Dalgarno and W. G. Roberge. Collision-induced dissociation of interstellar molecules. *ApJL*, 233:L25–L27, October 1979. doi: 10.1086/183069.
- A. Dalgarno, M. Yan, and W. Liu. Electron Energy Deposition in a Gas Mixture of Atomic and Molecular Hydrogen and Helium. *ApJS*, 125:237–256, November 1999. doi: 10.1086/313267.
- N. A. Doughty, P. A. Fraser, and R. P. McEachran. The bound-free absorption coefficient of the negative hydrogen ion. *MNRAS*, 132:255, 1966.
- J. E. Dove and M. E. Mandy. The rate of dissociation of molecular hydrogen by hydrogen atoms at very low densities. *ApJL*, 311:L93–L96, December 1986. doi: 10.1086/184805.
- J. E. Dove, A. C. M. Rusk, P. H. Cribb, and P. G. Martin. Excitation and dissociation of molecular hydrogen in shock waves at interstellar densities. *ApJ*, 318:379–391, July 1987. doi: 10.1086/165375.
- B. T. Draine. Photoelectric heating of interstellar gas. *ApJS*, 36:595–619, April 1978. doi: 10.1086/190513.
- B. T. Draine and H. M. Lee. Optical properties of interstellar graphite and silicate grains. *ApJ*, 285:89–108, October 1984. doi: 10.1086/162480.
- B. T. Draine and E. E. Salpeter. On the physics of dust grains in hot gas. *ApJ*, 231:77–94, July 1979. doi: 10.1086/157165.
- B. T. Draine and B. Sutin. Collisional charging of interstellar grains. *ApJ*, 320:803–817, September 1987. doi: 10.1086/165596.
- M. Elitzur, editor. *Astronomical masers*, volume 170 of *Astrophysics and Space Science Library*, 1992.
- M. Elitzur and G. J. Ferland. Radiation pressure and emission clouds around active galactic nuclei. *ApJ*, 305:35–44, June 1986. doi: 10.1086/164226.
- A. C. Fabian, J. E. Pringle, and M. J. Rees. X-ray emission from accretion on to white dwarfs. *MNRAS*, 175:43–60, April 1976.
- G. J. Ferland. Hydrogenic emission and recombination coefficients for a wide range of temperature and wavelength. *PASP*, 92:596–602, October 1980. doi: 10.1086/130718.
- G. J. Ferland and R. F. Mushotzky. Cosmic rays and the emission-line regions of active galactic nuclei. *ApJ*, 286:42–52, November 1984. doi: 10.1086/162574.

- G. J. Ferland and S. E. Persson. Implications of Ca II emission for physical conditions in the broad-line region of active galactic nuclei. *ApJ*, 347:656–673, December 1989. doi: 10.1086/168156.
- G. J. Ferland and M. J. Rees. Radiative equilibrium of high-density clouds with application to active galactic nucleus continua. *ApJ*, 332:141–156, September 1988. doi: 10.1086/166639.
- G. J. Ferland, B. M. Peterson, K. Horne, W. F. Welsh, and S. N. Nahar. Anisotropic line emission and the geometry of the broad-line region in active galactic nuclei. *ApJ*, 387:95–108, March 1992. doi: 10.1086/171063.
- G. J. Ferland, A. C. Fabian, and R. M. Johnstone. The Physical Conditions Within Dense Cold Clouds in Cooling Flows. *MNRAS*, 266:399, January 1994.
- G. J. Ferland, J. A. Baldwin, K. T. Korista, F. Hamann, R. F. Carswell, M. Phillips, B. Wilkes, and R. E. Williams. High Metal Enrichments in Luminous Quasars. *ApJ*, 461:683, April 1996. doi: 10.1086/177094.
- G. J. Ferland, K. T. Korista, D. A. Verner, and A. Dalgarno. Charge Transfer between Neutral Atoms and Highly Ionized Species: Implications for ISO Observations. *ApJL*, 481:L115+, June 1997. doi: 10.1086/310655.
- G. J. Ferland, A. C. Fabian, and R. M. Johnstone. The physical conditions within dense cold clouds in cooling flows - II. *MNRAS*, 333:876–884, July 2002. doi: 10.1046/j.1365-8711.2002.05470.x.
- G. J. Ferland, M. Chatzikos, F. Guzmán, M. L. Lykins, P. A. M. van Hoof, R. J. R. Williams, N. P. Abel, N. R. Badnell, F. P. Keenan, R. L. Porter, and P. C. Stancil. The 2017 Release Cloudy. *Revista Mexicana de Astronomía y Astrofísica*, 53:385–438, October 2017.
- G. B. Field. Thermal Instability. *ApJ*, 142:531, August 1965. doi: 10.1086/148317.
- R. H. Garstang. Energy levels and transition probabilities of Fe IV. *MNRAS*, 118:572, 1958.
- V. L. Ginzburg and S. I. Syrovatskii. *The Origin of Cosmic Rays*. New York: Macmillan, 1964.
- R. J. Gould. Radiative recombination of complex ions. *ApJ*, 219:250–261, January 1978. doi: 10.1086/155772.
- R. Gredel, S. Lepp, and A. Dalgarno. The C/CO ratio in dense interstellar clouds. *ApJL*, 323:L137–L139, December 1987. doi: 10.1086/185073.
- R. Gredel, S. Lepp, A. Dalgarno, and E. Herbst. Cosmic-ray-induced photodissociation and photoionization rates of interstellar molecules. *ApJ*, 347:289–293, December 1989. doi: 10.1086/168117.
- N. Grevesse and A. J. Sauval. Standard Solar Composition. *Space Science Reviews*, 85:161–174, May 1998. doi: 10.1023/A:1005161325181.
- P. W. Guilbert. Compton heating and cooling in thermal electron gases. *MNRAS*, 218:171–175, January 1986.
- F. Hamann and G. Ferland. The Chemical Evolution of QSOs and the Implications for Cosmology and Galaxy Formation. *ApJ*, 418:11, November 1993. doi: 10.1086/173366.
- J. P. Harrington. The scattering of resonance-line radiation in the limit of large optical depth. *MNRAS*, 162: 43, 1973.
- W. J. Henney, S. J. Arthur, R. J. R. Williams, and G. J. Ferland. Self-Consistent Dynamic Models of Steady Ionization Fronts. I. Weak-D and Weak-R Fronts. *ApJ*, 621:328–347, March 2005. doi: 10.1086/427491.
- D. W. Hogg. Distance measures in cosmology. *ArXiv Astrophysics e-prints*, May 1999.
- D. Hollenbach and C. F. McKee. Molecule formation and infrared emission in fast interstellar shocks. I Physical processes. *ApJS*, 41:555–592, November 1979. doi: 10.1086/190631.
- D. Hollenbach and C. F. McKee. Molecule formation and infrared emission in fast interstellar shocks. III - Results for J shocks in molecular clouds. *ApJ*, 342:306–336, July 1989. doi: 10.1086/167595.

- H. Holweger. Photospheric Abundances: Problems, Updates, Implications. In R. F. Wimmer-Schweingruber, editor, *Joint SOHO/ACE workshop "Solar and Galactic Composition"*, volume 598 of *American Institute of Physics Conference Series*, page 23, 2001. doi: 10.1063/1.1433974.
- D. G. Hummer. A fast and accurate method for evaluating the nonrelativistic free-free Gaunt factor for hydrogenic ions. *ApJ*, 327:477–484, April 1988. doi: 10.1086/166210.
- D. G. Hummer and P. J. Storey. Recombination-line intensities for hydrogenic ions. I - Case B calculations for H I and He II. *MNRAS*, 224:801–820, February 1987.
- J. B. Hutchins. The thermal effects of H₂ molecules in rotating and collapsing spheroidal gas clouds. *ApJ*, 205:103–121, April 1976. doi: 10.1086/154254.
- J. D. Jackson. *Classical electrodynamics*, 2nd ed. New York: Wiley, 1975.
- R. K. Janev, W. D. Langer, and K. Evans. *Elementary processes in Hydrogen-Helium plasmas - Cross sections and reaction rate coefficients*. Springer Series on Atoms and Plasmas. Berlin: Springer, 1987.
- L. C. Johnson. Approximations for Collisional and Radiative Transition Rates in Atomic Hydrogen. *ApJ*, 174:227, May 1972. doi: 10.1086/151486.
- M. Jura. Formation and destruction rates of interstellar H₂. *ApJ*, 191:375–379, July 1974. doi: 10.1086/152975.
- M. Jura. Interstellar clouds containing optically thin H₂. *ApJ*, 197:575–580, May 1975. doi: 10.1086/153545.
- J. S. Kaastra and R. Mewe. X-ray emission from thin plasmas. I - Multiple Auger ionisation and fluorescence processes for Be to Zn. *A&AS*, 97:443–482, January 1993.
- K. I. Kellermann. On the Interpretation of Radio-Source Spectra and the Evolution of Radio Galaxies and Quasi-Stellar Sources. *ApJ*, 146:621, December 1966. doi: 10.1086/148940.
- J. B. Kingdon and G. J. Ferland. Rate Coefficients for Charge Transfer between Hydrogen and the First 30 Elements. *ApJS*, 106:205, September 1996. doi: 10.1086/192335.
- J. B. Kingdon and G. J. Ferland. The Effects of Charge Transfer on the Thermal Equilibrium of Photoionized Nebulae. *ApJL*, 516:L107–L109, May 1999. doi: 10.1086/312008.
- J. H. Krolik, C. F. McKee, and C. B. Tarter. Two-phase models of quasar emission line regions. *ApJ*, 249:422–442, October 1981. doi: 10.1086/159303.
- D. L. Lambert and B. E. J. Pagel. The dissociation equilibrium of H[−] in stellar atmospheres. *MNRAS*, 141:299, 1968.
- A. Laor and B. T. Draine. Spectroscopic constraints on the properties of dust in active galactic nuclei. *ApJ*, 402:441–468, January 1993. doi: 10.1086/172149.
- W. B. Latter and J. H. Black. Molecular hydrogen formation by excited atom radiative association. *ApJ*, 372:161–166, May 1991. doi: 10.1086/169961.
- J. M. Launay, M. Le Dourneuf, and C. J. Zeippen. The reversible $H + H^{-} \Rightarrow H_2(v, j) + e^{-}$ reaction – A consistent description of the associative detachment and dissociative attachment processes using the resonant scattering theory. *A&A*, 252:842–852, December 1991.
- S. M. Lea and G. D. Holman. X-ray and radio emission from clusters of galaxies - The heating of intracluster gas by relativistic electrons. *ApJ*, 222:29–39, May 1978. doi: 10.1086/156118.
- P. Lenzuni, D. F. Chernoff, and E. E. Salpeter. Rosseland and Planck mean opacities of a zero-metallicity gas. *ApJS*, 76:759–801, June 1991. doi: 10.1086/191580.
- E. V. Levich and R. A. Sunyaev. The Heating of Gas in the Vicinity of Quasars, Nuclei of Seyfert Galaxies, and Pulsars by the Induced Compton Effect. *Astrophys. Lett.*, 7:69, November 1970.

- J. Liske. On the cosmological distance and redshift between any two objects. *MNRAS*, 319:557–561, December 2000. doi: 10.1046/j.1365-8711.2000.03874.x.
- B. W. Lites and D. Mihalas. The H(-) equilibrium using coupled rate equations for H(-), H, H(+), H₂, and H₂(+). *SoPh*, 93:23–35, June 1984. doi: 10.1007/BF00156650.
- M. S. Longair. *High energy astrophysics. an informal introduction for students of physics and astronomy*. Cambridge: Cambridge University Press, 1981.
- W. Lotz. Electron-Impact Ionization Cross-Sections and Ionization Rate Coefficients for Atoms and Ions. *ApJS*, 14:207, May 1967. doi: 10.1086/190154.
- P. G. Martin. Hydrogenic radiative recombination at low temperature and density. *ApJS*, 66:125–138, February 1988. doi: 10.1086/191249.
- P. G. Martin and D. C. B. Whittet. Interstellar extinction and polarization in the infrared. *ApJ*, 357: 113–124, July 1990. doi: 10.1086/168896.
- A. R. Masters, A. C. Fabian, M. J. Rees, and J. E. Pringle. Cyclotron emission from accreting magnetic white dwarfs. *MNRAS*, 178:501–504, March 1977.
- J. S. Mathis and S. G. Wallenhorst. The size distribution of interstellar particles. III - Peculiar extinctions and normal infrared extinction. *ApJ*, 244:483–492, March 1981. doi: 10.1086/158725.
- J. S. Mathis, W. Ruml, and K. H. Nordsieck. The size distribution of interstellar grains. *ApJ*, 217: 425–433, October 1977. doi: 10.1086/155591.
- C. Mendoza. Recent advances in atomic calculations and experiments of interest in the study of planetary nebulae. In D. R. Flower, editor, *Planetary Nebulae*, volume 103 of *IAU Symposium*, pages 143–172, 1983.
- D. Mihalas. *Stellar atmospheres /2nd edition/*. San Francisco, W. H. Freeman and Co., 1978. 650 p.
- R. Morrison and D. McCammon. Interstellar photoelectric absorption cross sections, 0.03–10 keV. *ApJ*, 270:119–122, July 1983. doi: 10.1086/161102.
- D. C. Morton, D. G. York, and E. B. Jenkins. A search list of lines for quasi-stellar object absorption systems. *ApJS*, 68:449–461, November 1988. doi: 10.1086/191295.
- H. Netzer, M. Elitzur, and G. J. Ferland. Bowen fluorescence and He II lines in active galaxies and gaseous nebulae. *ApJ*, 299:752–762, December 1985. doi: 10.1086/163741.
- D. A. Neufeld. Harvard research exam, 1989.
- E. Oliva, A. Pasquali, and M. Reconditi. On [NeV] atomic parameters and physical conditions in NGC 6302. *A&A*, 305:L21+, January 1996.
- S. Oliveira and W. J. Maciel. Grains and the heating of H II regions. *Ap&SS*, 126:211–222, October 1986. doi: 10.1007/BF00639374.
- D. E. Osterbrock. Transition Probabilities of Forbidden Lines. *ApJ*, 114:469, November 1951. doi: 10.1086/145487.
- A. G. Pacholczyk. *Radio astrophysics. Nonthermal processes in galactic and extragalactic sources*. Series of Books in Astronomy and Astrophysics. San Francisco: Freeman, 1970.
- F. Palla, E. E. Salpeter, and S. W. Stahler. Primordial star formation - The role of molecular hydrogen. *ApJ*, 271:632–641, August 1983. doi: 10.1086/161231.
- B. Peart, M. A. Bennett, and K. Dolder. New measurements of the mutual neutralisation of H(+)/H(-) and He(+)/H(-) ions. *Journal of Physics B Atomic Molecular Physics*, 18:L439–L444, July 1985. doi: 10.1088/0022-3700/18/13/007.
- R. M. Pengelly and M. J. Seaton. Recombination spectra, II. *MNRAS*, 127:165, 1964.
- J. R. Peterson, W. H. Aberth, J. T. Moseley, and J. R. Sheridan. Ion-Ion Mutual Neutralization Cross

- Sections Measured by a Superimposed Beam Technique. II. $O_2^+ + O_2^-$, $O_2^+ + NO_2^-$, and $NO^+ + NO_2^-$. *PhRvA*, 3:1651–1657, May 1971. doi: 10.1103/PhysRevA.3.1651.
- R. L. Porter and G. J. Ferland. Revisiting He-like X-Ray Emission-Line Plasma Diagnostics. *ApJ*, 664: 586–595, July 2007. doi: 10.1086/518882.
- R. L. Porter, R. P. Bauman, G. J. Ferland, and K. B. MacAdam. Theoretical He I Emissivities in the Case B Approximation. *ApJL*, 622:L73–L75, March 2005. doi: 10.1086/429370.
- Y. Rephaeli. Gas heating by energetic particles in M87 and the Coma cluster. *MNRAS*, 225:851–858, April 1987.
- C. S. Reynolds and A. C. Fabian. Warm absorbers in active galactic nuclei. *MNRAS*, 273:1167–1176, April 1995.
- M. Röllig, N. P. Abel, T. Bell, F. Bensch, J. Black, G. J. Ferland, B. Jonkheid, I. Kamp, M. J. Kaufman, J. Le Bourlot, F. Le Petit, R. Meijerink, O. Morata, V. Ossenkopf, E. Roueff, G. Shaw, M. Spaans, A. Sternberg, J. Stutzki, W.-F. Thi, E. F. van Dishoeck, P. A. M. van Hoof, S. Viti, and M. G. Wolfire. A photon dominated region code comparison study. *A&A*, 467:187–206, May 2007. doi: 10.1051/0004-6361:20065918.
- B. Rossi. *High-Energy Particles*. New York: Prentice-Hall, 1952.
- H. E. Saraph. Excitation of Ca^+ by electron impact: polarization of line radiation and transitions between fine-structure levels. *Journal of Physics B Atomic Molecular Physics*, 3:952–958, July 1970. doi: 10.1088/0022-3700/3/7/009.
- M. Schwarzschild. *Structure and evolution of the stars*. New York: Dover Publication, 1965.
- J. S. Scott, G. D. Holman, J. A. Ionson, and K. Papadopoulos. The heating of gas in clusters of galaxies by relativistic electrons - Collective effects. *ApJ*, 239:769–773, August 1980. doi: 10.1086/158162.
- M. J. Seaton. Radiative recombination of hydrogenic ions. *MNRAS*, 119:81, 1959.
- G. Shaw, G. J. Ferland, N. P. Abel, P. C. Stancil, and P. A. M. van Hoof. Molecular Hydrogen in Star-forming Regions: Implementation of its Microphysics in CLOUDY. *ApJ*, 624:794–807, May 2005. doi: 10.1086/429215.
- R. A. Shine and J. L. Linsky. Physical properties of solar chromospheric plagues. II - Chromospheric plague models. *SoPh*, 39:49–77, November 1974. doi: 10.1007/BF00154970.
- J. M. Shull and M. E. van Steenberg. X-ray secondary heating and ionization in quasar emission-line clouds. *ApJ*, 298:268–274, November 1985. doi: 10.1086/163605.
- L. Spitzer. *Physics of Fully Ionized Gases (2nd edition)*. New York: Interscience, 1962.
- L. Spitzer. *Physical processes in the interstellar medium*. New York Wiley-Interscience, 1978. 333 p.
- L. J. Spitzer. The Temperature of Interstellar Matter. I. *ApJ*, 107:6, January 1948. doi: 10.1086/144984.
- L. J. Spitzer and M. G. Tomasko. Heating of H I Regions by Energetic Particles. *ApJ*, 152:971, June 1968. doi: 10.1086/149610.
- P. J. Storey and D. G. Hummer. Fast computer evaluation of radiative properties of hydrogenic systems. *Computer Physics Communications*, 66:129–141, July 1991. doi: 10.1016/0010-4655(91)90013-B.
- J. Sugar and C. Corliss. *Atomic energy levels of the iron-period elements: Potassium through Nickel*. Washington: American Chemical Society, 1985.
- P. Swings and O. Struve. Spectrographic Observations of Peculiar Stars. *ApJ*, 91:546, June 1940. doi: 10.1086/144195.
- A. G. G. M. Tielens and D. Hollenbach. Photodissociation regions. I - Basic model. II - A model for the Orion photodissociation region. *ApJ*, 291:722–754, April 1985. doi: 10.1086/163111.

- P. A. M. van Hoof, D. A. Beintema, D. A. Verner, and G. J. Ferland. The collision strength of the [Ne v] infrared fine-structure lines. *A&A*, 354:L41–L44, February 2000.
- P. A. M. van Hoof, J. C. Weingartner, P. G. Martin, K. Volk, and G. J. Ferland. Grains in Photo-Ionized Environments. In G. Ferland and D. W. Savin, editors, *Spectroscopic Challenges of Photoionized Plasmas*, volume 247 of *Astronomical Society of the Pacific Conference Series*, page 363, 2001.
- P. A. M. van Hoof, J. C. Weingartner, P. G. Martin, K. Volk, and G. J. Ferland. Grain size distributions and photoelectric heating in ionized media. *MNRAS*, 350:1330–1341, June 2004. doi: 10.1111/j.1365-2966.2004.07734.x.
- J. E. Vernazza, E. H. Avrett, and R. Loeser. Structure of the solar chromosphere. III - Models of the EUV brightness components of the quiet-sun. *ApJS*, 45:635–725, April 1981. doi: 10.1086/190731.
- D. A. Verner and G. J. Ferland. Atomic Data for Astrophysics. I. Radiative Recombination Rates for H-like, He-like, Li-like, and Na-like Ions over a Broad Range of Temperature. *ApJS*, 103:467, April 1996. doi: 10.1086/192284.
- D. A. Verner and D. G. Yakovlev. Analytic FITS for partial photoionization cross sections. *A&AS*, 109: 125–133, January 1995.
- D. A. Verner, D. G. Yakovlev, I. M. Band, and M. B. Trzhaskovskaya. Subshell Photoionization Cross Sections and Ionization Energies of Atoms and Ions from He to Zn. *Atomic Data and Nuclear Data Tables*, 55:233, 1993. doi: 10.1006/adnd.1993.1022.
- D. A. Verner, G. J. Ferland, K. T. Korista, and D. G. Yakovlev. Atomic Data for Astrophysics. II. New Analytic FITS for Photoionization Cross Sections of Atoms and Ions. *ApJ*, 465:487, July 1996a. doi: 10.1086/177435.
- D. A. Verner, E. M. Verner, and G. J. Ferland. Atomic Data for Permitted Resonance Lines of Atoms and Ions from H to Si, and S, Ar, Ca, and Fe. *Atomic Data and Nuclear Data Tables*, 64:1, 1996b. doi: 10.1006/adnd.1996.0018.
- E. M. Verner, D. A. Verner, K. T. Korista, J. W. Ferguson, F. Hamann, and G. J. Ferland. Numerical Simulations of Fe II Emission Spectra. *ApJS*, 120:101–112, January 1999. doi: 10.1086/313171.
- G. M. Voit. Energy deposition by X-ray photoelectrons into interstellar molecular clouds. *ApJ*, 377: 158–170, August 1991. doi: 10.1086/170344.
- W. D. Watson. Heating of Interstellar H I Clouds by Ultraviolet Photoelectron Emission from Grains. *ApJ*, 176:103, August 1972. doi: 10.1086/151613.
- J. C. Weingartner and B. T. Draine. Photoelectric Emission from Interstellar Dust: Grain Charging and Gas Heating. *ApJS*, 134:263–281, June 2001. doi: 10.1086/320852.
- AM Winslow. Implicit numerical method for Compton scattering energy exchange between electrons and non-Planckian radiation. Technical report, UCID-16854, California Univ., Livermore (USA). Lawrence Livermore Lab., 1975.
- A. W. Wishart. The bound-free photo-detachment cross-section of H-. *MNRAS*, 187:59P–610P, May 1979.
- A. B. Wyse. Low-Level Lines of Ionized Calcium in Me Variables. *PASP*, 53:184, June 1941. doi: 10.1086/125300.
- Y. Xu and R. McCray. Energy degradation of fast electrons in hydrogen gas. *ApJ*, 375:190–201, July 1991. doi: 10.1086/170180.
- P. T. Zycki, J. H. Krolik, A. A. Zdziarski, and T. R. Kallman. X-ray reflection from photoionized media in active galactic nuclei. *ApJ*, 437:597–610, December 1994. doi: 10.1086/175024.
- B. Zygelman and A. Dalgarno. The radiative association of He(+) and H. *ApJ*, 365:239, December 1990. doi: 10.1086/169475.